



Provided by the author(s) and University of Galway in accordance with publisher policies. Please cite the published version when available.

Title	Cortical Bone Fracture and Orthopaedic Fixation Devices: An Experimental and Computational Investigation
Author(s)	Feerick, Emer M
Publication Date	2012-09-28
Item record	http://hdl.handle.net/10379/3359

Downloaded 2024-04-26T13:26:17Z

Some rights reserved. For more information, please see the item record link above.



**Cortical Bone Fracture and
Orthopaedic Fixation Devices:
An Experimental and Computational Investigation**

Emer M. Feerick B.E. (2008)



A thesis submitted to the National University of Ireland as fulfilment of the requirements for the Degree of Doctor of Philosophy

September 2012

Mechanical and Biomedical Engineering
College of Engineering and Informatics
National University of Ireland, Galway

Supervisor of Research: Dr. Patrick McGarry

Abstract

An experimental and computational investigation of cortical bone failure mechanisms has been conducted in this thesis. Firstly, a computational comparison of four methods of proximal humeral fracture fixation was conducted. Peak stresses were predicted at the screw cortical bone interface. Carbon fibre reinforced PEEK (CFPEEK) devices were proposed as an alternative to existing metallic devices. It was demonstrated that CFPEEK devices lowered stresses at the screw cortical bone interface, thus lowering the risk of screw pullout/pushout. Next, a novel experimental test rig was developed, so that crack patterns during screw pullout could be identified in real time as the screw was removed from the cortical bone. Pullout tests were conducted with; (i) osteons aligned parallel to the central axis of the screw (longitudinal pullout) and (ii) osteons aligned perpendicular to the central axis of the screw (transverse pullout). This experimental study uncovered for the first time, the relationship between the microstructural alignment of cortical bone, the pullout strength and the crack patterns. Two methods of computational modelling were subsequently developed to capture the relationship uncovered during the experimental screw pullout study. The first method of element deletion required the use of a phenomenological biphasic multi-layered composite model. This model accurately predicted both the pullout force and crack patterns for longitudinal and transverse pullout. The element deletion method was limited to 2D simulations therefore an alternate method with a lower computational expense was investigated. The second method involved the development of anisotropic damage initiation criteria in conjunction with the extended finite element method (XFEM). In this case, it was not necessary to explicitly represent the geometric microstructure of bone thus lowering the computational demand. This model accurately predicted the relationship between the osteon alignment, failure forces and crack propagation orientation for mode I, mode II and mixed mode loading. Application, of this fully calibrated anisotropic damage XFEM predictive framework, to screw pullout and 3D simulations of proximal humeral fracture repair, highlighted the potential future application of this method in the field of orthopaedic device design.

Acknowledgements

First and foremost I would like to acknowledge the Irish Research Council for Science, Engineering & Technology (IRCSET) for funding the work of this thesis. Without financial support the studies of this thesis would not have been undertaken.

I would like to extend my sincere gratitude to my Ph.D. supervisor Dr. Patrick McGarry. Firstly, for his assistance in securing the aforementioned funding and additionally for his guidance, technical insight and the hours he dedicated to the studies and publication of the work of this thesis.

Special thanks to my fellow Ph.D. students in particular the “McGarry Group” members; Nicola, Enda, Eamonn, Will, Paul, Noel and Dave. It has been a great experience from the day to day to conference trips, made all the better by the individuals of the group and also all the other Ph.D. students in the department.

Thanks to the Irish Centre for High End Computing (ICHEC) for the provision of computational hours for the simulations presented in this thesis. I would also like to extend thanks to Mr. Hannan Mullet, Dr. Jim Kennedy and Dr. David FitzPatrick for their contributions in the orthopaedic device evaluation studies of this thesis.

I also must acknowledge the time dedicated by Prof. Sean Leen, Prof. Peter McHugh, Dr. Laoise McNamara and Dr. Mark Bruzzi to annual GRC meetings over the years. A special thanks to all of the technicians and staff members of the department particularly Mr. Patrick Kelly, Mr. William Kelly, Mr. Bonaventure Kennedy and Mr. William Brennan. Thanks to all staff members of the department of Mechanical and Biomedical engineering for their help over the years.

Last, but not least I would like to thank my family; my parents Mary and PJ and my sisters Susan and Claire, for their support and help throughout the course of my studies. Without their continued support during the whole process it would have been a much more difficult undertaking. This support is not something that gets documented, but I certainly won't forget it!

Table of Contents

Chapter 1

Introduction.....	1
-------------------	---

Chapter 2

Background.....	10
2.1 Bone Mechanics	10
2.1.1 Bone Structure.....	11
2.1.2 Mechanical Properties of Cortical Bone	13
2.1.3 Mechanical Properties of Cancellous Bone	18
2.1.4 Animal and Synthetic Bone	19
2.2 The Shoulder: Anatomy, Fracture and Repair	21
2.2.1 The Glenohumeral Shoulder Joint	21
2.2.2 Proximal Humeral Fractures	23
2.2.3 Non Operative	25
2.2.4 Percutaneous Fixation (K-wires/Sutures)	25
2.2.5 Plate Fixation	25
2.2.6 Intramedullary Fixation.....	27
2.2.7 Hemiarthroplasty.....	28
2.3 Finite Element Modelling of the Humerus	28
2.4 Orthopaedic Screws	29
2.5 Biomaterials	33
2.6 References	36

Chapter 3

Theory	42
3.1 Introduction.....	42
3.2 Deformation (Measuring Stress and Strain).....	43
3.3 Elasto-Plasticity	45
3.4 Damage Modelling.....	48
3.4.1 Damage Modelling with Element Deletion	48
3.4.2 Damage Modelling with XFEM	50
3.5 Abaqus Standard (Implicit) vs Explicit Modelling	52
3.5.1 Implicit Modelling	52
3.5.2 Explicit Modelling	54
3.6 References	57

Chapter 4

Investigation of metallic and carbon fibre PEEK fracture fixation devices for three-part proximal humeral fractures	58
4.1 Introduction	58
4.2 Materials & Methods	60
4.2.1 Experimental	60
4.2.2 Computational:	61
4.3 Results	67
4.3.1 Experimental:	67
4.3.2 Computational:	67
4.4 Discussion	76
4.5 References	81
4.6 Appendix 4A	84

Chapter 5

Experimental Study of Cortical Bone Screw Pullout.....	85
5.1 Introduction	85
5.2 Materials and Methods	86
5.2.1 Sample preparation.....	86
5.2.2 Orthopaedic Cortical Bone Screws	86
5.2.3 Standard Pullout Tests	88
5.2.4 Screw Pullout Damage Visualisation Test (SPDV)	89
5.2.5 Comparison of Standard Pullout and SPDV Tests.....	91
5.2.6 SPDV Test Image Capture	92
5.3 Results	92
5.3.1 Complete Pullout.....	93
5.3.1.1 Longitudinal Pullout Results.....	93
5.3.1.2 Transverse Pullout Results	94
5.3.2 Screw Pullout Damage Visualisation.....	96
5.3.2.1 SPDV Longitudinal Pullout Results	96
5.3.2.2 SPDV Transverse Pullout Results.....	98
5.4 Discussion	100
5.5 References	102
5.6 Appendix 5A: Test Rig CAD Assembly Drawings	103
5.7 Appendix 5B: Computational Assessment of SPDV Test	105

Chapter 6

Computational Study of Cortical Bone Screw Pullout using Element Deletion.....	111
6.1 Introduction	111
6.2 Materials and Methods	112
6.3 Results	114
6.4 Discussion	123
6.5 References	126
6.6 Appendix 6A: Model B Calibration	128

Chapter 7

Anisotropic Mode Dependent Damage of Cortical Bone using the Extended Finite Element Method (XFEM).....	134
7.1 Introduction	134
7.2 Materials & Methods	136
7.2.1 Cortical Bone Failure Criteria	136
7.2.2 Material Parameter Longitudinal Calibration	138
7.2.3 Material Parameter Transverse/Longitudinal Calibration.....	138
7.2.4 XFEM Application: 2D and 3D Screw Pullout	141
7.3 Results	141
7.3.1 Material Parameter Longitudinal/Transverse Calibration.....	141
7.3.2 2D application: Screw pullout.....	145
7.4 XFEM Application: 3D Proximal Humeral Fracture Fixation	147
7.4.1 Materials and Methods	147
7.4.2 Results	148
7.5 XFEM Application: CF PEEK orthopaedic screws	152
7.6 Discussion	154
7.7 References	158
7.8 Appendix 7A: Mesh Sensitivity	160
7.9 Appendix 7B: XFEM Observations	160
7.10 Appendix 7C: 2D FORTRAN User Subroutine.....	162
7.11 Appendix 7D: 3D FORTRAN User Subroutine	164

Chapter 8

Concluding Remarks	167
---------------------------------	------------

Chapter 1

Introduction

Orthopaedic fracture fixation encompasses a broad range of fracture types. Currently an orthopaedic surgeon may select from a wide array of commercially available devices for the surgical repair of a given fracture type. Selection of a fracture fixation device is seldom biomechanically motivated, but is more generally based on the experience/preferred practice of the surgeon, on publications of clinical outcomes for large patient populations, or restriction to hospital approved medical device vendors. Proximal humeral fractures are the third most common fracture after hip and wrist fractures. The complexity of a humerus fracture repair increases with the number of fracture fragments that result from the injury, and with the level of displacement of these fragments. Several types of proximal humeral fracture fixation devices have been developed and implemented clinically. However, to date an optimal repair device is yet to be identified as a function of the number and displacement of fracture fragments, with a high rate of device failure being reported. Commonly reported failures of screw anchored devices include screw pullout/pushout (43% of patients over 60 years of age (Owsley and Gorczyca (2008))). One such example is shown in Figure 1.1, in which the screw has penetrated the cortical bone of the humerus, making contact with the glenoid surface. In order to progress towards an optimal device design with sufficient life span and reversion to intact functionality, it is important to identify the key device design features that dictate the success or failure of a fracture device. In addition to this, a complete understanding of the material properties of bone and the failure mechanisms that occur during the failure of these devices is paramount.

The overall aim of this thesis is to gain a better fundamental understanding of the failure mechanisms of cortical bone, with a specific focus on screw pullout and proximal humeral fracture repair.

The specific objectives of this thesis are;

- Analysis of proximal humeral fracture fixation techniques to identify potential failures in terms of fracture fragment stability and stress distribution within the cortical bone of a three part fracture repaired humerus.
- Investigation of cortical bone failure mechanisms during screw pullout by developing a novel damage visualisation test rig to capture failure mechanisms of cortical bone during pullout.
- Development of a phenomenological biphasic multi-layered composite model as a representation of cortical bone microstructure and use this in conjunction with the damage evolution method of element deletion to predict the pullout strength and crack patterns during cortical bone screw pullout (as observed experimentally).
- Development of an anisotropic elastic homogeneous continuum representation of cortical bone coupled with anisotropic damage initiation criteria using the extended finite element method (XFEM). Therefore, lowering computational expense compared to the phenomenological biphasic multi-layered composite model.
- Application of the anisotropic elastic homogeneous continuum representation of cortical bone coupled with anisotropic damage initiation criteria to 2D and 3D single screw pullout as well as 3D locking plate repair of a three part proximal humeral fracture fixation.

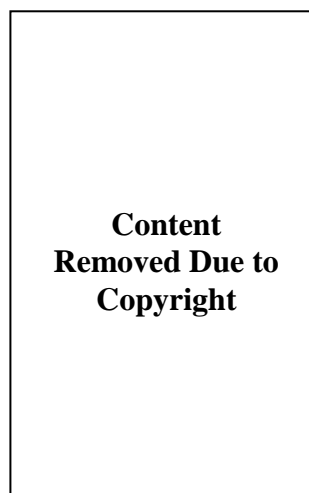


Figure 1.1 X-ray images of locking plate, with screw penetration highlighted at the glenohumeral interface. Image obtained from Owsley and Gorczyca (2008)

A flowchart is presented in Figure 1.2 for this thesis outlining the key findings of each study and the motivation each provided for subsequent experimental and computational studies.

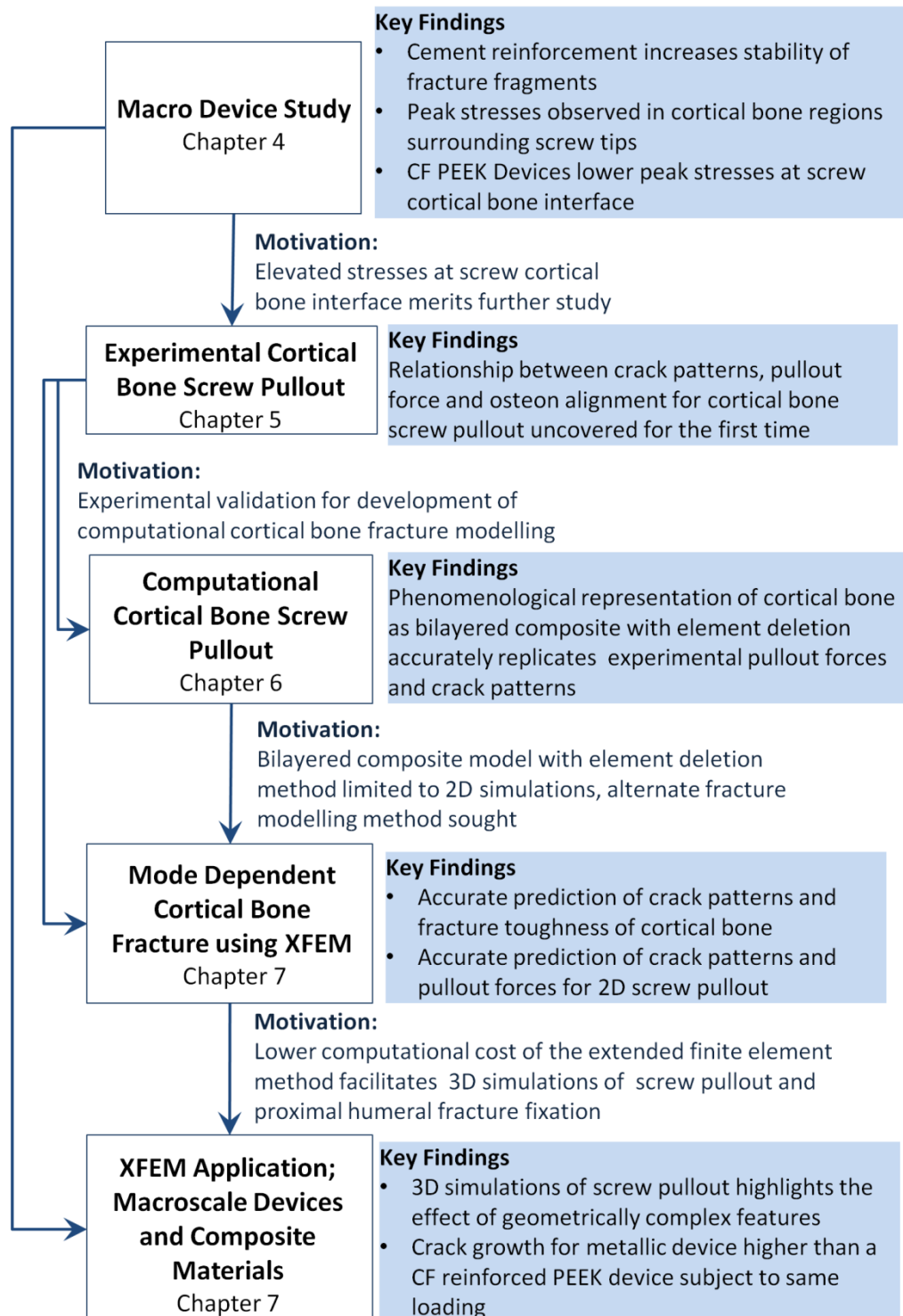


Figure 1.2 Flowchart outlining the key findings of each study and the motivation each provided for subsequent experimental and computational study that followed

The research work presented in this thesis began in the area of fracture fixation of the proximal humerus. For the first time, a detailed computational assessment of four proximal humeral fraction fixation techniques was conducted. The initial focus of this study was comparison of the performance of metallic fracture fixation devices, in terms of stability of fracture fragments and stress distribution within the humerus. These results provided some clinically relevant outcomes, such as, cement reinforced devices offer greater stability by lowering the micro motion between fracture fragments. Furthermore, a more significant observation were pressure and shear stress concentrations at the screw cortical bone interface, highlighting potential locations of failure at the screw cortical bone interface. This was due to the significantly higher stiffness of metallic implants, compared to the cortical bone in which they were implanted. The magnitude of these stress concentrations were in the range of osteoporotic cortical bone ultimate strength (Dickenson et al. (1981)). Therefore, an alternate material (carbon fibre reinforced PEEK (CFPEEK)) was proposed for the locking plate and intramedullary rod devices that had a modulus similar to that of cortical bone. This material offered similar stability to that of its metallic counterparts. Notably, a significant reduction in peak shear stresses at the screw tip bone interface was observed for a CFPEEK device. However, the trend of stress concentrations in the cortical bone surrounding screw tips remained, explaining clinically observed device failure (Figure 1.1). It is paramount for future device designs and configurations that the mechanisms leading to pullout and pushout are fully understood.

Following the key and most interesting finding of the fracture fixation analyses, stress concentrations predicted at the screw cortical bone interface, an experimental study of single screw pullout from cortical bone was conducted. Previous experimental screw pullout studies conducted tests according to ASTM standards. This type of test provides load displacement data but provides little enlightenment with regard to failure mechanisms in the material that lead to screw pullout. Due to the fact that cortical bone is highly anisotropic (Reilly and Burstein (1975); Cowin (2001)) with a distinct aligned microstructure (Rho et al. (1998); Kutz (2003)) the pullout strength and fracture patterns were expected to be related to the orientation of this microstructure. A novel test rig was developed which is referred to a screw pullout damage visualisation (SPDV) test. This novel test rig was used to investigate

cortical bone failure mechanisms in real time as the screw was removed from the cortical bone. Standard pullout tests were also conducted; load data from the standard pullout tests was used to validate the load data recorded during an SPDV test. The experimental SPDV test successfully uncovered for the first time, the relationship between osteon alignment, crack patterns and failure force for cortical bone screw pullout (Alternate pullout strengths were previously reported by Seebeck et al. (2004), however no failure mechanisms were uncovered). Pullout force was highest for osteons aligned perpendicular to the pullout direction (transverse pullout). Large deformation and significant crack growth perpendicular to the central axis of the screw was observed during transverse pullout. Pullout force was significantly lower for osteons aligned parallel to the direction of pullout (longitudinal). Localised crack patterns parallel to the central axis of the screw were observed with material between screw threads removed during longitudinal pullout. Such significant findings provided motivation for the development of a computational model capable of replicating the phenomena observed experimentally. The development of a validated computational model for cortical bone fracture potentially offers a powerful design evaluation tool for a range of orthopaedic devices.

Initial computational simulations of cortical bone screw pullout were conducted using a homogeneous anisotropic elasto-plastic material coupled with the crack propagation method of element deletion. Despite the significantly different material properties assigned in the directions parallel and perpendicular to the osteon directions, the same crack patterns were predicted for both a longitudinal and transverse simulation. This was due to the fact that the element removal technique utilises isotropic damage evolution and the removal of an element had no associated directionality. This critical finding motivated the development of a phenomenological representation of the cortical bone microstructure to capture the key differences between longitudinal and transverse pullout forces and failure mechanisms. A biphasic multi-layered composite model was developed as a phenomenological representation of the microstructure of cortical bone. 2D axisymmetric simulations of cortical bone screw pullout (based on the geometry of the screws used in the experimental study) were conducted. The calibrated biphasic multi-layered composite model developed is capable of predicting (i) Higher pullout

forces for transverse pullout; (ii) Horizontal crack paths perpendicular to screw axis for transverse pullout, whereas vertical crack paths were computed for longitudinal pullout. This provides a useful paradigm that can be used to evaluate screw thread design for application specific fracture fixation. However, it emerged that application of the biphasic multi-layered composite model with element deletion to 3D simulations raised computational demand beyond a viable threshold. This limited the biphasic multi-layered composite model to 2D simulations. Many orthopaedic devices contain unsymmetrical or geometrically complex features that cannot be fully evaluated in 2D. For example, self tapping orthopaedic screws have unsymmetrical features such as a helical design and a cutting flute at the screw tip that aids insertion. Therefore, it was clear that an alternate method of fracture modelling with a lower computational demand was required in order to conduct 3D simulations of screw pullout or whole bone fracture fixation.

One such crack propagation technique that was identified was the extended finite element method (XFEM). For this method, cracks propagate through a mesh by splitting elements instead of removing them from the mesh. Explicit representation of cortical bone microstructure was not necessary; instead it is simply modelled as an anisotropic homogeneous elastic continuum. In order to capture experimentally observed crack propagation direction and mode dependent fracture toughness, anisotropic damage initiation criteria were developed based on a known osteon orientation. The anisotropic damage initiation criteria were developed for XFEM prediction of crack initiation and direction of crack propagation. Interestingly, this highlights the critical role of the anisotropic damage initiation criteria with definition of crack direction via XFEM. The anisotropic elasto-plastic homogeneous modelling that was implemented in conjunction with the element deletion method (mentioned previously) failed to capture differences between crack patterns and failure forces. This was due to the fact that the element deletion technique utilises isotropic damage evolution and the removal of an element had no associated directionality. A unique set of parameters were calibrated using data reported by previous experimental studies of cortical bone fracture toughness (Norman et al. (1996); Zimmermann et al. (2009)). The proposed homogenised representation of cortical bone coupled with anisotropic damage initiation criteria in conjunction with XFEM predict; (i) the relationship between fracture energy and osteon alignment; (ii) the alternate crack

patterns for both varying osteon orientations and loading angle. Application of the calibrated XFEM model to 2D screw pullout resulted in accurate prediction of; (i) distinctive patterns of crack propagation during screw pullout for longitudinal and transverse screw pullout; (ii) alternate pullout strengths, with transverse pullout requiring significantly higher pullout force than longitudinal simulations. Both of these findings accurately replicate the experimental findings of single screw pullout.

Due to the lower computational expense of XFEM, application of the calibrated material properties to 3D models was possible. 3D simulations of single screw pullout were conducted revealing the influence of helical screw design and cutting flute of self tapping orthopaedic screws. Furthermore, the calibrated material model with XFEM was then applied to unreinforced locking plate fixation of the proximal humerus using the 3D models generated as part of the initial work of this thesis. Simulations revealed that the level of crack growth for a metallic device was significantly higher than that of a CF reinforced PEEK device for the same loading magnitude. Critical locations of crack initiation are also identified. This concluding application of the methodologies developed in this thesis for cortical bone fracture modelling highlights the huge potential for their application to future designing of orthopaedic fracture fixation devices.

The structure of this thesis is presented as follows. Chapter 2 outlines the important background literature relevant to the work of the present thesis to provide an introduction to bone mechanics, proximal humeral fractures, fixation devices and biomaterials. It is important to note that additional relevant literature for each of the experimental and computational studies is also presented at the beginning of each chapter as an introduction to that study. Chapter 3 outlines the important relevant computational theory on finite element techniques, material formulations and damage techniques used in the computational analyses of Chapters 4, 6 and 7. Chapter 4 contains the initial work providing significant motivation for the primary application focus of this thesis, namely cortical bone screw pullout. Chapter 5 contains the experimental study of single screw pullout from bovine cortical bone. The experimental results of Chapter 5 provide validation of the computational models of cortical bone screw pullout outlined in Chapters 6 and 7. The 2D

computational models developed for cortical bone screw pullout using the element deletion method (based on the experimentally observed data) are presented in Chapter 6. The anisotropic homogeneous elastic continuum models of cortical bone coupled with anisotropic damage initiation criteria and evolution via XFEM are presented in Chapter 7. The additional application of XFEM to 2D and 3D screw pullout as well as 3D macroscale simulations of locking plate fixation, of a 3 part proximal humeral fracture, are contained in Chapter 7. Concluding remarks and suggested future work are outlined in Chapter 8 of this thesis.

References

- Cowin, S. C., 2001. Bone mechanics handbook, CRC press USA.
- Dickenson, R. P., Hutton, W. C. and Stott, J. R., 1981. The mechanical properties of bone in osteoporosis. *Journal of Bone and Joint Surgery-British* Volume 63, 233-38.
- Kutz, M., 2003. *Standard Handbook of Biomedical Engineering and Design*, McGraw-Hill. 8.1-8.23.
- Norman, T. L., Nivargikar, S. V. and Burr, D. B., 1996. Resistance to crack growth in human cortical bone is greater in shear than in tension. *Journal of Biomechanics* 29, 1023-1031.
- Owsley, K. C. and Gorczyca, J. T., 2008. Displacement/Screw Cutout After Open Reduction and Locked Plate Fixation of Humeral Fractures. *J Bone Joint Surg Am* 90, 233-240.
- Reilly, D. T. and Burstein, A. H., 1975. The elastic and ultimate properties of compact bone tissue. *Journal of Biomechanics* 8, 393-396, IN9-IN11, 397-405.
- Rho, J.-Y., Kuhn-Spearing, L. and Zioupos, P., 1998. Mechanical properties and the hierarchical structure of bone. *Medical Engineering & Physics* 20, 92-102.
- Seebeck, J., Goldhahn, J., Städele, H., Messmer, P., Morlock, M. M. and Schneider, E., 2004. Effect of cortical thickness and cancellous bone density on the holding strength of internal fixator screws. *Journal of Orthopaedic Research* 22, 1237-1242.
- Zimmermann, E. A., Launey, M. E., Barth, H. D. and Ritchie, R. O., 2009. Mixed-mode fracture of human cortical bone. *Biomaterials* 30, 5877-5884.

Chapter 2

Background

The sections of this chapter provide an introduction to the relevant subject areas of this thesis. Bone structure, mechanics and experimentally reported material properties are summarised for human, animal and synthetic bone. The anatomy of the shoulder is introduced with a specific focus on the glenohumeral joint. Proximal humeral fracture classification is also introduced in addition to some of repair options that are investigated as part of this thesis. The relevant biomaterials associated with proximal humeral fracture repair and screw pullout are also discussed. In addition to the background literature provided in this chapter, critically relevant literature to each of the studies of Chapter 4-7 is provided as an introduction within that chapter.

2.1 Bone Mechanics

The skeletal system provides structure and shape for the body while also protecting vital internal organs. Movement of the body is also facilitated through the contracting of muscles that are anchored to the bones of the skeletal system. As the skeletal system performs these functions, bone undergoes a range of loading configurations both cyclically and statically. Bone is an ever growing tissue with the ability to adapt to its loading environment. The two main types of bone tissue are cortical and trabecular bone. Cortical bone is the dense tough skin forming the outer morphology of bone. Cancellous bone is less dense, consisting of a porous network of trabeculae that form the spongy bone located under the outer layers of cortical bone (Rho et al. (1998); Kutz (2003); Liebschner (2004)). A summary of the microstructure of cortical and cancellous bone is shown in Figure 2.1

Content Removed Due to Copyright

Figure 2.1 Cortical and cancellous bone microstructure and location within a typical long bone at a multiscale level; image obtained from Liebschner and Keller (2005)

2.1.1 Bone Structure

Cortical bone is a naturally occurring composite. The constituents can be classified as organic and inorganic phases and water. The organic phase consists of impure hydroxyapatite, while the inorganic phase consists mainly of collagen (90% type I collagen) (Currey (2002); Kutz (2003)). The organisation of these constituents is shown in Figure 2.2. At the micro-scale concentric stacks of collagen sheets with a central Haversian canal form osteons. Volkmann's canals run perpendicular to Haversian canals interconnecting neighbouring haversian canals with the periosteum. The periosteum is the membrane covering the surface of all bones consisting of a network of dense fibrous tissue providing the blood supply and nourishment to the bone. Osteons are embedded in an interstitial matrix of hydroxyapatite, as illustrated in Figure 2.2 as the regions between neighbouring osteons. In long whole bones, osteons are aligned parallel to the central axis of the bone (Rho et al. (1998); Kutz (2003)).

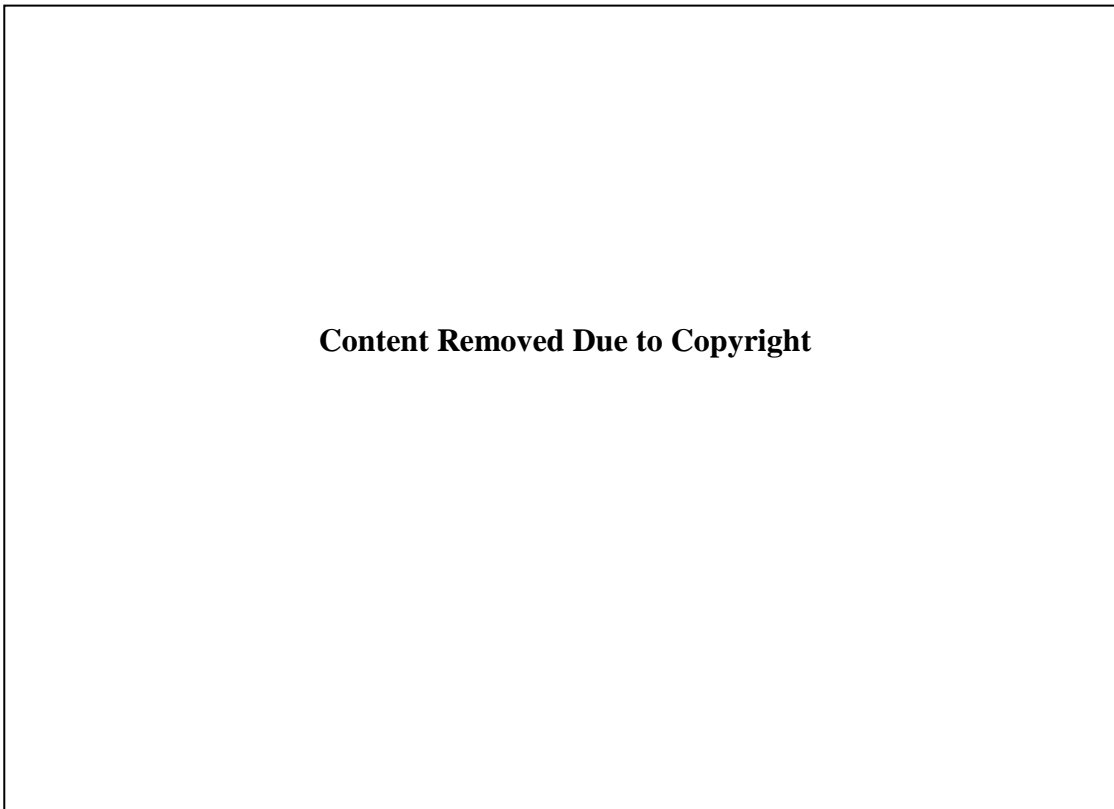


Figure 2.2 Cortical bone microstructure; image obtained from Weatherholt et al. (2012)

Two categories of bone exist for cortical bone, woven or lamellar bone. Primary bone or early life bone is referred to as woven bone (An and Draughn (1999)). Woven bone is formed at birth with no distinct arrangement of osteons in the microstructure. Collagen fibres are arranged at random within woven bone. Due to the random arrangement of the microstructure of woven bone it has a much lower strength than lamellar bone. Lamellar or secondary bone is the structure outlined in Figure 2.2. It is formed with age as woven bone is remodelled and the structured alignment of collagen shown in Figure 2.2 is formed (McNamara (2011)). The alignment of the fibres of the stacked collagen sheets shown in Figure 2.2B can also vary as shown in Figure 2.3 (An and Draughn (1999)).

Cancellous bone is a porous structure that has significantly lower density and higher porosity than cortical bone (Kutz (2003)). It is located in the medulla of the bone in the epiphysis and metaphysic regions of long bones (An and Draughn (1999)). The microstructure of cancellous bone consists of a network of rods and plates or trabeculae producing a spongy porous structure (An and Draughn (1999))

(Figure 2.1). Interdigitated between the pores of cancellous bone is a fluid of bone marrow (McNamara (2011)).

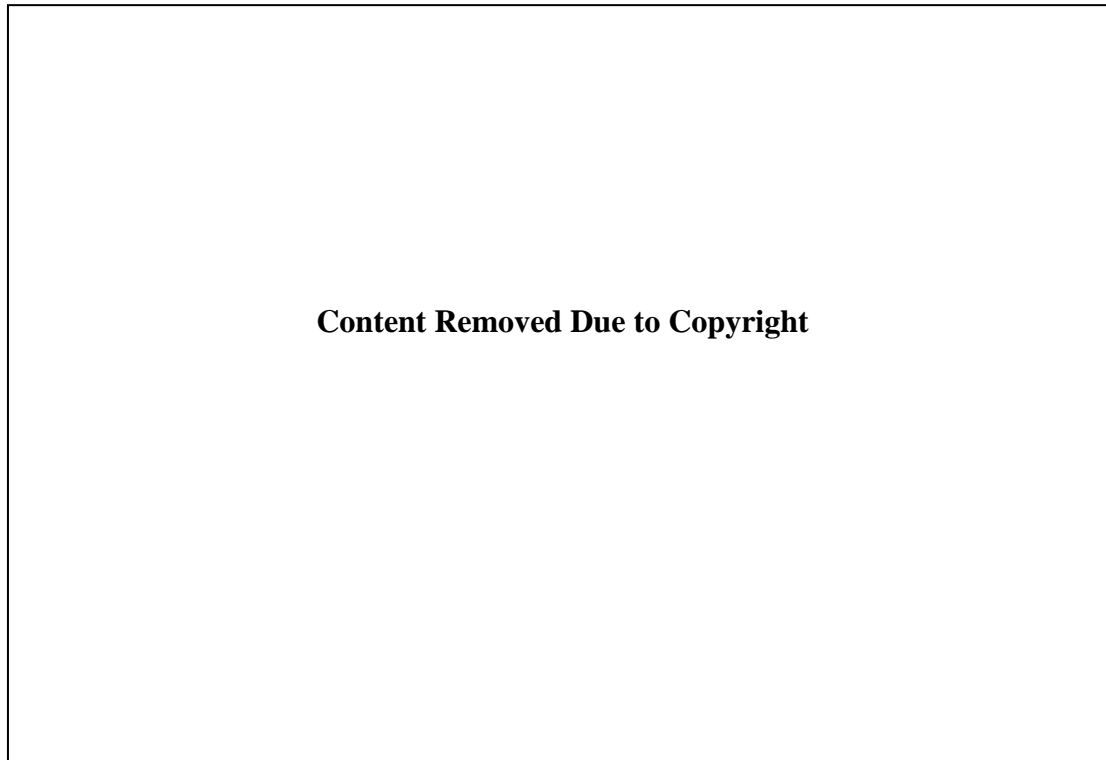


Figure 2.3 Illustration of three types of osteons. Transversal (T), alternate (A) and longitudinal (L) osteon. Image obtained from An and Draughn (1999)

This combined architecture of cortical and cancellous bone provides the unique material properties recorded for bone. Additionally, the microstructure is responsible for the complex stress distribution within whole bones as they undergo single and multiaxial loadings both statically and cyclically during daily activities.

2.1.2 Mechanical Properties of Cortical Bone

The mechanical properties of cortical bone have been experimentally investigated by several research groups at multiple scales using a range of experimental test methods. Some of the reported material properties are summarised in Table 2.1.

It is clear from Table 2.1 that cortical bone is an anisotropic material. It exhibits different strengths under tension and compression, with highest strength in the latter. Additionally, from the data of Table 2.1, the size of the cortical bone samples has an

effect on the elastic modulus, as the modulus for single osteons is consistently lower than larger macroscale samples used by Reilly and Burstein (1975). The size dependency of cortical bone samples relative to elastic modulus was investigated by Choi et al. (1990). A range of sample sizes were investigated with heights of 100-1000 μm . The relationship between sample size and modulus observed by Choi et al. (1990) is shown in Figure 2.4.



Figure 2.4 Size dependency of cortical bone modulus relative to the surface area to volume ratio. Image taken from Choi et al. (1990).

The age related properties of cortical bone have also been investigated (Burstein et al. (1976); Dickenson et al. (1981); Zioupos and Currey (1998)). The most significant age related change reported by Burstein et al. (1976) for healthy specimens was the reduction in plastic strain before failure. Therefore there was an increase in instances of brittle failure with age. Dickenson et al. (1981) reported the altered mechanical properties of healthy (normal) bone compared to that of osteoporotic bone aged 67-91 years. Osteoporosis is a disease that leaches bone mass and leads to thinning bone microstructures. This is due to defective bone remodelling activity. This disease is predominantly associated with postmenopausal women (McNamara (2011)). The altered mechanical properties of cortical bone as a result of osteoporosis are shown in Figure 2.5.

Table 2.1 Modulus of Elasticity of Cortical bone

Study	Orientation	Specimen Origin	Modulus (GPa) Standard Deviation (SD)	Ultimate Strength (MPa)
Mechanical Test: Tension				
Reilly and Burstein (1975)	L	Human Femur	17.9 (3.9)	133
Reilly and Burstein (1975)	T	Human Femur	10.1 (2.4)	51
Ascenzi and Bonucci (1968)	L	Single Osteon Human Femur	11.7 (5.8)	
Ascenzi and Bonucci (1968)	A	Single Osteon Human Femur	5.5 (2.6)	
Ko (1953)	L	Human Humerus	17.2	
Ko (1953)	L	Human Radius	18.5	
Mechanical Test: Compression				
Reilly and Burstein (1975)	L	Human Femur	18.2 (0.85)	193
Reilly and Burstein (1975)	T	Human Femur	11.7(1.01)	133
Ascenzi and Bonucci (1968)	L	Single Osteon Human Femur	6.3 (1.8)	
Ascenzi and Bonucci (1968)	A	Single Osteon Human Femur	7.4 (1.6)	
Ascenzi and Bonucci (1968)	T	Single Osteon Human Femur	9.3 (1.6)	
Mechanical Test: Bending				
Reilly and Burstein (1975)		Human Femur	3.28 (0.38)	
Ascenzi et al. (1990)	L	Single Osteon Human Femur	2.32 (1.20)	
Ascenzi et al. (1990)	A	Single Osteon Human Femur	2.69 (0.93)	



Content Removed Due to Copyright

Figure 2.5 Stress strain curve for healthy and osteoporotic cortical bone aged 67-91 years. Image taken from Dickenson et al. (1981)

Asymmetric yielding is a material characteristic reported for cortical bone (Bayraktar et al. (2004); Mercer et al. (2006)). Cortical bone has a higher yield and ultimate strength in compression than in tension. The yielding response of cortical bone has been compared to that of a soil, with previous studies implementing the Drucker Prager plasticity model to simulate the cortical bone plasticity behaviour observed experimentally (Drucker and Prager (1952); Mercer et al. (2006); Mullins et al. (2009)).

Cortical bone also exhibits anisotropic fracture toughness. Several experimental studies have investigated the fracture toughness of cortical bone for longitudinally and transversely aligned cortical bone (Norman et al. (1996); Feng et al. (2000); Zimmermann et al. (2009); Zimmermann et al. (2010); Olvera et al. (2012)). Cortical bone exhibits the lowest fracture toughness when the applied loading is parallel to the direction of the osteon alignment. Fracture toughness of cortical bone is highest when the applied loading is perpendicular to the direction of osteon alignment as reported by Zimmermann et al. (2009). The relationship between fracture toughness and microstructural alignment are shown in Figure 2.6.

Content Removed Due to Copyright

Figure 2.6 Fracture toughness of cortical bone defined in terms of strain energy release rate as a function of phase angle for transversely and longitudinally aligned cortical bone. Image taken from Zimmermann et al. (2009)

In addition to the relationship of fracture toughness of cortical bone to microstructure alignment, the microstructure of cortical bone also influences the crack trajectories during fracture (Nalla et al. (2003); Nalla et al. (2004); Ritchie et al. (2006); Budyn and Hoc (2010)) (Figure 2.7).

Content Removed Due to Copyright

Figure 2.7 Illustrations of the toughening mechanisms of cortical bone, with the crack trajectories altered by the microstructure of cortical bone. (a) crack deflection due to osteons, (b) crack bridging by collagen fibres, (c) uncracked ligament bridging and (d) micro cracking. Image taken from Ritchie et al. (2006)

2.1.3 Mechanical Properties of Cancellous Bone

Cancellous bone is much more compliant than cortical bone with lower modulus of elasticity and ultimate strengths. A summary of the reported properties for cancellous bone is listed in Table 2.2. A large range of elastic moduli and ultimate strengths have been reported for cancellous bone.

The work presented in this thesis focuses on cortical bone. Cancellous bone is modelled in Chapter 4 as a linear elastic material. Detailed analysis of cancellous bone yield and fracture are beyond the scope of this thesis.

Table 2.2 Modulus of Elasticity and Ultimate Failure of Human Cancellous bone

Study	Specimen Origin	Elastic Modulus (MPa) Standard Deviation (SD)	Ultimate Strength (MPa)
Martens et al. (1983)	Femoral Head	900 (710)	9.3 (4.5)
Martens et al. (1983)	Proximal Femur	616 (707)	6.6 (6.3)
Kuhn et al. (1989)	Distal Femur	298 (224)	5.6 (3.8)
Linde et al. (1989)	Proximal Tibia	445 (257)	5.3 (2.9)
Keaveny et al. (1997)	Vertebral Body	165 (110)	-
Morgan et al. (2001) <i>Compressive Properties</i>	Vertebra	344 (148)	-
	Proximal Tibia	1091 (634)	-
	Greater Trochanter	622 (302)	-
	Femoral Neck	3230 (936)	-

2.1.4 Animal and Synthetic Bone

Animal bone is often used as an approximation for human bone due to its higher availability. Liebschner (2004) outlined the importance of selecting the appropriate animal model for a given experimental study as no standard selection criteria exist. Larger animal models such as bovine are most suitable for biomechanical studies. A summary of the reported material properties of animal bone models are included in Table 2.3. It is clear from this table of data that the animal bone is reasonably similar to human cadaveric cortical bone in terms of stiffness and strength.

Table 2.3 Modulus of Elasticity and Ultimate Failures of Animal Bone (Liebschner (2004))

Study	Specimen Origin	Elastic Modulus (GPa)	Ultimate Strength (MPa)
Mechanical Test: Tension			
Currey (1998)	Bovine Femur	26.1	148
Reilly and Burstein (1974)	Bovine Tibia	21.9 -31.4	240-295
Currey (1988)	Ovine Metatarsus	18.96 ± 2.2	
Currey (1998)	Equine Femur	21.2 ± 1.9	152
Mechanical Test: Compression			
Reilly and Burstein (1974)	Bovine Femur	23.1 – 30.4	129 - 182
Reilly and Burstein (1974)	Bovine Tibia	21.6 ± 5.3	152 ± 17
Simkin and Robin (1973)	Bovine Tibia	7.1 ± 1.05	
Mechanical Test: Bending			
An et al. (1996)	Lapine Humerus	13.6 ± 0.7	165 ± 5
Ayers et al. (1996)	Mouse Femur	5.3 ± 1.8	40 ± 13
Schryver (1978)	Equine Radius	16.2 – 20.2	217 - 249

Synthetic bones (polyurethane foam), such as the commercially available Sawbones, (Sawbones, Malmö, Sweden) is commonly used as a replacement for animal or human bone for the biomechanical assessment of orthopaedic devices (Agneskirchner et al. (2006); Roberts et al. (2007); Grover et al. (2011)). Synthetic bone is available in several forms for biomechanical testing. Whole synthetic bones are available for a range of long bone types. A synthetic humerus is shown in Figure 2.8. Synthetic whole bones consist of a short fibre filled epoxy outer skin to represent cortical bone. The inner volume of the synthetic bone is filled with solid rigid polyurethane foam (PU) to represent cancellous bone. Individual test blocks of synthetic cortical or cancellous bone area also available for the various grades listed in Table 2.4.

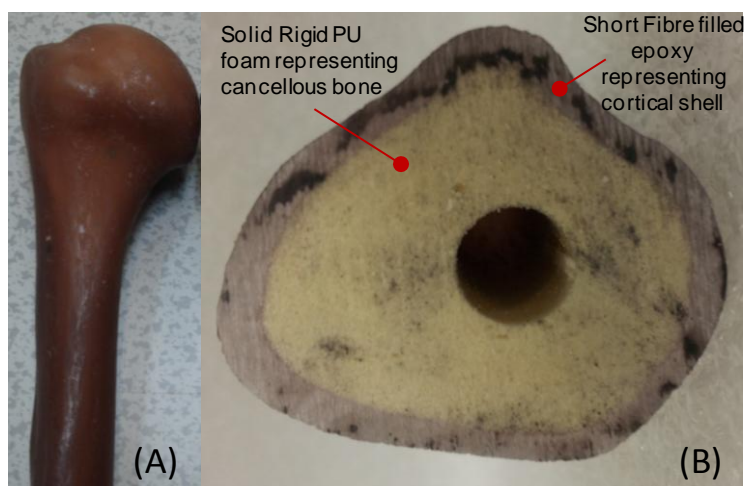


Figure 2.8 Whole bone synthetic humerus used in the experimental testing of Chapter 4; (A) Side view of synthetic humerus, (B) Section cut of synthetic humerus showing the short fibre filled epoxy skin representing the cortical shell and the inner solid rigid polyurethane foam representing cancellous bone.

Synthetic bone offers a consistent test material for device evaluation studies eliminating the inter specimen variability associated with animal or cadaveric bone (20-200 times lower inter specimen variability observed for synthetic bone versus cadaveric specimens Cristofolini et al. (1996)). Samples are easy to prepare, readily available and easy to handle. The use of synthetic bone has been validated as a test material for human bone. (Cristofolini et al. (1996); Cristofolini and Viceconti (2000)). However one clear disadvantage of synthetic bone is that the materials used

are homogeneous and isotropic. Natural bone, on the other hand, is highly anisotropic, due to spatial variations in density and a highly aligned microstructure. Hence, while synthetic bone may offer similar elastic properties to natural bone, their reliability as a model of inelastic behaviour and fracture of bone is questionable. In the current thesis it will be shown that the aligned microstructure of natural bone results in complex fracture properties. The range of mechanical properties reported for synthetic Sawbone representations of cortical bone and varying densities of cancellous bone are summarised in Table 2.4.

Table 2.4 Sawbone compressive properties (PacificResearchLaboratories (2012))

Material	Modulus	Strength (MPa)
Short Fibre Reinforced Epoxy (Cortical Shell)	16.7 GPa	157
Solid Rigid Foam (Cancellous Bone)	16–1148 MPa	0.6 - 48
Cellular Rigid Foam (Cancellous Bone)	12.4–137 MPa	1.4 – 5.4
Open Cell Rigid Foam (Cancellous Bone)	6.2–270 MPa	0.11 – 3.2

2.2 The Shoulder: Anatomy, Fracture and Repair

The bony anatomy of the shoulder joint is introduced in this section. Fracture classification of the humerus is introduced and the fixation options currently available are outlined highlighting previously reported clinical outcomes.

2.2.1 The Glenohumeral Shoulder Joint

The shoulder is a complex joint constructed by a network of muscles, tendons and ligaments. The shoulder facilitates the largest range of motion of any joint in the body. A healthy fully functional shoulder is held in a state of equilibrium by three joints;

1. The Glenohumeral joint
2. The Acromioclavicular joint
3. The Sternoclavicular joint

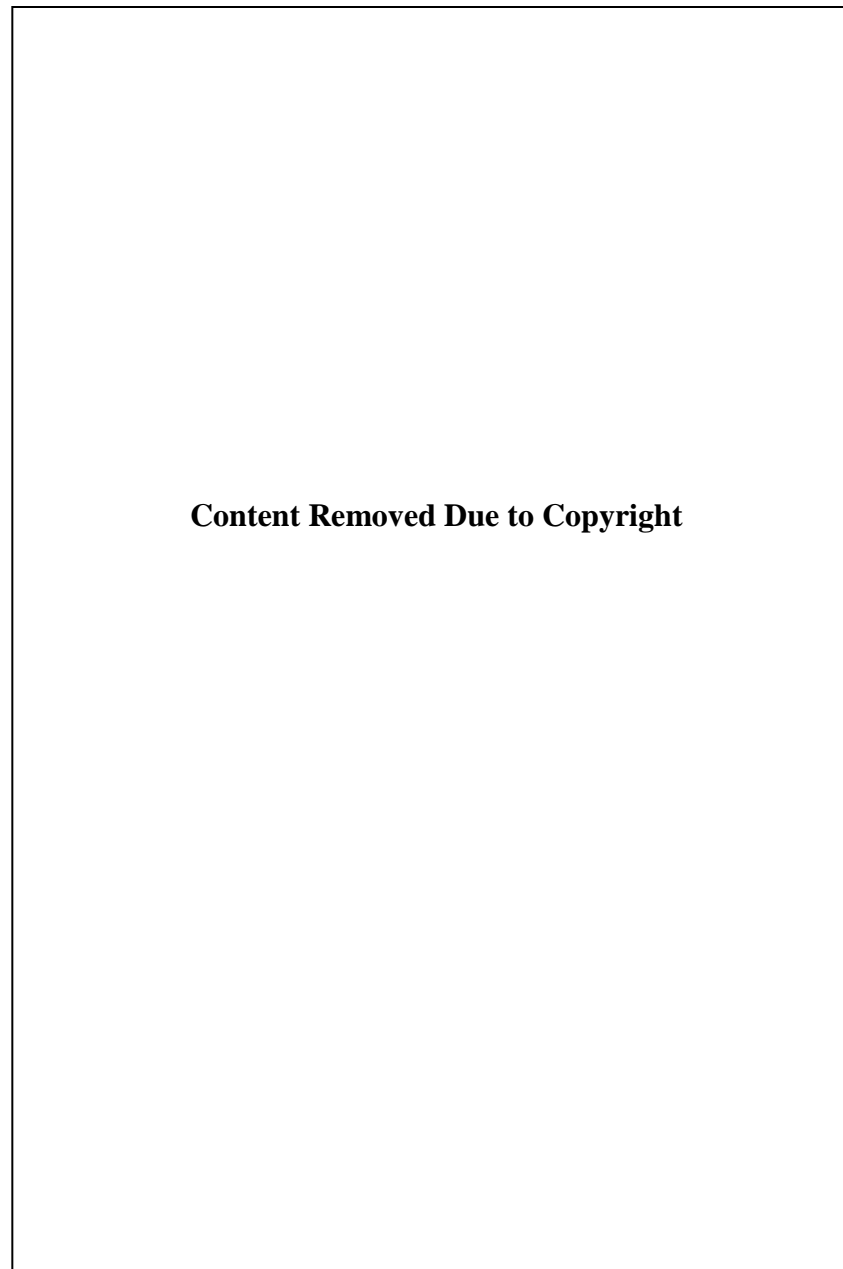


Figure 2.9 Shoulder joint bony anatomy. Image obtained from Agur and Dalley (2008)

The work presented on the shoulder in this thesis is focused on the humerus bone and the loading at the glenohumeral joint. The main bones of the shoulder are the humerus and the scapula which create the glenohumeral joint (Figure 2.9). The proximal humerus has three ossification centres; one for the head of the humerus, one for the greater tuberosity and one for the lesser tuberosity. The humeral head is a bony structure and its curvature is one third of a sphere. The scapula more commonly referred to as the shoulder blade is a thin sheet of bone with variable thickness across the surface. The bone serves as an attachment site for various

muscles as well as the glenoid. The humeral head sits into the glenoid, a shallow concave curved groove of the scapula cushioned by a layer of articular cartilage (Figure 2.10). The curved mating of the humerus and the glenoid facilitates a large range of motion. However the humeral head is much larger than the glenoid, stability of the joint is maintained by tissue surrounding the glenoid cavity (labrum), muscle and ligaments. Thus the potential for instability can be easily understood.

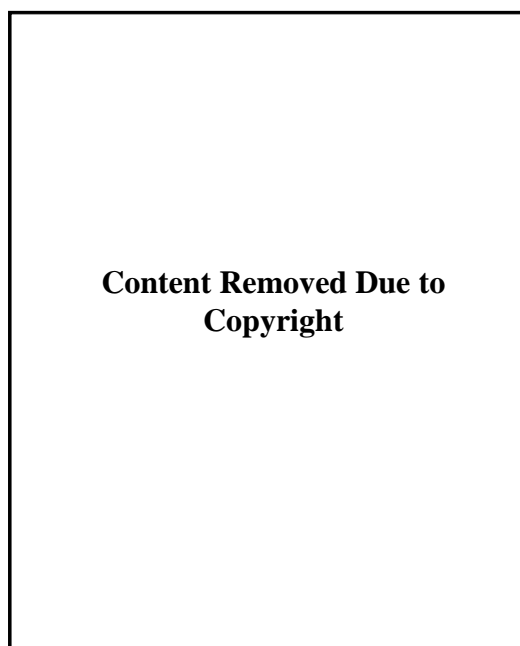


Figure 2.10 Lateral view of shoulder joint (scapula) highlighting glenoid cavity. Image obtained from Agur and Dalley (2008)

2.2.2 Proximal Humeral Fractures

Proximal humeral fractures are the second most common fracture to the upper extremity after the wrist (Johnell and Kanis (2006); Kettler et al. (2006)). This type of fracture can occur as a result of falling on an outstretched limb or as a result of a high energy impact. Women are also subject to higher incidence of the injury due to greater bone mass loss over the course of their lifetime (Johnell and Kanis (2006)).

The Neer classification chart is used to summarise the main types of proximal humeral fractures that occur. The classification chart is shown in Figure 2.11. The

fracture can be classified as a 2, 3 or 4 part fracture with different anatomical sites forming the third and fourth fragments. The fracture type focussed on in this thesis (Chapter 4) is a three part fracture of the proximal humerus with the greater tuberosity forming the third fragment.

Content Removed Due to Copyright

Figure 2.11 Neer Classification of proximal humeral fractures; (A) Complete Neer classification chart, (B) Three part fracture with greater tuberosity forming third fragment (this fracture type is the focus of Chapter 4 of this thesis). Image obtained from <http://faculty.washington.edu/alexbert/MEDEX/Winter/ch263fg10.jpg>

Several methods of fixation exist for proximal humeral fractures; these include both internal and external fixation as well as the option of open or closed reduction. Clinical and experimental studies have been conducted on many of the orthopaedic devices to examine their performance and success rate in patients.

Fracture management includes:

- Non-operative treatment,
- Percutaneous fixation,
- Open reduction internal fixation (ORIF) using various devices
- Humeral head replacement

2.2.3 Non Operative

Treatment of non displaced fractures involves a combination of protection and gradual mobilization. This would involve placing the arm in a sling and beginning physiotherapy as soon as possible (Koval et al. (1997)). Elderly patients with reduced physical demands are more likely to accept a stiff shoulder. Elderly patients are also more likely to be poor rehabilitation candidates thus suited to non operative treatment. This option is less appropriate for younger patients or those that wish to return to a full range of motion.

2.2.4 Percutaneous Fixation (K-wires/Sutures)

Percutaneous fixation is a closed reduction option (Figure 2.12); it is a minimally invasive procedure with minor scarring. This type of fixation has a reduced risk of avascular necrosis. Hägg and Lundberg (1984) reported that the risk of avascular necrosis is doubled when open reduction is selected. The risk is further increased when plating is selected for fixation. Resch et al. (1997) reported good functional outcome for percutaneous fixation of three and four part fractures where all patients returned to work or continued their normal activities. These results were achieved in younger patients with higher quality bone stock which may be the reason for the success of this type of fixation. This study reported that for older patients with osteoporosis the use of hemi prosthesis was advised. An experimental study by Koval et al. (1996) reported that K-wire fixation was unable to provide a fixation as strong as plate and screws or internal nails. Kwon et al. (2002) also reported a significant reduction in stability when K-wire fixation was compared to plate fixation.

2.2.5 Plate Fixation

Plate fixation is an open reduction internal fixation (Figure 2.13). Several types of plates have been developed including a cloverleaf plate, angle blade plate and locking plates. Rose et al. (2007) reported good functional outcomes for plate fixation however 25% of the fractures failed to heal. Koval et al. (1996) reported that T plate fixation offered the strongest fixation for 2 part fractures occurring at the metaphysic region. Kwon et al. (2002) conducted a study that compared three

fixation methods where no significant difference was reported between the stabilisation offered by the cloverleaf plate and the angular blade plate. High union rates and good functional outcomes were achieved with a locking plate system according to Muckter et al. (2001). However with these systems a high rate of screw cut out was found into the glenoid fossa in patients with weaker osteoporotic bone, this was shown by Owsley and Gorczyca (2008).

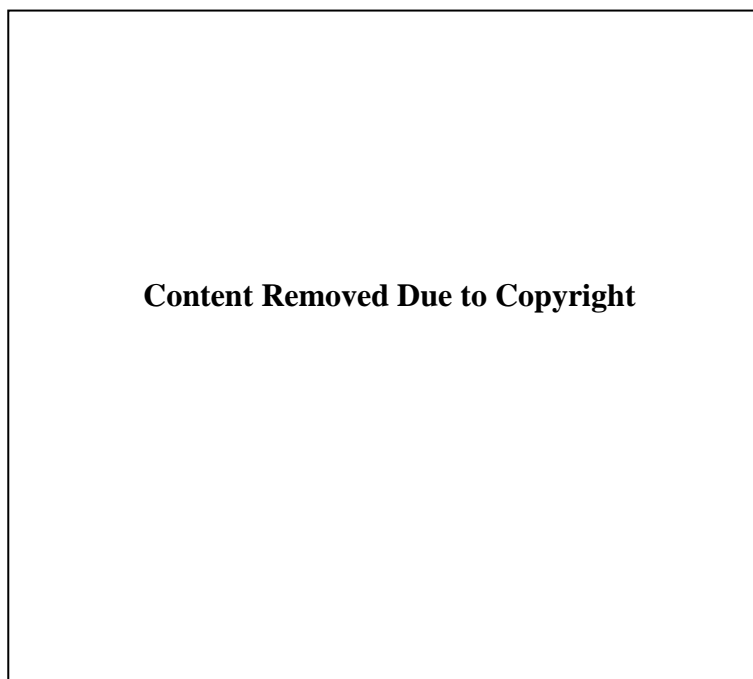


Figure 2.12 X-ray of percutaneous k-wire fixation. Image obtained from Kwon et al. (2002)

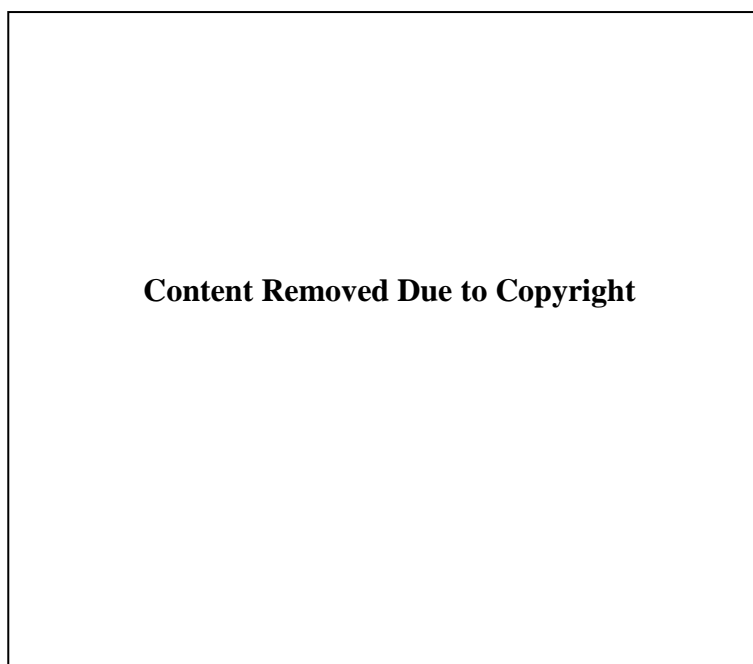


Figure 2.13 X-ray of plate fixation. Image obtained from Kwon et al. (2002)

2.2.6 Intramedullary Fixation

Several types of intramedullary devices have been developed and clinically evaluated (Figure 2.14). The cannulated titanium Polarus nail was evaluated by Koike et al. (2008) in 54 patients. 79% had satisfactory to excellent results. The success of this device was attributed to its usage in patients with a high bone stock, thus patients with severe osteoporosis may not be appropriate candidates for this fixation. Cuny et al. (2008) reported use of a straight telegraph nail with locking screws in 64 patients which achieved stabilisation and early mobilisation. However several weaknesses were identified with this type of fixation. These include possible rotator cuff damage due to insertion point as the nail transfixes the rotator cuff. Screw penetration is a common problem which requires early removal of device. The Bilboquet device was reviewed by Doursounian et al. (2000). It is a titanium internal fixation that can be converted to a humeral head replacement if complications arise. The device consists of two parts, a circular staple that is inserted into the humeral head and placed on top of a stem following its insertion into the humeral shaft. The study reported good results in 26 patients and proposed the Bilboquet as a viable alternative to hemiarthroplasty.



Figure 2.14 (A) X-ray of telegraph nail, (B) Illustration of telegraph nail. Images A-B obtained from Cuny et al. (2008). (C) X-ray of implanted Bilboquet device, (D) Image of Bilboquet two components pre implantation. Images C-D obtained from Doursounian et al. (2000)

2.2.7 Hemiarthroplasty

Hemiarthroplasty is one option in cases where it is not possible to salvage the humeral head (Figure 2.15). It offers good results for pain relief but there is a large variation in success rate with functional outcome depending on surgical positioning. A 15 year follow up by Sperling et al. (2004) revealed glenoid erosion in 72% of the cases and loosening in 34% of the cases. Thus hemiarthroplasty is recommended for older patients with low functional requirements.

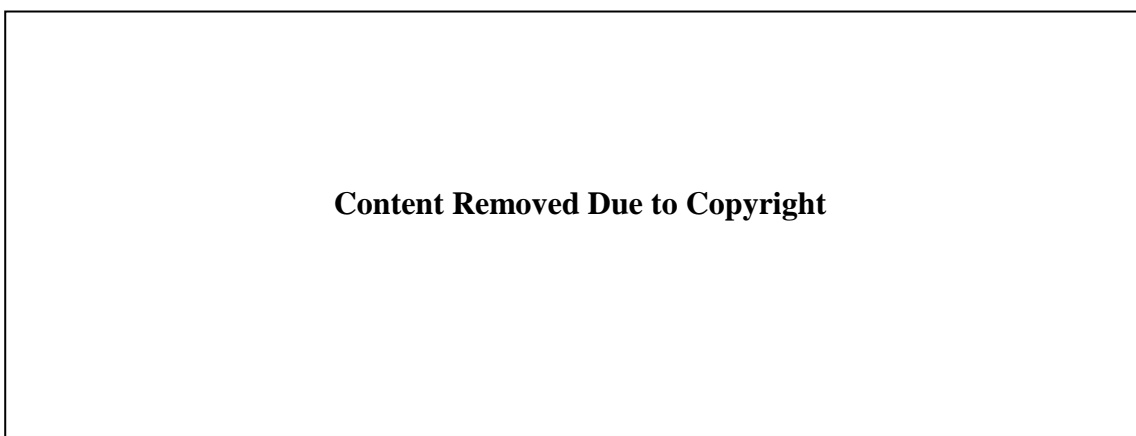


Figure 2.15 (A) X-ray of patient with rheumatoid arthritis prior to procedure, (B) X-ray of implant immediately after procedure, (C) X-ray of implant 20 years after procedure. Image taken from Sperling et al. (2004)

2.3 Finite Element Modelling of the Humerus

Few finite element studies of the humerus/ shoulder joint are reported in the literature. Finite element analysis has been somewhat underutilised for modelling of intact, fractured and repaired humeri. Previous studies have simplified representation of the distal humerus to a cylinder (Johnson (2007)). Studies that have modelled more complex bone geometry have focused on 2 part neck fractures of the humerus. This type of fracture has been modelled by Maldonado et al. (2003) considering a locking plate fracture fixation. This study concluded that the maximum strains in the humerus occurred at 90° arm abduction. The bone properties were assigned according to apparent density extracted from DEXA scans. The loading applied to the model represented 15 muscles of the shoulder as well as compression loading. However, the fracture line was simply modelled as an area of very low modulus, rather than modelling individual fragments. Therefore, contact and micro-motion between fracture fragments was not correctly simulated. Detailed 3D modelling of

the muscles of the shoulder joint reported by Webb et al. (2012) illustrated that the complex interaction between neighbouring muscles, large attachment areas of muscle to bone and complex muscle trajectories could not simply be represented by point load representation of muscles as conducted by Maldonado et al. (2003).

A 3D finite element study by Buchler et al. (2004) investigated the benefits of anatomical reconstruction of the humeral head for shoulder arthroplasty. This study highlighted the importance of replicating the anatomical geometry of each patient in order to ensure appropriate load transfer between the humerus and the glenoid. This would prevent altered stress distribution within the glenoid post operatively. This conclusion provides support for fracture fixation surgeries that salvage the fracture fragments of the humerus, as investigated in this thesis.

Clavert et al. (2006) developed a 3D model of an intact humerus including the muscles of the rotator cuff to identify the pathology of fractures of the proximal humerus. Simulations were conducted using the finite element solver NASTRAN. This study reported that peak stresses occurred in the cortical bone at 90° arm abduction.

2.4 Orthopaedic Screws

A large number of experimental test studies have been reported for pedicle screw pullout for spinal applications (Kincaid et al. (2007); Tan et al. (2007); Wen-Chi et al. (2009); Erkan et al. (2010)). Chapman et al. (1996) conducted an experimental study of screw pullout for twelve different orthopaedic screws (Figure 2.16). Both cannulated and non-cannulated screws were included with varying diameters and pitch. The testing was conducted on polyurethane foam to ensure consistent properties between test specimens. This study reported high correlation between the pullout strength of bone screws and machine screws. The following factors govern screw pullout:

- Major diameter of the screw
- Length of engagement of the thread
- Shear strength of the material the screw is inserted into
- Thread shape factor (pitch and thread depth parameters)

The major diameter of the screw and thread shape are factors that can be altered by designers to increase the contact area between the screws and the material in which it is embedded, hence increasing pullout strength. Length of engagement and shear strength of the material in which the screw is embedded are limiting factors for designers depending on the anatomical location. Chapman et al. (1996) was supported by the study of Gausepohl et al. (2001) which compared maximum holding power of fine versus coarse screw threads in both polyurethane foam and bovine bone (Figure 2.17). Due to the fact that orthopaedic implants are usually implanted into osteoporotic bone the question of tapping a hole prior to screw insertion is a concern. A pre-tapped hole will ensure correct screw placement but leads to a higher percentage of bone removal than self tapping screws. Self tapping screws will compact the bone around the threads as it is inserted thus increasing the pullout strength (Chapman et al. (1996)). Battula et al. (2006) compared the holding power of self tapping screws in both normal and osteoporotic bone in an attempt to identify the necessary depth at which screws must be inserted to achieve maximum pullout strength. This study reported that in normal bone the screw tip should protrude 1 mm beyond the far cortex and this should be increased to 2 mm for osteoporotic bone (referred to as a bicortical fixation). Screws protruding from the cortical bone of the humerus are possible in the distal region. However, screws protruding through the humeral head would damage the glenoid and labrum which would lead to further shoulder complications.

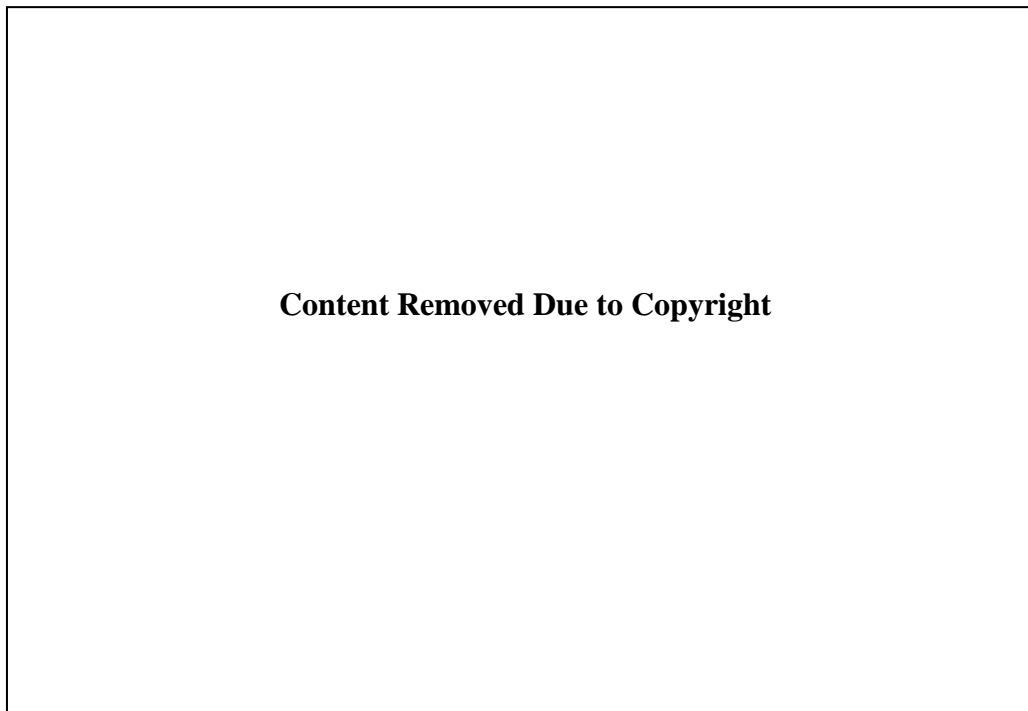


Figure 2.16 Screw design features and thread types reported by Chapman et al. (1996)

Shuib et al. (2007) conducted a finite element study of three simple thread geometries to evaluate the most biocompatible. Rectangular, triangular and trapezoidal thread types were compared. Plastic deformation was not included in the model and conclusions of the study simply reported that square threads were the most biocompatible, as there was an equal distribution of stress between the screw and bone thus preventing stress shielding. Stress shielding has been identified as one cause of screw loosening over time (Gefen (2002)).

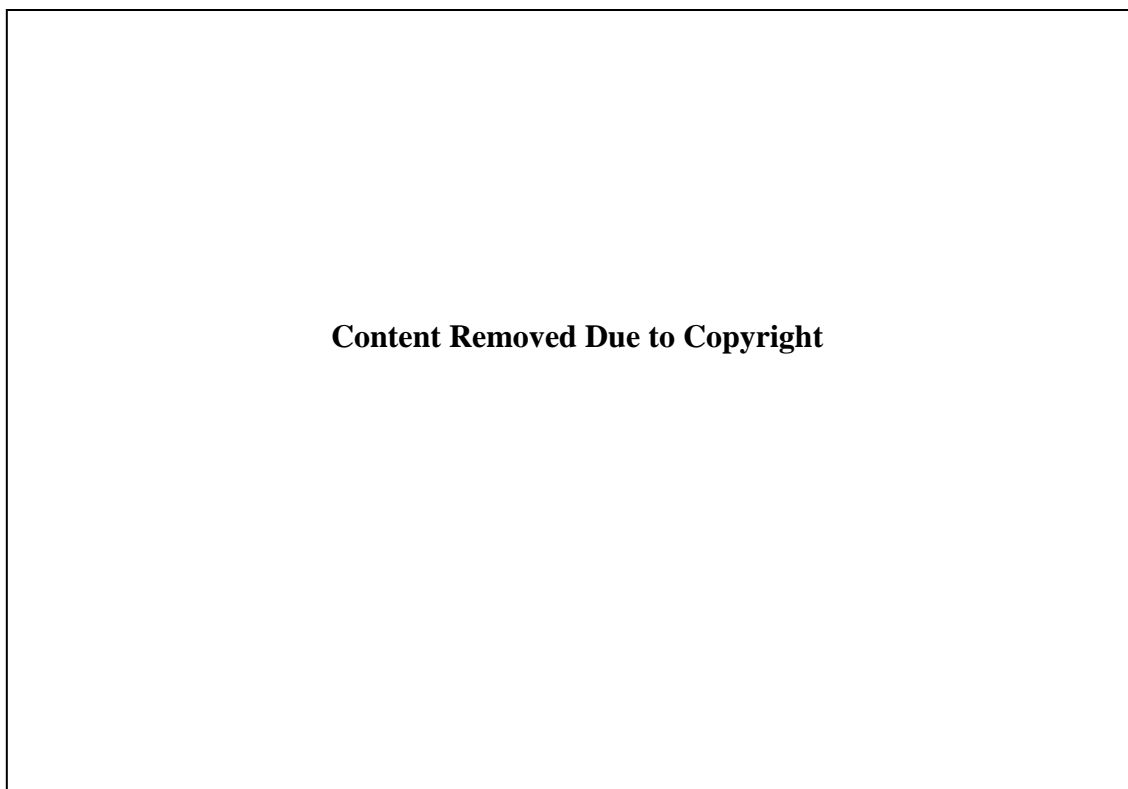


Figure 2.17 Course and fine thread screw designs investigated by Gausepohl et al. (2001)

A double threaded pedicle screw design was previously investigated by Mummaneni et al. (2002). An image of the double threaded design investigated compared a standard single thread is provide in Figure 2.18. An experimental investigation of the pullout strength of these designs found that the second smaller inner thread did not lead to an increase in either higher bone purchase or higher pullout strengths. However, it was noted that the insertion torque was 14.5% higher for the single threaded screw.



Figure 2.18 (A) Single and double thread design investigated by Mummaneni et al. (2002), (B) Comparison of pullout forces recorded for single and double screw designs

Alternative screw designs have been suggested by Goldhahn et al. (2005). These designs include more rounded edges and increasing the surface area of the implant in contact with the surrounding bone (Figure 2.19). Alternative methods of insertion were also investigated based on pneumatic / ultrasound vibrations. Finite element analysis of these new geometries revealed reduced stress on the surrounding bone. These are preliminary designs and no clinical data currently exists to validate their performance.



Figure 2.19 Alternate screw designs proposed by Goldhahn et al. (2005) offering reduced stress concentrations in bone. Image obtained from Goldhahn et al. (2005)

Orthopaedic screws are used as the primary mode of fixation for applications such as fracture plates (Kwon et al. (2002)), intramedullary rods (Cuny et al. (2008)), spinal devices (GainesJr (2000)) and suture anchors (Barber et al. (2008)). The ability of devices to perform as designed is dictated by pullout strength of the screws anchoring them. Pullout is a commonly reported clinical problem (Owsley and Gorczyca (2008)). The failure mechanisms leading to pullout have not previously been uncovered.

2.5 Biomaterials

The devices investigated in Chapter 4 are manufactured from titanium and stainless steel. Stainless steel was first implemented for a hip prosthesis in the late 1950s (Charnley (1960)). Stainless steel offers good corrosion resistance, however it has poor wear properties Navarro et al. (2008). Titanium is less stiff than stainless steel

with good corrosion resistance. Additionally, as reported by Brånemark et al. (1964) the porous microstructure of titanium facilitates bone ingrowth over time referred to as osteointegration. This ensures that the implant is held in position and maintains stability. Both stainless steel and titanium are significantly stiffer than cortical bone as shown in the graph of Figure 2.20 Other metals, such as cobalt chromium, tantalum and nitinol, are used to manufacture orthopaedic devices; however these materials were not investigated in the work presented in this thesis.

Given that 70% of proximal humeral fractures occur in patients over 60 years of age (Kettler et al. (2006)) the injury can be complicated by osteoporosis. Bone voids, resulting from osteoporosis, mean poor results for proximal humerus fractures. In cases where the reconstruction of the fracture fragments is not possible, a void filling bone graft may be used. Problems associated with bone grafts include limited availability and high cost. One option proposed to improve the performance of fracture fixation devices is to fill these bone voids with bone graft substitutes such as calcium phosphate cement. Histological studies of calcium phosphate showed that it is osteoconductive (Frankenburg et al. (1998)). An experimental study by Kwon et al. (2002) reported lower relative motion between fracture fragments when bone voids were filled with cement (reinforced fixation). A clinical study of cement reinforced fixation found that it lowered the prevalence of pain at the fracture site compared to an unfilled bone void (unreinforced fixation) (Kwon et al. (2002); Bajammal et al. (2008)).

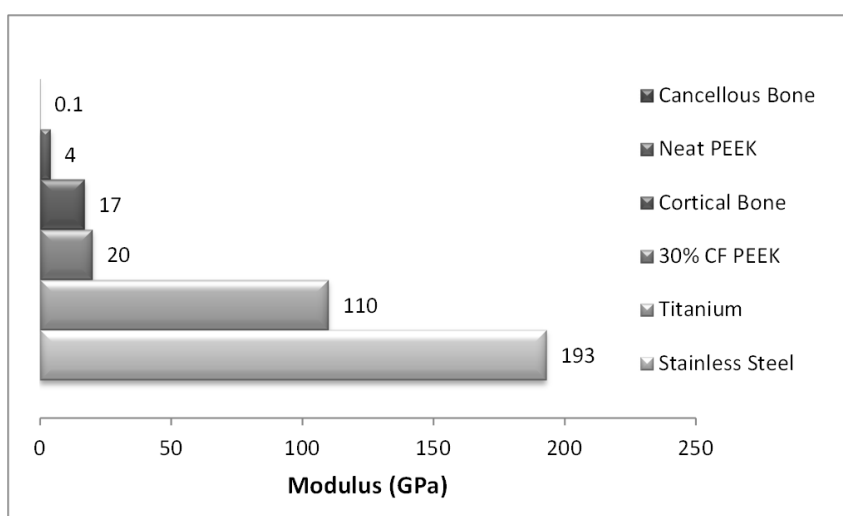


Figure 2.20 Elastic modulus of CF PEEK compared to the properties of bone, titanium and stainless steel.

Carbon fibre (CF) reinforced composites have been suggested as alternatives to metallic implants for several biomedical applications (Fujihara et al. (2004); Kurtz and Devine (2007); Kharazi et al. (2010)). CF reinforced composites can be tailored to have a significantly lower stiffness than metallic devices close to that of cortical bone. A summary of elastic modulus of carbon fibre peek is shown in Figure 2.20. Ponnappan et al. (2009) compared a carbon fibre reinforced polymer (polyetheretherketone (PEEK)) rod system to titanium for spinal applications. It was reported that PEEK provided a more flexible stabilisation, as well as offering the advantage of reduced stress at the bone screw interface. A summary of the ultimate strengths of unreinforced and reinforced PEEK is provided in Table 2.5. The fatigue properties of CFPEEK are also a concern as implanted devices will undergo millions of cycles of loading. Steinberg et al. (2013) demonstrated that the fatigue performance of CFPEEK proximal humeral plates satisfied ASTM standards for implanted devices.

Table 2.5 Unreinforced and reinforced PEEK mechanical properties (Kurtz and Devine (2007))

	Unreinforced PEEK	30% Short CF reinforced PEEK	68% Continuous CF reinforced PEEK
Flexural Modulus (GPa)	4	20	135
Tensile Strength (MPa)	93	170	>2000
Tensile Elongation (%)	30 - 40	1 - 2	1

Additionally, carbon fibre reinforced materials such as CFPEEK are radiolucent (Kurtz and Devine (2007)). This means fracture lines are easier to visualise with x-rays as there is no visible plate on the x-ray. CFPEEK devices are also MRI compatible as the artefact generated by metallic components makes interpretation of the MRI scan difficult (Ponnappan et al. (2009)). CFPEEK materials also prevent cold weather intolerance in patients, which has been reported for metallic devices (Kitsis et al. (2003)).

2.6 References

- Agneskirchner, J., Freiling, D., Hurschler, C. and Lobenhoffer, P., 2006. Primary stability of four different implants for opening wedge high tibial osteotomy. *Knee Surgery, Sports Traumatology, Arthroscopy* 14, 291-300.
- Agur, A. M. R. and Dalley, A. F., 2008. Grant's Atlas of Anatomy, Lippincott Williams & Wilkins.
- An, Y., Kang, Q. and Friedman, R., 1996. Mechanical symmetry of rabbit bones studied by bending and indentation testing. *American journal of veterinary research* 57, 1786-1789.
- An, Y. H. and Draughn, R. A., 1999. Mechanical Testing of Bone and the Bone-Implant Interface, Taylor & Francis.
- Ascenzi, A., Baschieri, P. and Benvenuti, A., 1990. The bending properties of single osteons. *Journal of Biomechanics* 23, 763-771.
- Ascenzi, A. and Bonucci, E., 1968. The compressive properties of single osteons. *The Anatomical Record* 161, 377-391.
- Ayers, R., Miller, M., Simske, S. and Norrdin, R., 1996. Correlation of flexural structural properties with bone physical properties: a four species survey. *Biomedical sciences instrumentation* 32, 251.
- Bajammal, S. S., Zlowodzki, M., Lelwica, A., Tornetta, P., Einhorn, T. A. and Buckley, R., 2008. The use of calcium phosphate bone cement in fracture treatment. *J Bone Joint Surg Am* 90, 1186-1196.
- Barber, F. A., Herbert, M. A., Beavis, R. C. and Barrera Oro, F., 2008. Suture Anchor Materials, Eyelets, and Designs: Update 2008. *Arthroscopy: The Journal of Arthroscopic & Related Surgery* 24, 859-867.
- Battula, S., Schoenfeld, A., Vrabec, G. and Njus, G. O., 2006. Experimental evaluation of the holding power/stiffness of the self-tapping bone screws in normal and osteoporotic bone material. *Clinical Biomechanics* 21, 533-537.
- Bayraktar, H. H., Morgan, E. F., Niebur, G. L., Morris, G. E., Wong, E. K. and Keaveny, T. M., 2004. Comparison of the elastic and yield properties of human femoral trabecular and cortical bone tissue. *Journal of Biomechanics* 37, 27-35.
- Brånemark, P., Breine, U., Johansson, B., Rooyance, P., Röckert, H. and Yoffey, J., 1964. Regeneration of bone marrow. *Cells Tissues Organs* 59, 1-46.
- Buchler, P., Farron, A., 2004. Benefits of an anatomical reconstruction of the humeral head during shoulder arthroplasty: a finite element analysis. *Clinical Biomechanics* 19, 16-23.
- Budyn, É. and Hoc, T., 2010. Analysis of micro fracture in human Haversian cortical bone under transverse tension using extended physical imaging. *International Journal for Numerical Methods in Engineering* 82, 940-965.
- Burstein, A. H., Reilly, D. T. and Martens, M., 1976. Aging of bone tissue: Mechanical properties. *J Bone Joint Surg Am* 58, 82.
- Chapman, J. R., Harrington, R. M., Lee, K. M., Anderson, P. A., Tencer, A. F. and Kowalski, D., 1996. Factors Affecting the Pullout Strength of Cancellous Bone Screws. *Journal of Biomechanical Engineering* 118, 391-398.
- Charnley, J., 1960. Anchorage of the femoral head prosthesis to the shaft of the femur. *Journal of Bone and Joint Surgery-British Volume* 42, 28.
- Choi, K., Kuhn, J. L., Ciarelli, M. J. and Goldstein, S. A., 1990. The elastic moduli of human subchondral, trabecular, and cortical bone tissue and the size-

- dependency of cortical bone modulus. *Journal of Biomechanics* 23, 1103-1113.
- Clavert, P., Zerah, M., Krier, J., Mille, P., Kempf, J. and Kahn, J., 2006. Finite element analysis of the strain distribution in the humeral head tubercles during abduction: comparison of young and osteoporotic bone. *Surg Radiol Anat* 28, 581-587.
- Cristofolini, L. and Viceconti, M., 2000. Mechanical validation of whole bone composite tibia models. *Journal of Biomechanics* 33, 279-288.
- Cristofolini, L., Viceconti, M., Cappello, A. and Toni, A., 1996. Mechanical validation of whole bone composite femur models. *Journal of Biomechanics* 29, 525-535.
- Cuny, C., Scarlat, M. M., Irrazi, M., Beau, P., Wenger, V., Ionescu, N. and Berrichi, A., 2008. The Telegraph nail for proximal humeral fractures: A prospective four-year study. *J Shoulder Elbow Surg* 17, 539-545.
- Currey, J., 1998. Mechanical properties of vertebrate hard tissues. *Proceedings of the Institution of Mechanical Engineers, Part H: Journal of Engineering in Medicine* 212, 399-411.
- Currey, J. D., 1988. The effect of porosity and mineral content on the Young's modulus of elasticity of compact bone. *Journal of Biomechanics* 21, 131-139.
- Currey, J. D., 2002. *Bones Structure and Mechanics*, Princeton University Press.
- Dickenson, R. P., Hutton, W. C. and Stott, J. R., 1981. The mechanical properties of bone in osteoporosis. *Journal of Bone and Joint Surgery-British Volume* 63, 233-38.
- Doursounian, L., Grimberg, J., Cazeau, C., Jos, E. and Touzard, R., 2000. A new internal fixation technique for fractures of the proximal humerus-the Bilboquet device: A report on 26 cases. *J Shoulder Elbow Surg* 9, 279-288.
- Drucker, D. and Prager, W., 1952. Soil Mechanics and Plastic Analysis or Limit Design. *Quarterly of applied mathematics* 10, 157.
- Erkan, S., Hsu, B., Wu, C., Mehbod, A., Perl, J. and Transfeldt, E., 2010. Alignment of pedicle screws with pilot holes: can tapping improve screw trajectory in thoracic spines? *European Spine Journal* 19, 71-77.
- Feng, Z., Rho, J., Han, S. and Ziv, I., 2000. Orientation and loading condition dependence of fracture toughness in cortical bone. *Materials Science and Engineering: C* 11, 41-46.
- Frankenburg, E. P., Goldstein, S. A., Bauer, T. W., Harris, S. A. and Poser, R. D., 1998. Biomechanical and histological evaluation of a calcium phosphate cement. *J Bone Joint Surg Am* 80, 1112-1124.
- Fujihara, K., Huang, Z. M., Ramakrishna, S., Satknanantham, K. and Hamada, H., 2004. Feasibility of knitted carbon/PEEK composites for orthopedic bone plates. *Biomaterials* 25, 3877-3885.
- Gaines Jr, R. W., 2000. The Use of Pedicle-Screw Internal Fixation for the Operative Treatment of Spinal Disorders. *The Journal of Bone and Joint Surgery (American)* 82, 1458-1458.
- Gausepohl, T., Möhring, R., Pennig, D. and Koebke, J., 2001. Fine thread versus coarse thread: A comparison of the maximum holding power. *Injury* 32, Supplement 4, 1-7.
- Gefen, A., 2002. Computational simulations of stress shielding and bone resorption around existing and computer-designed orthopaedic screws. *Medical and Biological Engineering and Computing* 40, 311-322.

- Goldhahn, J., Seebeck, J., Frei, R., Frenz, B., Antoniadis, I. and Schneider, E., 2005. New implant designs for fracture fixation in osteoporotic bone. *Osteoporosis International* 16, S112-S119.
- Grover, P., Albert, C., Wang, M. and Harris, G. F., 2011. Mechanical characterization of fourth generation composite humerus. *Proceedings of the Institution of Mechanical Engineers, Part H: Journal of Engineering in Medicine* 225, 1169-1176.
- Hägg, O. and Lundberg, B., 1984. Aspects of prognostic factors in comminuted and dislocated proximal humeral fractures. *Surgery of the shoulder*. Philadelphia: BC Decker, 51-59.
- Johnell, O. and Kanis, J., 2006. An estimate of the worldwide prevalence and disability associated with osteoporotic fractures. *Osteoporosis International* 17, 1726-1733.
- Johnson, A. J., 2007. Humeral Fracture Fixation Techniques: A FEA Comparison of Locking and Compression Techniques with Cadaveric Pullout Comparison of Cortical Compression and Internal Locking Screws, University of Maryland, College Park.
- Keaveny, T. M., Pinilla, T. P., Crawford, R. P., Kopperdahl, D. L. and Lou, A., 1997. Systematic and random errors in compression testing of trabecular bone. *Journal of Orthopaedic Research* 15, 101-110.
- Kettler, M., Biberthaler, P., Braunstein, V., Zeiler, C., Kroetz, M. and Mutschler, W., 2006. Treatment of proximal humeral fractures with the PHILOS angular stable plate. Presentation of 225 cases of dislocated fractures. *Der Unfallchirurg* 109, 1032-40.
- Kharazi, A. Z., Fathi, M. H. and Bahmany, F., 2010. Design of a textile composite bone plate using 3D-finite element method. *Materials & Design* 31, 1468-1474.
- Kincaid, B., Schroder, L. and Mason, J., 2007. Measurement of Orthopedic Cortical Bone Screw Insertion Performance in Cadaver Bone and Model Materials. *Experimental Mechanics* 47, 595-607.
- Kitsis, C. K., Marino, A. J., Krikler, S. J. and Birch, R., 2003. Late complications following clavicular fractures and their operative management. *Injury* 34, 69-74.
- Ko, R., 1953. The tension test upon the compact substance of the long bones of human extremities. *J Kyoto Pref Med Univ* 53, 503.
- Koike, Y., Komatsuda, T. and Sato, K., 2008. Internal fixation of proximal humeral fractures with a Polarus humeral nail. *J Orthopaed Traumatol* 9, 135-139.
- Koval, K. J., Blair, B., Takei, R., Kummer, F. J. and Zuckerman, J. D., 1996. Surgical neck fractures of the proximal humerus: a laboratory evaluation of ten fixation techniques. *J Trauma* 40, 778-83.
- Koval, K. J., Gallagher, M. A., Marsicano, J. G., Cuomo, F., McShinawy, A. and Zuckerman, J. D., 1997. Functional Outcome after Minimally Displaced Fractures of the Proximal Part of the Humerus*. *The Journal of Bone and Joint Surgery (American)* 79, 203-7.
- Kuhn, J. L., Goldstein, S. A., Ciarelli, M. J. and Matthews, L. S., 1989. The limitations of canine trabecular bone as a model for human: A biomechanical study. *Journal of Biomechanics* 22, 95-107.
- Kurtz, S. M. and Devine, J. N., 2007. PEEK biomaterials in trauma, orthopedic, and spinal implants. *Biomaterials* 28, 4845-4869.

- Kutz, M., 2003. Standard Handbook of Biomedical Engineering and Design, McGraw-Hill. 8.1-8.23.
- Kwon, B. K., Goertzen, D. J., O'Brien, P. J., Broekhuysse, H. M. and Oxland, T. R., 2002. Biomechanical evaluation of proximal humeral fracture fixation supplemented with calcium phosphate cement. *J Bone Joint Surg Am* 84, 951-61.
- Liebschner, M. and Keller, T., 2005. Hydraulic Strengthening Affects the Stiffness and Strength of Cortical Bone. *Annals of Biomedical Engineering* 33, 26-38.
- Liebschner, M. A. K., 2004. Biomechanical considerations of animal models used in tissue engineering of bone. *Biomaterials* 25, 1697-1714.
- Linde, F., Hvid, I. and Pongsoipetch, B., 1989. Energy absorptive properties of human trabecular bone specimens during axial compression. *Journal of Orthopaedic Research* 7, 432-439.
- Maldonado, Z. M., Seebeck, J., Heller, M. O. W., Brandt, D., Hepp, P., Lill, H. and Duda, G. N., 2003. Straining of the intact and fractured proximal humerus under physiological-like loading. *J Biomech* 36, 1865-1873.
- Martens, M., Van Audekercke, R., Delpont, P., De Meester, P. and Mulier, J. C., 1983. The mechanical characteristics of cancellous bone at the upper femoral region. *Journal of Biomechanics* 16, 971-983.
- McNamara, L., 2011. Bone as a Material. *Comprehensive Biomaterials*, Elsevier. 169-186.
- Mercer, C., He, M. Y., Wang, R. and Evans, A. G., 2006. Mechanisms governing the inelastic deformation of cortical bone and application to trabecular bone. *Acta Biomaterialia* 2, 59-68.
- Morgan, E.F., Keaveney, T.M., 2001. Dependence of yield strain of human trabecular bone on anatomic site. *Journal of Biomechanics* 34, 569-577.
- Muckter, H., Herzog, L., Becker, M., Vogel, W., Meeder, P. J. and Buchholz, J., 2001. Angle- and rotation-stable internal fixation of proximal humerus fractures with the humerus fixator plate. Early clinical experience with a newly developed implant. *Der Chirurg; Zeitschrift für alle Gebiete der operativen Medizin* 72, 1327-35.
- Mullins, L. P., Bruzzi, M. S. and McHugh, P. E., 2009. Calibration of a constitutive model for the post-yield behaviour of cortical bone. *Journal of the Mechanical Behavior of Biomedical Materials* 2, 460-470.
- Mummaneni, P.V., Haddock, S.M., Liebschner, M.A.K., Keaveney, T.M., Rosenberg, W.S., 2002. *Journal of Spinal Disorders & Techniques* 15, 64-68.
- Nalla, R. K., Kinney, J. H. and Ritchie, R. O., 2003. Mechanistic fracture criteria for the failure of human cortical bone. *Nat Mater* 2, 164-168.
- Nalla, R. K., Kruzic, J. J. and Ritchie, R. O., 2004. On the origin of the toughness of mineralized tissue: microcracking or crack bridging? *Bone* 34, 790-798.
- Navarro, M., Michiardi, A., Castaño, O. and Planell, J. A., 2008. Biomaterials in orthopaedics. *Journal of The Royal Society Interface* 5, 1137-1158.
- Norman, T. L., Nivargikar, S. V. and Burr, D. B., 1996. Resistance to crack growth in human cortical bone is greater in shear than in tension. *Journal of Biomechanics* 29, 1023-1031.
- Olvera, D., Zimmermann, E. A. and Ritchie, R. O., 2012. Mixed-mode toughness of human cortical bone containing a longitudinal crack in far-field compression. *Bone* 50, 331-336.

- Owsley, K. C. and Gorczyca, J. T., 2008. Displacement/Screw Cutout After Open Reduction and Locked Plate Fixation of Humeral Fractures. *J Bone Joint Surg Am* 90, 233-240.
- PacificResearchLaboratories. (2012). "Sawbones Biomechanical Test Materials". Retrieved June 2012, 2012, from <http://www.sawbones.com/products/bio/default.aspx>.
- Ponnappan, R. K., Serhan, H., Zarda, B., Patel, R., Albert, T. and Vaccaro, A. R., 2009. Biomechanical evaluation and comparison of polyetheretherketone rod system to traditional titanium rod fixation. *The Spine Journal* 9, 263-267.
- Reilly, D. T. and Burstein, A. H., 1974. The Mechanical Properties of Cortical Bone. *The Journal of Bone & Joint Surgery* 56, 1001-1022.
- Reilly, D. T. and Burstein, A. H., 1975. The elastic and ultimate properties of compact bone tissue. *Journal of Biomechanics* 8, 393-396, IN9-IN11, 397-405.
- Resch, H., Povacz, P., Frohlich, R. and Wambacher, M., 1997. Percutaneous fixation of three-and four-part fractures of the proximal humerus. *J Bone Joint Surg Br* 79, 295-300.
- Rho, J.-Y., Kuhn-Spearing, L. and Zioupos, P., 1998. Mechanical properties and the hierarchical structure of bone. *Medical Engineering & Physics* 20, 92-102.
- Ritchie, R., Kinney, J., Kruzic, J. and Nalla, R., 2006. Cortical bone fracture. *Wiley Encyclopedia of Biomedical Engineering*.
- Roberts, J. W., Grindel, S. I., Rebholz, B. and Wang, M., 2007. Biomechanical Evaluation of Locking Plate Radial Shaft Fixation: Unicortical Locking Fixation Versus Mixed Bicortical and Unicortical Fixation in a Sawbone Model. *The Journal of Hand Surgery* 32, 971-975.
- Rose, P. S., Adams, C. R., Torchia, M. E., Jacofsky, D. J., Haidukewych, G. G. and Steinmann, S. P., 2007. Locking plate fixation for proximal humeral fractures: initial results with a new implant. *J Shoulder Elbow Surg* 16, 202-207.
- Schryver, H., 1978. Bending properties of cortical bone of the horse. *American journal of veterinary research* 39, 25.
- Shuib, S., Ridzwan, M., Mohamad Ibrahim, M. and Tan, C., 2007. Analysis of Orthopedic Screws for Bone Fracture Fixations with Finite Element Method. *Journal of Applied Sciences* 7, 1748-1754.
- Simkin, A. and Robin, G., 1973. The mechanical testing of bone in bending. *Journal of Biomechanics* 6, 31-39.
- Sperling, J. W., Cofield, R. H. and Rowland, C. M., 2004. Minimum fifteen-year follow-up of Neer hemiarthroplasty and total shoulder arthroplasty in patients aged fifty years or younger. *Journal of Shoulder and Elbow Surgery* 13, 604-613.
- Steinberg, E.L., Rath, E., Shlaifer, A., Chechik, O., Maman, E., Salai, M., 2013. Carbon fiber reinforced PEEK Optima—A composite material biomechanical properties and wear/debris characteristics of CF-PEEK composites for orthopedic trauma implants. *Journal of the Mechanical Behavior of Biomedical Materials* 17, 221-228.
- Tan, J. S., Bailey, C. S., Dvorak, M. F., Fisher, C. G., Cripton, P. A. and Oxland, T. R., 2007. Cement augmentation of vertebral screws enhances the interface strength between interbody device and vertebral body. *Spine* 32, 334.

- Weatherholt, A. M., Fuchs, R. K. and Warden, S. J., 2012. Specialized Connective Tissue: Bone, the Structural Framework of the Upper Extremity. *Journal of Hand Therapy* 25, 123-132.
- Webb, J.D., Blemker, S.S, Delp, S.L., 2012. 3D finite element models of shoulder muscles for computing lines of actions and moment arms. *Computer Methods in Biomechanics and Biomedical Engineering*. Article in Press.
- Wen-Chi, T., Po-Quang, C., Tung-Wu, L., Shing-Sheng, W., Kao-Shang, S. and Shang-Chih, L., 2009. Comparison and prediction of pullout strength of conical and cylindrical pedicle screws within synthetic bone. *BMC Musculoskeletal Disorders* 10.
- Zimmermann, E. A., Launey, M. E., Barth, H. D. and Ritchie, R. O., 2009. Mixed-mode fracture of human cortical bone. *Biomaterials* 30, 5877-5884.
- Zimmermann, E. A., Launey, M. E. and Ritchie, R. O., 2010. The significance of crack-resistance curves to the mixed-mode fracture toughness of human cortical bone. *Biomaterials* 31, 5297-5305.
- Zioupos, P. and Currey, J. D., 1998. Changes in the Stiffness, Strength, and Toughness of Human Cortical Bone With Age. *Bone* 22, 57-66.

Chapter 3

Theory

3.1 Introduction

The theoretical basis of the computational work presented in Chapters four, six and seven are outlined in the current chapter. The definitions and governing equations for the material models are provided for elasticity and plasticity with a focus on the extended Drucker Prager model. The computational modelling techniques for two methods of fracture are also outlined, namely element deletion, and the extended finite element method (XFEM). Both implicit and explicit finite element solution schemes (Abaqus Standard and Abaqus Explicit) are utilised in this thesis. Both schemes are outlined, highlighting the advantages and disadvantages of each solution scheme. Notation used within this thesis is Table 3.1.

Table 3.1: Notation summary used in the present thesis

Notation Type	Example
A scalar value written in italics	<i>a</i>
A vector written in bold or unbold inside square brackets	a or [a]
A vector with a transpose	a ^T
A second order tensor in bold	a
A second order tensor with Transpose	a ^T or [a] ^T

For example, the dot product of two components in 3D is written as follows:

$$\mathbf{u} \cdot \mathbf{v} = u_1 v_1 + u_2 v_2 + u_3 v_3 = \sum_i^3 u_i v_i = c \quad (3.1)$$

The cross product of two vectors is written as follows:

$$\mathbf{u} \times \mathbf{v} = (u_1 i + u_2 j + u_3 k) \times (v_1 i + v_2 j + v_3 k) = \mathbf{c} \quad (3.2)$$

3.2 Deformation (Measuring Stress and Strain)

In the computational simulations performed in this work, finite deformation kinematics is assumed. The position vectors, \mathbf{X} and \mathbf{x} , define a material point in the reference (or undeformed) and current (or deformed) configurations, respectively. Essentially, when a body is subjected to a stress, a particle of that body may move from an original position in space (\mathbf{X}) to a new position in space (\mathbf{x}). The path or history of positions of a particle can be written relative to time as follows:

$$\mathbf{x} = \mathbf{x}(\mathbf{X}, t) \quad (3.3)$$

The displacement vector of the material point is given as

$$\mathbf{u}(\mathbf{x}, t) = \mathbf{x}(\mathbf{X}, t) - \mathbf{X} \quad (3.4)$$

Consider two neighbouring particles, with initial positions located at positions \mathbf{X} and $\mathbf{X} + d\mathbf{X}$. The deformation gradient tensor, \mathbf{F} , relates the difference in particle position in the current configuration, $d\mathbf{x}$, to that reference configuration, $d\mathbf{X}$

$$d\mathbf{x} = \mathbf{F} \cdot \frac{\partial \mathbf{x}}{\partial \mathbf{X}} \quad \text{and} \quad \mathbf{F} = \frac{\partial \mathbf{x}}{\partial \mathbf{X}} \quad (3.5)$$

The deformation of materials is generally path dependent and so the constitutive relationships are defined in terms of time (rate form). The velocity of a particle is defined in equation 3.6. This defines the rate of change of the spatial position \mathbf{x} as a function of time for a specific material particle.

$$\mathbf{v} = \frac{\partial \mathbf{x}}{\partial t} \quad (3.6)$$

The velocity difference between two neighbouring particles is given in equation 3.7.

$$d\mathbf{v} = \frac{\partial \mathbf{v}}{\partial \mathbf{x}} \cdot d\mathbf{x} = \mathbf{L} \cdot d\mathbf{x} \quad (3.7)$$

where, \mathbf{L} is referred to as the velocity gradient.

$$\mathbf{L} = \frac{\partial \mathbf{v}}{\partial \mathbf{x}} \quad (3.8)$$

Relating this to the deformation gradient \mathbf{F} in equation 3.9

$$d\mathbf{v} = \mathbf{L} \cdot d\mathbf{x} = \mathbf{L} \cdot \mathbf{F} \cdot d\mathbf{X} \quad (3.9)$$

Therefore the velocity difference ($d\mathbf{v}$) between two neighbouring particles can be obtained using equation 3.10.

$$d\mathbf{v} = \frac{\partial}{\partial t} (\mathbf{F} \cdot d\mathbf{X}) = \dot{\mathbf{F}} \cdot d\mathbf{X} \quad (3.10)$$

The relative distance between the two particles ($d\mathbf{X}$) remains the same throughout the particle motion and therefore $d\mathbf{X}$ has no time derivative. Comparing the two formulations for $d\mathbf{v}$ from equations 3.9 and 3.10 in terms of the relative distance between particles ($d\mathbf{X}$) (equation 3.11).

$$\mathbf{L} \cdot \mathbf{F} = \dot{\mathbf{F}} \text{ or } \mathbf{L} = \dot{\mathbf{F}} \cdot \mathbf{F}^{-1} \quad (3.11)$$

The velocity gradient (\mathbf{L}) consists of two components, a symmetric strain rate tensor (\mathbf{D}) and an anti-symmetric rotation or spin tensor (\mathbf{W}). The velocity gradient is the sum of these two ($\mathbf{L}=\mathbf{D}+\mathbf{W}$).

$$\mathbf{D} = \dot{\epsilon} = \text{sym}(\mathbf{L}) = \frac{1}{2} (\mathbf{L}^T + \mathbf{L}) \quad (3.12)$$

$$\mathbf{W} = \text{asym}(\mathbf{L}) = \frac{1}{2} (\mathbf{L}^T - \mathbf{L}) \quad (3.13)$$

The integration of \mathbf{D} (equation 3.12) with respect to time, gives the logarithmic strain tensor ($\boldsymbol{\epsilon}(t)$). Equation 3.14 can be used in the calculation of finite strain.

$$\boldsymbol{\epsilon}(t) = \int_0^t \mathbf{D} dt \quad (3.14)$$

Stress calculated and reported in this thesis unless otherwise stated is the Cauchy “true” stress ($\boldsymbol{\sigma}$). It is defined as the force per unit area for the current level of deformation of a body. It can be decomposed into two parts; the hydrostatic stress which governs volume change of a body and deviatoric stress which governs shape change of a body. These individual components will be discussed further for the description of the Drucker Prager yield criterion. The stress tensor is symmetric ($\boldsymbol{\sigma} = \boldsymbol{\sigma}^T$) and related to the traction (\mathbf{t}) on an internal or external surface of the current configuration of a body and a normal vector to the surface of that body (\mathbf{n}).

$$\mathbf{t} = \boldsymbol{\sigma} \cdot \mathbf{n} \quad (3.15)$$

The current stress state of a body can be defined as the sum of the mean normal ($\boldsymbol{\sigma}_m$) and deviatoric (\mathbf{S}) stress (equation 3.16).

$$\boldsymbol{\sigma} = \boldsymbol{\sigma}_m + \mathbf{S} = p\boldsymbol{\delta} + \mathbf{S} \quad (3.16)$$

where, the mean normal stress ($\boldsymbol{\sigma}_m$) is a product of the mean hydrostatic pressure (p) and the kronecker delta ($\boldsymbol{\delta}$). $\boldsymbol{\delta}$ is equal to 1 if $i = j$, and 0 if $i \neq j$.

$$p = \frac{\sigma_{xx} + \sigma_{yy} + \sigma_{zz}}{3} = \frac{\text{trace}(\boldsymbol{\sigma})}{3} \quad (3.17)$$

3.3 Elasto-Plasticity

Abaqus defines elasto-plastic deformation of a material as two components, an elastic component (\mathbf{F}^{el} ; consisting of recoverable deformation) and a plastic component (\mathbf{F}^{pl} ; consisting of permanent deformation).

$$\mathbf{F} = \mathbf{F}^{el} \cdot \mathbf{F}^{pl} \quad (3.18)$$

The total strain rate of the material is also considered as a combination of elastic and plastic strain rates as shown in equation 3.19.

$$\dot{\boldsymbol{\varepsilon}} = \dot{\boldsymbol{\varepsilon}}^{el} + \dot{\boldsymbol{\varepsilon}}^{pl} \quad (3.19)$$

Integrating equation 3.19 with respect to time gives the corresponding elastic and plastic strains (equation 3.20).

$$\boldsymbol{\varepsilon} = \boldsymbol{\varepsilon}^{el} + \boldsymbol{\varepsilon}^{pl} \quad (3.20)$$

If considering a material as linear isotropic elastic then the elasticity can be written in terms of two material constants; the bulk modulus (K) and the Shear Modulus (G). These are calculated in terms of the Young's modulus (E) and the Poisson's ratio (ν).

$$K = \frac{E}{3(1 - 2\nu)} \quad (3.21)$$

$$G = \frac{E}{2(1 + \nu)} \quad (3.22)$$

Hooke's law relates the current stress state of a body ($\boldsymbol{\sigma}$) to the deformation strain ($\boldsymbol{\varepsilon}$) of the stiffness of the body according to the elasticity tensor (\mathbf{C}).

$$\boldsymbol{\sigma} = \mathbf{C} \boldsymbol{\varepsilon} \quad (3.23)$$

In the case of isotropic elasticity the 36 components of \mathbf{C} can simply be defined in terms of the two variables (Young's modulus (E) and the Poisson's ratio (ν)). In the case of anisotropic elasticity the 36 components of \mathbf{C} can be defined in terms of 21 independent constants. An orthotropic material can be defined in terms of 9 independent components. This is further reduced to 5 components in the case of a transversely isotropic material.

Plastic deformation/ yield of cortical bone in this thesis is defined using the linear Drucker Prager plasticity model. This model was first introduced by Drucker and Prager (1952). The adapted linear Drucker Prager model is used to model frictional materials that have higher yield strength in compression than tension (Abaqus (2009)). The model is isotropic. It predicts a non-circular yield surface in the deviatoric plane in order to predict alternate yield strengths in tension and compression. The yield surface is defined in terms of both the Von Mises equivalent stress (q) and the equivalent pressure (p) (equation 3.17).

$$F = t - p \tan \beta - d = 0 \quad (3.24)$$

where, the Drucker Prager deviatoric stress measure t is defined in equation 3.25.

$$t = \frac{1}{2} q \left[1 + \frac{1}{K} - \left(1 - \frac{1}{K} \right) \left(\frac{r}{q} \right)^3 \right] \quad (3.25)$$

$$r = \left(\frac{9}{2} \mathbf{S} \cdot \mathbf{S} \cdot \mathbf{S} \right) \quad (3.26)$$

where, β is the slope of the linear yield surface in the p - t plane and is referred to as the friction angle of the material (Figure 3.1). d is the cohesion of the material (equation 3.27-3.29), r is the third invariant of deviatoric stress. K is the flow stress ratio between yield stress in triaxial tension and triaxial compression.

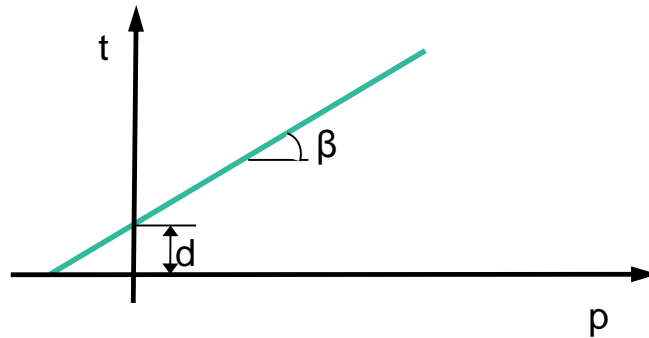


Figure 3.1: Linear yield surface for the Drucker-Prager plasticity formulation in the p - t plane.

$$d = \left(1 - \frac{1}{3} \tan \beta \right) \sigma_c \quad (3.27)$$

Or
$$d = \left(\frac{1}{K} + \frac{1}{3} \tan \beta \right) \sigma_t \quad (3.28)$$

Or
$$d = \left(\frac{\sqrt{3}}{2} \tau \left(1 + \frac{1}{K} \right) \right) \quad (3.29)$$

where the cohesion of the material can be defined in terms of uniaxial compression (σ_c), uniaxial tension (σ_t) or the shear yield stress (τ).

Plastic flow of the material is governed by the flow potential G .

$$G = t - p \tan \varphi \quad (3.30)$$

Where, ψ is the dilation angle in the p - t plane. The previously calibrated Drucker Prager parameters reported for bovine cortical bone were: $K=1$, $\beta=43.5^\circ$, $\psi=0$ Mercer et al. (2006). For $\psi=0$, no dilation occurs.

3.4 Damage Modelling

3.4.1 Damage Modelling with Element Deletion

Crack initiation and propagation is simulated in Chapter 6 using the integrated damage initiation and evolution criteria in Abaqus 6.9 Explicit. Damage is characterised by material degradation beyond a defined yield stress, once the material is fully degraded an option to remove the element from the mesh is available to simulate crack propagation. The graph of Figure 3.2 summarises the process of damage initiation and evolution for cortical bone. Once a defined critical yield stress (σ_{yDI}) and equivalent plastic strain ($\bar{\epsilon}_{DI}^{pl}$) are reached damage is initiated ($D = 0$). Further deformation beyond this point leads to a reduction in stiffness and strength until the defined equivalent plastic strain at failure is reached, at this point ($D = 1$) the element is removed from the mesh.

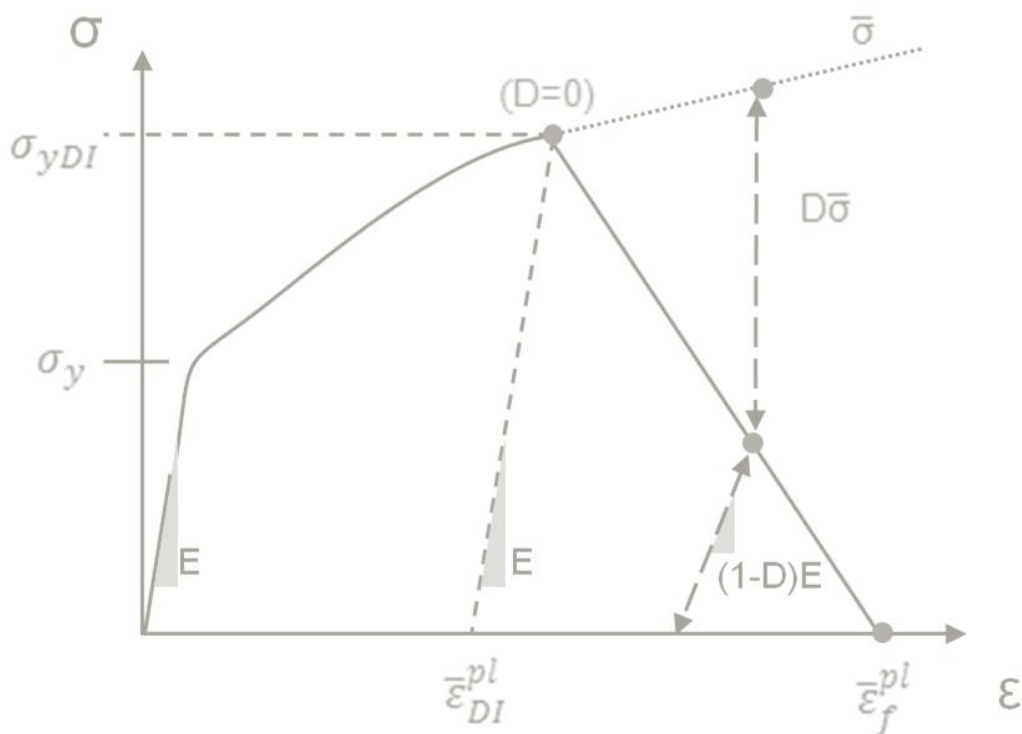


Figure 3.2 Process of damage initiation and evolution for cortical bone to simulate crack initiation and propagation during screw pullout.

The damage initiation criterion implemented in Chapter 6 is a shear based criterion. Equivalent plastic strain at the onset of damage is a function of shear stress ratio and plastic strain rate ($\bar{\epsilon}_s^{pl}(\theta_s, \dot{\epsilon}^{pl})$). Once the current equivalent plastic strain reaches the

defined critical value then the initiation criteria equals 1 ($\omega = 1$). At this point damage has been initiated so the damage variable equals 0 ($D = 0$).

$$\omega = \int \frac{d\bar{\varepsilon}^{pl}}{\bar{\varepsilon}_s^{pl}(\theta_s, \dot{\bar{\varepsilon}}^{pl})} = 1 \quad (3.31)$$

The definition of the softening response as damage evolves is based on the fracture energy (G_f). The fracture energy defined in terms of a stress displacement response is based on Hillerborg et al. (1976). The equivalent plastic displacement (\bar{u}^{pl}) is defined in terms of an element's characteristic length (L) and equivalent plastic strain ($\bar{\varepsilon}^{pl}$). The characteristic length L is determined based upon the average line across an element for a first order element.

$$G_f = \int_{\bar{\varepsilon}_0^{pl}}^{\bar{\varepsilon}_f^{pl}} L \sigma_y d\bar{\varepsilon}^{pl} = \int_0^{\bar{u}^{pl}} \sigma_y d\bar{u}^{pl} \quad (3.32)$$

A linear damage evolution is defined in terms of the plastic displacement (\bar{u}^{pl}) at failure and the damage variable (D). When \bar{u}^{pl} reaches the critical defined magnitude for plastic displacement at failure the damage variable reaches the value 1 ($D = 1$) and the element is removed from the mesh.

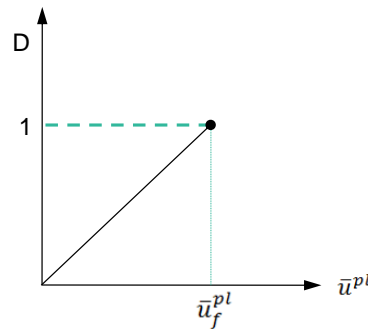


Figure 3.3 Graph of linear relationship between damage variable (D) and the plastic displacement (\bar{u}^{pl})

$$D = \frac{L\bar{\varepsilon}^{pl}}{\bar{u}_f^{pl}} = \frac{\bar{u}^{pl}}{\bar{u}_f^{pl}} \quad (3.33)$$

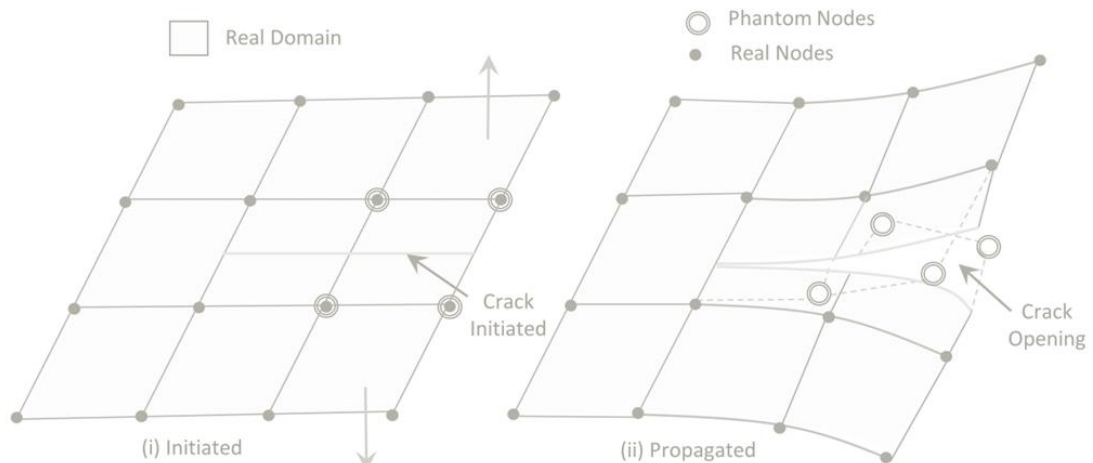
3.4.2 Damage Modelling with the Extended Finite Element Method (XFEM)

The extended finite element method (XFEM) implemented in Chapter 7 was developed for computationally modelling crack initiation and propagation without the need for adaptive remeshing (Melenk and Babuška (1996); Sukumar et al. (2004); Song et al. (2006); Abaqus (2012)). In contrast to the element deletion method, crack propagation using the XFEM method involves splitting elements rather than removing them from the mesh. Additionally, unlike cohesive zone modelling in which a crack path is predefined, XFEM can be used to predict crack initiation and propagation along an arbitrary, solution dependent path. A process of damage initiation and evolution are implemented to simulate fracture opening. Discontinuous functions are added to the conventional finite element nodal functions with additional degrees of freedom. XFEM can be used to model stationary or moving cracks. The work presented in Chapter 7 of this thesis focuses on the modelling of moving cracks. Damage initiation is predicted according to a defined anisotropic failure criterion outlined in Chapter 7. Damage evolution is simulated using the integrated energy based damage evolution in Abaqus 6.12 Standard.

The addition of nodal functions to the conventional finite element nodal displacement vector is shown in equation 3.34. $N_I(x)$ is the conventional nodal shape function. u_I is the standard nodal displacement vector associated with a node without XFEM. $H(x)a_I$ is the product of the enriched degrees of freedom vector (a_I) and the associated discontinuous jump function across the crack surface ($H(x)$).

$$u = \sum_{I=1}^N N_I(x)[u_I + H(x)a_I] \quad (3.34)$$

When modelling a moving crack using XFEM the assumption that a crack propagates across an entire element at a time is made. A phantom node method in conjunction with a fracture energy definition of bond strength between split elements is used to model the propagation of cracks through the mesh. The principle of the phantom node method is shown in Figure 3.4



Feerick et al. (2013) JMBBM, Article In Press, <http://dx.doi.org/10.1016/j.jmbbm.2012.12.004>

Figure 3.4 (i) Cracked elements once damage is initiated, with phantom nodes in the same location as real nodes; (ii) Crack opening occurs when strain energy dissipation reaches the defined critical value. Phantom and real nodes displace independently of one another

Once damage is initiated the damage variable equals zero ($D = 0$). A cracked element is shown in Figure 3.4(i). Crack propagation and crack opening is modelled using a phantom node method. As shown in Figure 3.4(i), when a crack is initiated in an element, phantom nodes (with additional degrees of freedom) are located at the same location as the real nodes. A linear energy based damage evolution law was defined for each of the failure criteria. The area under the graph of Figure 3.5 is the fracture dissipation energy required to propagate the crack. When damage initiates, the two surfaces of the cracked element are held together by equal and opposite forces referred to as the traction strength (T) (Figure 3.5). The traction strength (T) is degraded linearly over the separation (δ) of the two surfaces. The traction strength (T_{max}) of the split element surfaces is determined by the user defined fracture energy required to propagate the crack (G_f).

$$T_{max} = \frac{2G_f}{\delta_{max}} \quad (3.35)$$

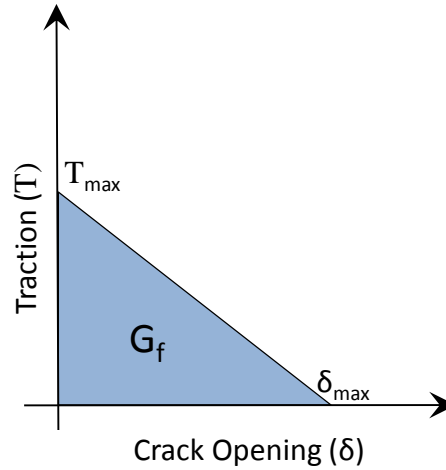


Figure 3.5 Linear degradation of traction strength between crack surfaces, area under the graph is the fracture energy required to propagate the crack (G_f)

When the fracture dissipation energy reaches the defined critical value then the split element fragments are free to displace independently of one another. Crack opening is shown in Figure 3.4(ii), with phantom nodes displacing away from real node locations. Small sliding contact is implemented between newly exposed surfaces.

3.5 Abaqus Standard (Implicit) vs Explicit Modelling

Implicit modelling means that the current state of a body at $t + \Delta t$ is determined by the information available at $t + \Delta t$. In contrast with this explicit modelling means that the current state of a body at $t + \Delta t$ is determined by the information available at t .

3.5.1 Implicit Modelling

Implicit modelling (i.e. Abaqus Standard) uses the implicit Hilber-Hughes-Taylor operator for the integration of equations. A Newton-Raphson method is implemented for Abaqus Standard simulations. The principle of virtual work is the fundamental equation upon which this method is based.

$$\int_V \delta \boldsymbol{\varepsilon}^T \boldsymbol{\sigma} dV = \int_S \delta \mathbf{u}^T \mathbf{t} dS \quad (3.36)$$

where V is a reference volume, S is the surface bounding the reference volume. $\boldsymbol{\sigma}$ is the stress tensor and \mathbf{t} is the surface traction. $\delta \boldsymbol{\varepsilon}$ is the virtual strain vector and $\delta \mathbf{u}$ is

the virtual displacement vector. Integration of equation 3.36 over a finite element mesh containing multiple elements with Volume (V_e) and Surface (S_e) is the sum of the integrands of each element. The virtual strain and displacement within each element are defined in equations (3.37 and 3.38)

$$\delta \boldsymbol{\varepsilon} = \mathbf{B}_e \delta \mathbf{u}_e \quad (3.37)$$

$$\delta \mathbf{u} = \mathbf{N}_e \delta \mathbf{u}_e \quad (3.38)$$

where, \mathbf{B}_e and \mathbf{N}_e are the element shape gradient and shape function matrices respectively. Therefore substituting equations 3.37 & 3.38 into equation 3.36 and integrating over a mesh of “e” number of elements give equation 3.39.

$$\sum_e \int_{V_e} \delta \mathbf{u}_e^T \mathbf{B}_e^T \boldsymbol{\sigma}(\mathbf{u}_e) dV = \sum_e \int_{S_e} \delta \mathbf{u}_e^T \mathbf{N}_e^T \mathbf{t} dS \quad (3.39)$$

\mathbf{u}_e is the elemental vector of nodal displacements. As equation 3.39 involves the summing of individual element quantities, the individual virtual components ($\delta \boldsymbol{\varepsilon}$ and $\delta \mathbf{u}$) become redundant and are replaced with global components giving equation 3.40.

$$\int_V \mathbf{B}^T \boldsymbol{\sigma}(\mathbf{u}) dV = \int_S \mathbf{N}^T \mathbf{t} dS \quad (3.40)$$

where, \mathbf{u} is the global nodal displacement vector for the mesh (containing “e” number of elements). The out of balance/residual forces vector (\mathbf{G}) can be written in terms of the global nodal displacement vector \mathbf{u} as shown in equation 3.41.

$$\mathbf{G}(\mathbf{u}) = \int_V \mathbf{B}^T \boldsymbol{\sigma}(\mathbf{u}) dV - \int_S \mathbf{N}^T \mathbf{t} dS = 0 \quad (3.41)$$

Implicit solving involves incremental methods, where loads/displacements are applied in time steps (Δt) up to a defined ultimate time (t_{ult}). Each increment of an analysis is solved and updated iteratively using the Newton Raphson Method from time t to time $t + \Delta t$ to solve for $\mathbf{u}^{t+\Delta t}$ until t_{ult} is reached. Defining equation 3.41 for the i^{th} iteration gives equation 3.42.

$$\delta \mathbf{u}_{i+1} = \mathbf{u}_{i+1}^{t+\Delta t} - \mathbf{u}_i^{t+\Delta t} = - \left(\frac{\partial \mathbf{G}(\mathbf{u}_i^{t+\Delta t})}{\partial \mathbf{u}} \right) \mathbf{G}(\mathbf{u}_i^{t+\Delta t}) \quad (3.42)$$

where, \mathbf{u}_{i+1} is the vector of nodal displacements for the i^{th} iteration at time $t + \Delta t$. The term on the right hand side is referred to as the Jacobian matrix or can be referred to as the global stiffness matrix (\mathbf{K}_G).

$$\mathbf{K}_G(\mathbf{u}_i^{t+\Delta t})\delta\mathbf{u}_{i+1} = -\mathbf{G}(\mathbf{u}_i^{t+\Delta t}) \quad (3.43)$$

Equation 3.43 must be solved, for each iteration, for the change in incremental displacements ($\delta\mathbf{u}_{i+1}$). In order to solve for $\delta\mathbf{u}_{i+1}$ the global stiffness matrix (\mathbf{K}_G) must be inverted. Therefore this leads to a significant computational expense compared to explicit solution method outlined in 3.4.2, but generates an accurate solution. The accuracy of the method also depends on the accurate calculation of $\mathbf{G}(\mathbf{u}_i^{t+\Delta t})$, which in turn depends on the accurate calculation of $\boldsymbol{\sigma}(\mathbf{u}_i^{t+\Delta t})$. The accuracy of the solution is also dictated by the convergence criterion where the updated value for \mathbf{G} must be less than a tolerance value. Complications can arise when using Abaqus Standard if:

- simulations involve a highly non linear stress-strain response
- simulating large deformation problems
- simulating damage and fracture of materials
- simulating contact and sliding between surfaces

One alternative available within Abaqus is the explicit solution method, described in the following section.

3.5.2 Explicit Modelling

Abaqus Explicit was developed for modelling dynamic problems, with large deformation of bodies. Acceleration and velocity at a particular time point are assumed constant for that time increment and are used to solve for next time point rather than the iterative method outlined in section 3.5.1 of this chapter. Abaqus explicit uses the central difference operator as outlined in equations 3.44 and 3.45.

$$\mathbf{u}^{i+1} = \mathbf{u}^i + \Delta t^{i+1}\dot{\mathbf{u}}^{i+\frac{1}{2}} \quad (3.44)$$

$$\dot{\mathbf{u}}^{i+\frac{1}{2}} = \dot{\mathbf{u}}^{i-\frac{1}{2}} + \frac{\Delta \mathbf{t}^{i+1} + \Delta \mathbf{t}^i}{2} \ddot{\mathbf{u}}^i \quad (3.45)$$

where, \mathbf{u} is the displacement vector and superscripts identifying the current time increment. In this case i refers to the increment number rather than the iteration number specified for implicit solving methods. As no iterations are involved in the Explicit solving method, no convergence checks are made. Therefore this method can be used to solve for simulations that failed to converge using the implicit solving method.

The use of an explicit solution means that each new time increment is calculated by assuming constant velocities $\dot{\mathbf{u}}$ and constant accelerations $\ddot{\mathbf{u}}$ across half time intervals $(i - \frac{1}{2})$. The accelerations are calculated at the start of an increment according to equation 3.46.

$$\ddot{\mathbf{u}}^i = \mathbf{M}^{-1}(\mathbf{F}^i - \mathbf{I}^i) \quad (3.46)$$

where, \mathbf{F}^i is the vector of externally applied forces and \mathbf{M} is the lumped mass matrix.

$$\mathbf{F}^i = \int_S \mathbf{N}^T \mathbf{t}^i dS + \int_V \mathbf{N}^T \mathbf{P}^i dV \quad (3.47)$$

where, \mathbf{P}^i is the vector of nodal forces and \mathbf{I}^i is the vector of internal element forces.

$$\mathbf{I}^i = \int_V \mathbf{B}^T \boldsymbol{\sigma}^i dV \quad (3.48)$$

$$\mathbf{M} = \int_V \rho \mathbf{N} dV \quad (3.49)$$

ρ denotes the current density of the material. All other quantities are defined in terms of the global expression of equation 3.40. The lumped mass matrix from equation 3.46 can be isolated to give $\mathbf{M}\ddot{\mathbf{u}} = (\mathbf{F} - \mathbf{I})$, which is comparable to the linear equation 3.43 of the implicit solving method. The lumped mass matrix (\mathbf{M}) is diagonalised making matrix inversion a significantly lower computational expense, compared to the inversion of the global stiffness matrix required by the implicit solving method.

Updating the incremental changes of the components of equation 3.46 requires small time increments to ensure an accurate solution. The stability limit determines the size of the time increment.

$$\Delta t < \frac{2}{\omega_{max}} \quad (3.50)$$

where, ω_{max} is the maximum element eigenvalue. The stability limit is enforced using equation 3.51.

$$\Delta t = \min\left(\frac{L^e}{c^d}\right) \quad (3.51)$$

where L^e is the characteristic element length and c^d is the dilatational wave speed.

$$c^d = \sqrt{\frac{\lambda + 2\mu}{\rho}} \quad (3.52)$$

where λ and μ are the Lamé constants and ρ is the material density. A quasi-static problem solved using the explicit solving method would require much smaller time increments than the implicit solving method. Each increment of an explicit simulation can be calculated at a low computational expense, however in some cases it is quite likely that >100,000 increments are required to solve. As the stability limit is based on the characteristic length of an element, it is important to maintain a regular element size within the mesh and ensure that excessively small elements do not reduce the increment size when using Abaqus Explicit.

The run time of an Abaqus Explicit simulation can be artificially reduced by speeding up the applied deformation or scaling the density of the materials of the model. Scaling of the density is the preferred method. Focussing on equations 3.51 and 3.52, when the density of the material is scaled by a factor, the incremental time magnitude is increased by the square root of that factor (eg. increasing the density by a factor of 4 would result in doubling the magnitude of Δt).

It has been shown that in order to prevent dynamic effects in the model the ratio between kinetic energy and internal energy in the model should be kept below 5% (Chung et al. (1998); Choi et al. (2002)).

3.6 References

- Abaqus, 2009. Abaqus Users Manual 6.9, Dassault Systemes Simulia Corp., Providence
- Abaqus, 2012. Abaqus Users Manual 6.12, Dassault Systemes Simulia Corp., Providence.
- Choi, H. H., Hwang, S. M., Kang, Y. H., Kim, J. and Kang, B. S., 2002. Comparison of Implicit and Explicit Finite-Element Methods for the Hydroforming Process of an Automobile Lower Arm. *The International Journal of Advanced Manufacturing Technology* 20, 407-413.
- Chung, W. J., Cho, J. W. and Belytschko, T., 1998. On the dynamic effects of explicit FEM in sheet metal forming analysis. *Engineering Computations* 15, 750-776.
- Drucker, D. and Prager, W., 1952. Soil Mechanics and Plastic Analysis or Limit Design. *Quarterly of applied mathematics* 10, 157.
- Hillerborg, A., Modeer, M. and Petersson, P. E., 1976. Analysis of crack formation and crack growth in concrete by means of fracture mechanics and finite elements. *Cement and concrete research* 6, 773-781.
- Melenk, J. M. and Babuška, I., 1996. The partition of unity finite element method: Basic theory and applications. *Computer Methods in Applied Mechanics and Engineering* 139, 289-314.
- Mercer, C., He, M. Y., Wang, R. and Evans, A. G., 2006. Mechanisms governing the inelastic deformation of cortical bone and application to trabecular bone. *Acta Biomaterialia* 2, 59-68.
- Song, J. H., Areias, P. and Belytschko, T., 2006. A method for dynamic crack and shear band propagation with phantom nodes. *International Journal for Numerical Methods in Engineering* 67, 868-893.
- Sukumar, N., Huang, Z. Y., Prévost, J. H. and Suo, Z., 2004. Partition of unity enrichment for bimaterial interface cracks. *International Journal for Numerical Methods in Engineering* 59, 1075-1102.

Chapter 4

Investigation of metallic and carbon fibre PEEK fracture fixation devices for three-part proximal humeral fractures

Abstract

An investigation of proximal humeral fracture fixation has been conducted. Four devices were selected for the study; a locking plate, intramedullary nail (IM Nail), K-wires and a Bilboquet device. A 3D model of a humerus was created using a process of thresholding based on the grayscale values of a CT scan of an intact humerus. An idealised three part fracture was created in addition to removing a standard volume from the humeral head as a representation of bone voids that occur as a result of the injury. All finite element simulations conducted represent 90° arm abduction. Simulations were conducted to investigate the effect of filling this bone void with calcium phosphate cement for each device. The effect of constructing devices from carbon fibre polyetheretherketone (CFPEEK) was investigated. Simulations of cement reinforced devices predict greater stability for each device. The average unreinforced fracture line opening (FLO) is reduced by 48.5 % for metallic devices, with a lesser effect on composite devices with FLO reduced by 23.6 %. Relative sliding (shear displacement) is also reduced between fracture fragments by an average of 58.34 %. CFPEEK device simulations predict reduced stresses at the device-bone interface.

4.1 Introduction

The shoulder joint allows multiplanar motion of the upper limb which is facilitated by a complex interaction of joint geometry, muscle forces and ligament restraints. Proximal humeral fractures can permanently disrupt this arrangement and lead to pain and loss of function, particularly when the joint (articular) surface is involved in the fracture pattern. Proximal humeral fractures are the third most frequent fracture after hip and wrist fractures (Kettler et al. (2006)). Cancellous bone depletes with age, thus the occurrence of proximal humerus fractures is highest particularly in the elderly. However, proximal humeral fractures are not limited to the elderly and can

also occur in younger individuals as a result of falling on an outstretched limb or as a result of a high energy impact. Displaced intra-articular fractures in physiologically fit patients are candidates for reconstructive surgery.

Several types of proximal humeral fracture fixation devices have been developed and implemented clinically. These include locking plates (Muckter et al. (2001); Kwon et al. (2002); Rose et al. (2007); Owsley and Gorczyca (2008)), intramedullary nails (Cuny et al. (2008); Koike et al. (2008)), the Bilboquet device (Doursounian et al. (2000); Doursounian et al. (2011)) and percutaneous fixation using K-wires (Jaberg et al. (1992); Resch et al. (1997)). Previous clinical studies for locking plates and intramedullary fixation have reported screw pullout and push out as primary modes of failure (Cuny et al. (2008); Owsley and Gorczyca (2008)). Previous experimental studies reported that K-wires had higher relative motion between fracture fragments than locking plates or an intramedullary rod (Koval et al. (1996); Kwon et al. (2002)). The Bilboquet device is not commonly used for proximal humeral fracture fixation compared to the other three methods of fixation; however it is proposed as an alternative to Hemiarthroplasty (Doursounian et al. (2000)).

Given that 70% of proximal humeral fractures occur in patients over 60 years of age (Kettler et al. (2006)), the injury can be complicated by osteoporosis. Bone voids, resulting from osteoporosis, mean poor results for proximal humerus fractures. In cases where the reconstruction of the fracture fragments is not possible, a void filling bone graft may be used (Ring et al. (2001)). Problems associated with bone grafts include limited availability and high cost. One option proposed to improve the performance of fracture fixation devices is to fill these bone voids with bone graft substitutes such as calcium phosphate cement (Faour et al. (2011)). Histological studies of calcium phosphate showed that it is osteoconductive (Frankenburg et al. (1998)). An experimental study by Kwon et al. (2002) reported lower relative motion between fracture fragments when bone voids were filled with cement (reinforced fixation). A clinical study of cement reinforced fixation found that it lowered the prevalence of pain at the fracture site compared to an unfilled bone void (unreinforced fixation) (Kwon et al. (2002); Bajammal et al. (2008)).

Previous studies have proposed carbon fibre (CF) reinforced composites as alternatives to metallic implants for several biomedical applications (Fujihara et al. (2004); Kurtz and Devine (2007); Kharazi et al. (2010)). CF reinforced composites can be tailored to have a significantly lower modulus than metallic devices close to that of cortical bone. A previous experimental study by Ponnappan et al. (2009) compared a polyetheretherketone (PEEK) rod system to titanium for spinal applications. It was reported that PEEK provided a more flexible stabilisation, as well as offering the advantage of reduced stress at the bone screw interface. An additional advantage of PEEK is the fact that it is radiolucent (Kurtz and Devine (2007)). This means fracture lines are easier to visualise with x-rays as there is no visible plate on the x-ray. PEEK devices are also MRI compatible as the artefact generated by metallic components makes interpretation of the MRI scan difficult (Ponnappan et al. (2009)). Some patients have developed cold weather intolerance as a result of metal devices (Kitsis et al. (2003)); the use of PEEK would eliminate this complication.

The objective of the present chapter is to computationally investigate the performance of four methods of fixation; locking plate, intramedullary rod, K-wires and the Bilboquet device. To date, no previous studies have compared the performance of these four devices in terms of micro motion between fracture fragments as well as stress distribution within the humeral head. The effect of reinforcing each device with calcium phosphate cement was also investigated. The effect of constructing devices from carbon fibre reinforced PEEK (CFPEEK) was investigated and compared to metallic devices.

4.2 Materials & Methods

4.2.1 Experimental

Experimental tests were conducted using synthetic humeri (4th generation humerus #3404, Sawbones, Malmö, Sweden). A three part fracture was recreated in a synthetic humerus and a fracture repair was implemented using a locking plate (Philos, AO, Davos, Switzerland), with screw configurations similar to those used in our finite element models (Figure 4.1(B)). The experimental set up is shown in Figure 4.2. Uniaxial strain gauges (CEA-06-240UZ-120, Micro-Measurements,

North Carolina, USA) were then applied to the shaft (S2) and humeral head (S1) of the repaired humerus and mechanical testing was performed. An intact (Figure 4.2(A)) synthetic humerus was also tested following identical strain gauge placement. Both humeri were orientated 63.33° to the vertical axis to represent 90° arm abduction (Poppen and Walker (1978)). The test was conducted using an Instron universal testing system (Model 3364, Instron, UK) with a 30 kN load cell. An LVDT was used to record the displacement of the crosshead of the Instron as shown in Figure 4.2(A). A data acquisition system (NI cDAQ-9172, National Instruments, Newbury, Berkshire, UK) was used to collect strain, load and displacement data at the same time points. A load of up to 534 N was applied at a linear rate of 1 mm/min. The test procedure was repeated five times ($n=5$) for both the intact and fracture repaired humerus. The strains recorded experimentally were compared to the predicted computational strains in the same regions of the humerus. Two sample t tests were conducted to establish the statistical significance of the results.

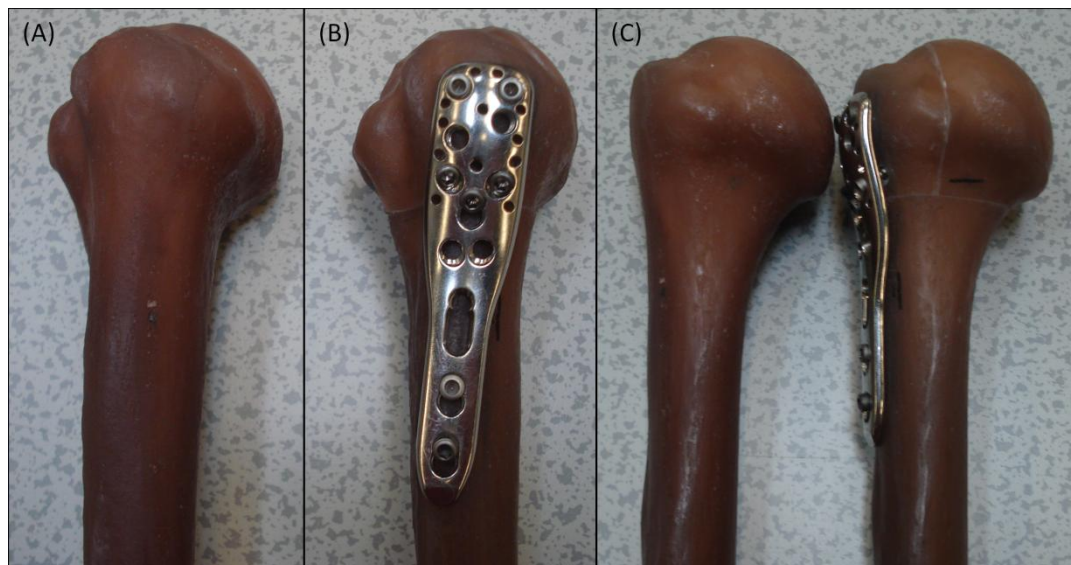


Figure 4.1 Experimental sample preparation; (A) intact humerus; (B) locking plate repaired three part fractured humerus; (C) side view of intact and plate repaired three part fracture highlighting fracture lines.

4.2.2 Computational:

A 3D geometry of an intact humerus was generated from the CT scan of a 78 year old Caucasian male. Using thresholding and 3D geometry generating software (v3.2 Simpleware Ltd. Exeter, UK) the grayscale values of the images were used to create cortical and cancellous bone volumes. The CT scans values were calibrated and

converted to Hounsfield units according to the equation $HU=1000 \times (CT - CT_w) / (CT_w - CT_a)$ where CT_w and CT_a are the CT values of water and air respectively (Rho et al. (1995)). A Hounsfield unit (HU) of zero represents water. A cortical bone volume was isolated by selecting pixels with a HU ranging from 500-900 (Lim Fat et al. (2012)). The cancellous bone volume was isolated as HU ranging from 80-499 within the humeral head (Yamada et al. (2007)). An idealised three part fracture was generated. The fracture fragments were created based upon the Mueller AO classification of proximal humeral fractures (Müller (1990)). The fracture fragments created are highlighted in Figure 4.3. The three fragments are the greater tuberosity (Figure 4.3A), articular and shaft fragments (Figure 4.3B). An ellipsoid shaped volume was removed from the humeral head to represent a bone void. The 37.7% volume of bone that remained was representative of the average percentage of bone tissue lost within the humeral head with age for patients that reported shoulder joint complications (Yamada et al. (2007)). Additionally, for simulations of cement reinforced fixation, this void was then filled with a homogeneous volume that was assigned the properties of commercially available calcium phosphate cement. 3D models of the four fracture fixation devices were generated and positioned in the assembled model according to anatomical location.

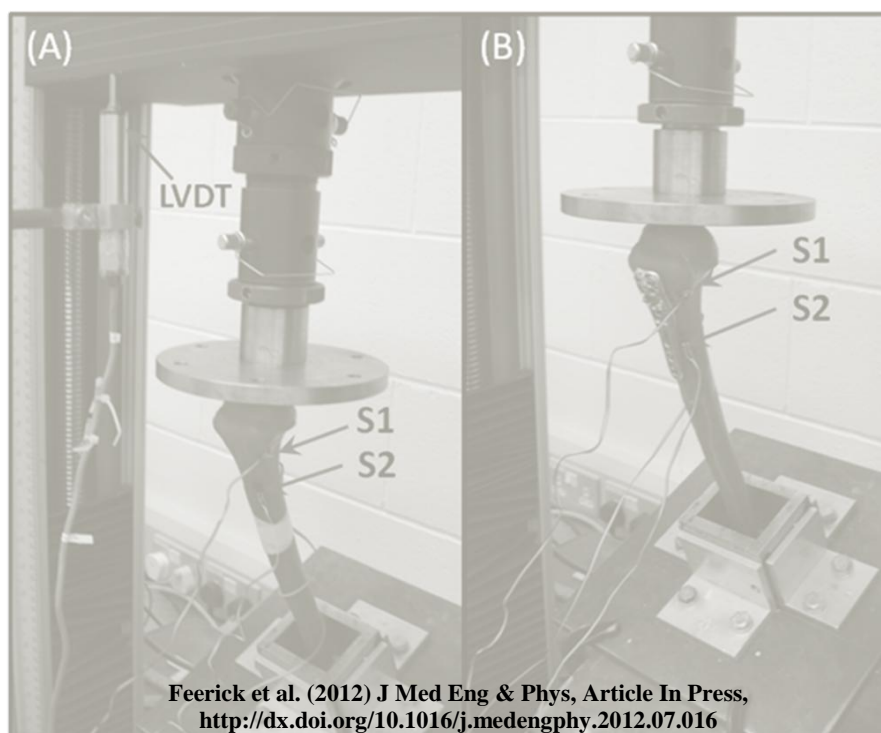
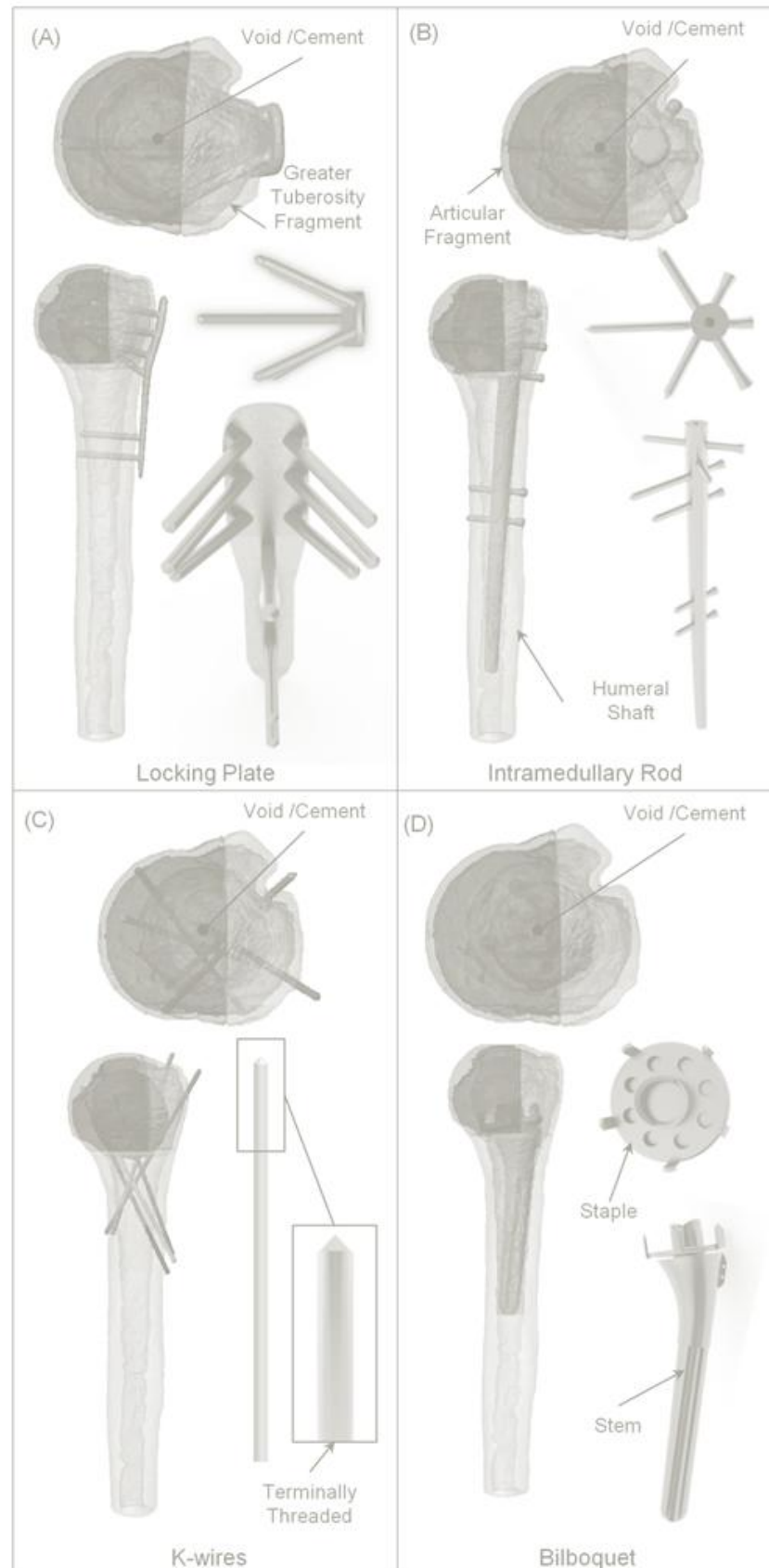


Figure 4.2 Experimental set up for 90° arm abduction loading; (A) intact humerus and (B) locking plate repaired three part fractured humerus.

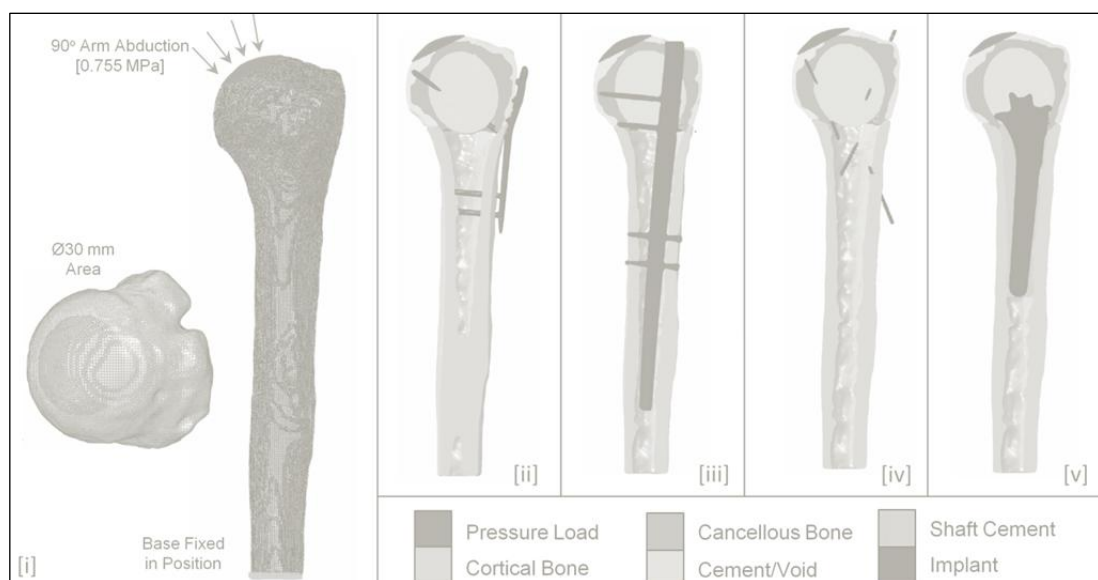
The four methods of fixation are shown in Figure 4.3. The locking plate is an external fixate with screws passing through the lateral cortex and anchored in the opposite cortical wall (Figure 4.3(A)). In this model, nine screws were modelled with two distal screws and seven screws anchored in the proximal humeral head. The void volume, highlighted in Figure 4.3(A-D), indicates the location of the cement for a reinforced fixation. The intramedullary nail is an internal fixate inserted into the intramedullary canal and locked both proximally (four screws) and distally (two screws) (Figure 4.3(B)). K-wires are stainless steel, terminally threaded wires that are pierced through the lateral cortex and anchored in the opposite cortical wall. A configuration using five K-wires was considered, based on the images reported by Jaberg et al. (1992). As shown in Figure 4.3(C), two K-wires were inserted through the greater tuberosity fragment and anchored in the humeral shaft cortex. The remaining three were inserted through the lateral distal shaft and inserted in the opposite articular fragment cortex. The Bilboquet device is an internal fixate consisting of two components: firstly, the stem, which is anchored with cement in the shaft of the humerus, and secondly, a spigot which is a pronged plate anchored in the humeral head (Figure 4.3(D)). A model of an intact humerus was also generated to provide a benchmark for comparison of stress fields generated by each of the fixation devices.



Feerick et al.
(2012) J Med
Eng & Phys,
Article In
Press,
<http://dx.doi.org/10.1016/j.medengphy.2012.07.016>

Figure 4.3: 3D computational models four methods of fixation. The three fracture fragments are highlighted in different colours; the greater tuberosity (blue), the articular fragment (purple) and the shaft (green). (A) Locking plate fixation, (B) IM rod fixation, (C) 5 K-wire fixation, (D) Bilboquet fixation.

The mesh generated for each fixation method contained, on average, 750,000 elements (20% hex C3D8 elements and 80% tet C3D4 elements). Due to the complex curvature of the humerus, the mesh consists of both tet and hex elements. All computational simulations were conducted using the finite element solver software Abaqus 6.9 standard (Simulia, Providence, RI, USA). Figure 4.4 illustrates the boundary conditions placed on the model for each of the simulations. The base of the shaft of the humerus was fixed in position. The load applied to the humerus model was selected based upon the experimental data reported by Poppen and Walker (1978), which stated that a compressive peak load of 80% body weight exerted at the humeral head occurs at 90° abduction. A previous 3D computational study of a shoulder joint also reported peak stresses occurred at 90° arm abduction Clavert et al. (2006). A pressure load of 0.755 MPa was applied over a circular area of Ø30 mm (representing 534 N), at an angle of 63.33° relative to the central axis of the humeral shaft to simulate 90° arm abduction. Five loading-unloading cycles with a linear waveform were performed to analyse cumulative micro motion at the fracture fragment contact surfaces. Linear elastic material behaviour is assumed in the current chapter without consideration of plasticity or damage. The material properties assigned to the models are summarised in Table 4.1.



Feerick et al. (2012) *J Med Eng & Phys*, Article In Press,
<http://dx.doi.org/10.1016/j.medengphy.2012.07.016>

Figure 4.4 [i] Boundary conditions applied to all models created including intact simulation, [ii] Section view of locking plate fixation, [iii] Section view of IM nail fixation, [iv] Section view of K-wire fixation, [v] Section view of Bilboquet fixation.

Table 4.1 Material Properties

	Modulus (GPa)	Poisson's Ratio
Cortical Bone	12	0.3
Cancellous Bone	0.1	0.3
Cement	1.52	0.3
Titanium (Locking Plate, Bilboquet)	110	0.3
Stainless Steel (Intramedullary Nail, K-wires)	193	0.3
Short Fibre CFPEEK	18	0.3

Contact interactions were included between the humeral shaft and the greater tuberosity fragment, between the humeral shaft and the articular fragment, and between the greater tuberosity and the articular fragments. The contact interactions were defined using surface to surface finite sliding with a coefficient of friction of 0.3 (Viceconti et al. (2004)). Tied constraints were applied between the cement and surrounding bone / device under the assumption that cement attains full adhesion with the surrounding components. Tied constraints were also applied between threaded areas of each device and surrounding bone.

Simulations were conducted to evaluate the performance of locking plate and IM nail devices constructed from short carbon fibre reinforced PEEK (CFPEEK) with a modulus of 18 GPa. CFPEEK is significantly more compliant than titanium (110 GPa) and stainless steel (193 GPa). Simulations were also conducted for reinforced fixations with a cement modulus ranging from 0.1 GPa to 1.5 GPa.

Each simulation was examined and compared, in terms of micro motion, between the fracture fragments as well as stress distribution within the humeral head. Pressure and shear stresses are considered in order to provide a complete description of the stress state in the bone and implant. Regions in which the yield stress of bone is exceeded are identified. In particular, high pressures at implant tips and high shear

stresses along implant bone interfaces indicate possible implant pullout or push out for each device

4.3 Results

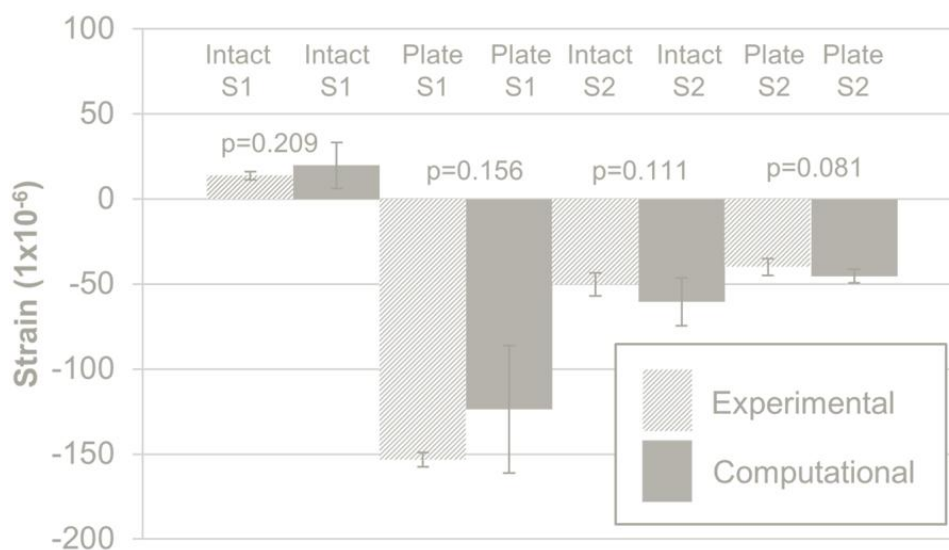
4.3.1 Experimental:

The peak experimental strains were compared to the computed axial strain components in the corresponding strain gauge direction in the finite element simulations (Figure 4.5). Due to the high level of mesh refinement, several elements coincided with the strain gauge location. Therefore, a range of strains are presented for the computational results of Figure 4.5. It was noted that in the region of strain gage S1, the strain changed from tension, for the intact case, to compression, for the locking plate case. The compressive strain magnitude for the locking plate fixation was six times higher than the tensile strain magnitude of the intact humerus. It should be noted that there was a large range for the computational simulations of locking plate fixation at the location of S1, as a high strain gradient was computed in this region. A reduction in compressive strain occurred at location S2 for the locking plate repaired humerus, compared to an intact humerus. As shown in the chart of Figure 4.5, the same trends in strain were observed both computationally and experimentally. No statistical difference was observed between the experimental and computational results.

4.3.2 Computational:

The stability of each fixation method was examined by computing the maximum magnitude of fracture line opening (FLO) between fracture fragments. In all cases the cement reinforced simulations had significantly lower FLO between fracture fragments than unreinforced simulations. The deformed shape of a K-wire fixation at the mid-cycle peak load is shown for the unreinforced and reinforced simulations in Figure 4.6A and 4.6B respectively. The two key areas of FLO are highlighted for both reinforced and unreinforced K-wire fixation. As a result of the glenohumeral loading, we see that the articular fragment was compressed into the greater tuberosity and subject to a rotation. This resulted in FLO at the medial side of the articular fragment and humeral shaft surfaces. At the same time, the greater

tuberosity fragment was subject to a rotation outwards in the lateral direction. This lead to opening of fracture lines between the greater tuberosity and humeral shaft surfaces. A similar pattern of deformation was observed for all four devices. As illustrated in Figure 4.6C, cement reinforcement resulted in a significant reduction in FLO (<19 microns) for all four devices. A cement reinforced Bilboquet simulation computed the most significant reduction (67%) compared to the unreinforced equivalent.

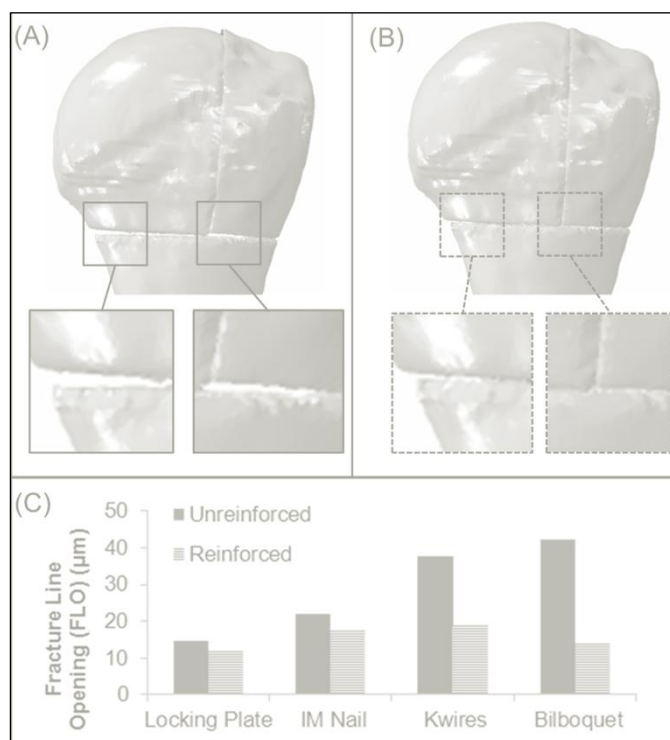


Feerick et al. (2012) J Med Eng & Phys, Article In Press,
<http://dx.doi.org/10.1016/j.medengphy.2012.07.016>

Figure 4.5 Graph of average peak experimental strains (micro strains) recorded for five tests (n=5) and standard deviations compared to the average strains predicted computationally at peak load in the same regions for intact and plate repaired humeri.

In addition to FLO, relative sliding (shear displacement) between fracture fragments was computed for five cycles of loading and unloading. The average shear displacement between the fracture fragments is reported for both reinforced and unreinforced devices in Figure 4.7. During five cycles of loading and unloading there was a cumulative increase in shear displacement between the fracture fragments. In all cases, reinforced simulations predicted lower shear displacement between fracture fragments compared to unreinforced devices. K-wire simulations predicted the highest shear displacement compared with other reinforced devices. The same trend was predicted when unreinforced K-wires were compared to other unreinforced devices. An unreinforced IM nail and Bilboquet predicted similar shear displacement magnitudes. A reinforced locking plate and IM nail computed shear displacements

close in magnitude. A reinforced Bilboquet simulation predicted the lowest magnitude of shear displacement.



Feerick et al. (2012) *J Med Eng & Phys*, Article In Press,
<http://dx.doi.org/10.1016/j.medengphy.2012.07.016>

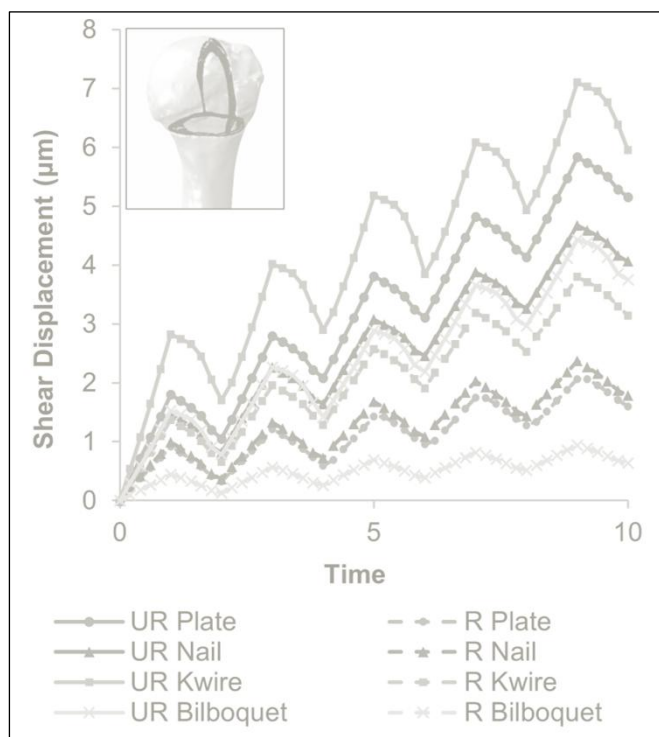
Figure 4.6 (A) Failure mode for unreinforced K-wire fixation (deformation scale factor: 50), (B) Failure mode for reinforced K-wire fixation (deformation scale factor: 50), (C) Bar chart of maximum fracture line opening (FLO) between fracture fragments.

Figure 4.8 summarises the shear stress (Tresca) distribution within the cortical bone of the humerus for each method of fixation compared to an intact model. A section view of the cortical bone for each method of fixation simulated is presented in Figure 4.8(A-D). Shear stress distribution computed for an intact cortical humerus is also presented for comparison (Figure 4.8(E)). The key points to note are as follows:

- In all cases, cement reinforcement resulted in a reduction in the average shear stress in both the articular and greater tuberosity fragments.
- For all devices, shear stresses in the lateral cortex of the greater tuberosity and humeral shaft were lower than those computed for the intact humerus. Reductions in shear stress were more pronounced in cement reinforced fixations.
- Unreinforced locking plate, K-wires and Bilboquet fixation resulted in shear stresses in the articular fragment that were higher than those computed for the

intact case. Unreinforced locking plate and IM nail fixation resulted in lower shear stresses within the greater tuberosity than the intact case. In contrast, unreinforced K-wires and Bilboquet fixation resulted in higher shear stresses than the intact case in the greater tuberosity.

- Shear stresses in the articular and greater tuberosity fragments computed for a reinforced Bilboquet fixation, were significantly lower than those predicted for the intact case.

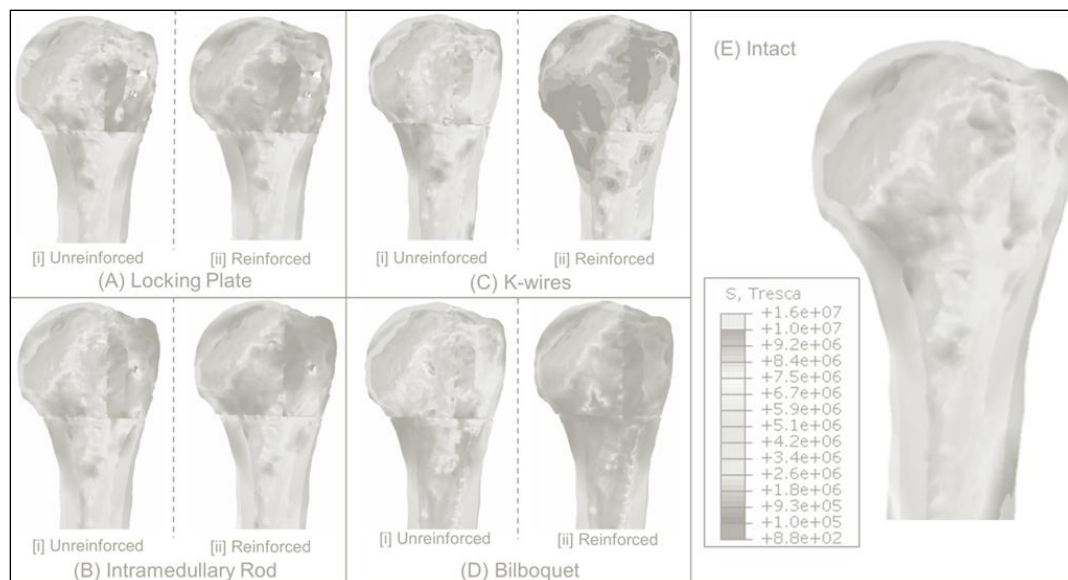


Feerick et al. (2012) *J Med Eng & Phys*, Article In Press,
<http://dx.doi.org/10.1016/j.medengphy.2012.07.016>

Figure 4.7 Average shear displacement between fracture fragments for unreinforced (UR) and reinforced (R) fracture fixation during five cycles of loading and unloading.

Figure 4.9 summarises the pressure distribution within the cortical bone of the humerus for each method of fixation compared to an intact humerus. A section view of the cortical bone, for each method of fixation simulated, is presented in Figure 4.9(A-D). An intact cortical bone section view of pressure distribution is also presented in Figure 4.9(E). The computed pressures followed the same trend as the computed shear stresses, with the highest pressures predicted in the regions surrounding the device anchors/screws. An unreinforced K-wire and IM nail achieved the closest pressure distribution to that computed for the intact case. A reinforced Bilboquet device resulted in significantly lower pressure distribution

within the humeral head compared to all other devices, with the average pressure distribution within the articular fragment being three times lower than the intact case. The average pressure distribution within the greater tuberosity was five times lower than the intact case.



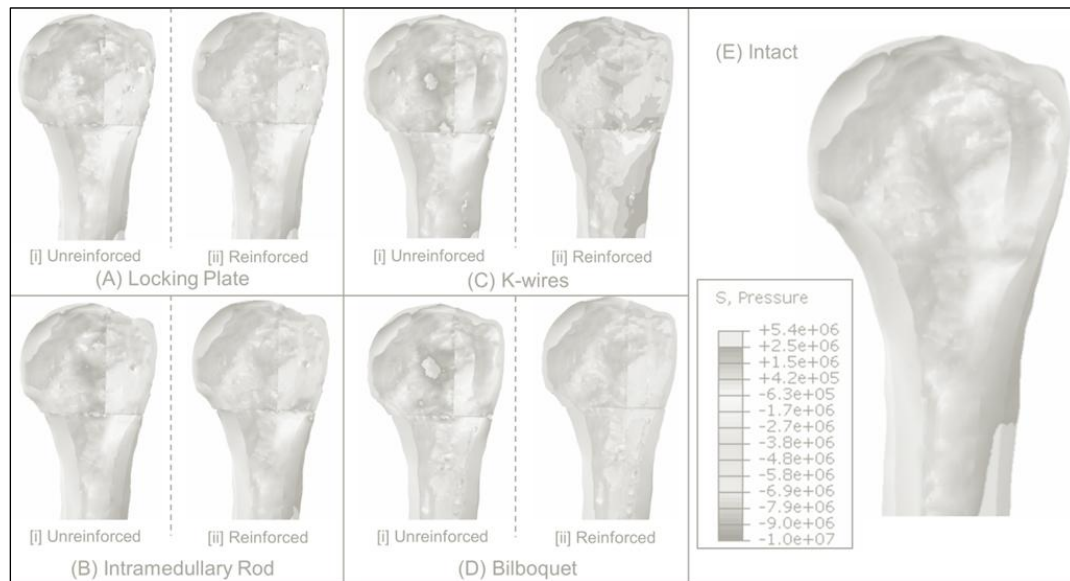
Feerick et al. (2012) *J Med Eng & Phys*, Article In Press,
<http://dx.doi.org/10.1016/j.medengphy.2012.07.016>

Figure 4.8 Section view of Tresca shear stress distribution within the humerus cortical bone, (A) Locking plate fixation [i] Unreinforced, [ii] Reinforced, (B) IM nail fixation [i]Unreinforced, [ii]Reinforced, (C) K-wires fixation [i] Unreinforced, [ii] Reinforced, (D) Bilboquet fixation [i] Unreinforced, [ii] Reinforced, (E) Shear stress distribution within an intact humerus subject to 90° arm abduction.

Additional simulations, over a range of loading orientations for an unreinforced locking plate and IM nail, are shown in Figures 4.10 and 4.11 respectively. The computed shear stress in the humeral shaft cortical bone decreased with increasing arm abduction (angle of loading), as shown in Figure 4.10, with a minimum reached at 90° and an increase observed at 120°. In contrast with this, the shear stress within the humeral head increased with increasing arm abduction (angle of loading), reaching a maximum at 90° and reducing again at 120°.

Shear stress distribution computed for an IM nail is presented in Figure 4.11. Due to the fact that the IM nail is an internal fixate, the lateral side of the humerus was shielded from the fluctuating shear stress observed for the locking plate repaired humerus, for all loading orientations. Similar to the locking plate (Figure 4.10) the computed shear stress within the cortical bone of the humeral head increased with

increasing angle of abduction, as shown in Figure 4.11. The highest shear stress occurred at 90° abduction, with a reduction observed for 120°. However, in contrast to the locking plate fixation, no significant changes in shaft stresses were computed across the range of loading orientations for the IM nail. The results included in Figure 4.10 and 4.11 highlight that 90° abduction was the critical loading orientation at which maximum stresses occurred in the regions surrounding screw tips and within the humeral head.

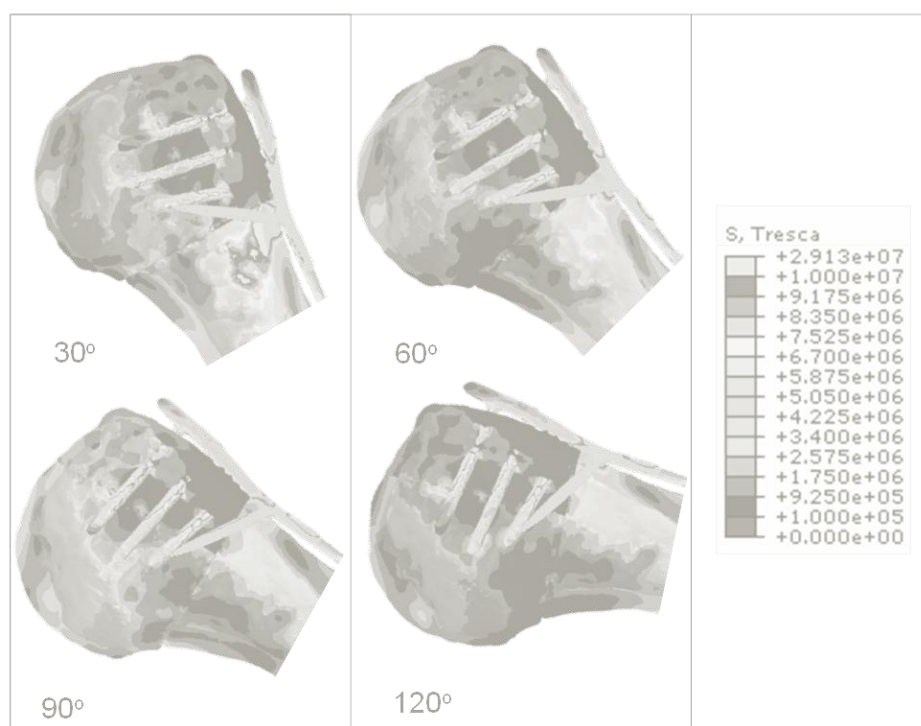


Feerick et al. (2012) *J Med Eng & Phys*, Article In Press,
<http://dx.doi.org/10.1016/j.medengphy.2012.07.016>

Figure 4.9 Section view of pressure distribution within the humerus cortical bone, (A) Locking plate fixation [i] Unreinforced, [ii] Reinforced, (B) IM nail fixation [i] Unreinforced, [ii] Reinforced, (C) K-wires fixation [i] Unreinforced, [ii] Reinforced, (D) Bilboquet fixation [i] Unreinforced, [ii] Reinforced, (E) Pressure distribution within an intact humerus subject to 90° arm abduction

Highly localised maximum values of pressures and shear stresses occurred in the cortical bone directly surrounding the screws of the locking plate and IM nail. Figure 4.12 highlights such stress concentrations for a metallic unreinforced locking plate and intramedullary nail fixation (Figure 4.12(A-B)). Pressure concentrations also occurred in the regions of cortical bone at the tips of the screws (pressure concentrations not shown in Figure 4.12). Unreinforced fixations had higher maximum stresses than reinforced. Unreinforced locking plates computed the highest maximum stresses. A maximum shear stress of 113 MPa was computed in the cortical bone adjacent to the screw tips. This exceeded reported values of ultimate tensile strength (UTS) (95.1 MPa Dickenson et al. (1981)) for osteoporotic bone. Given the extremely high cortical bone stress concentrations that resulted from

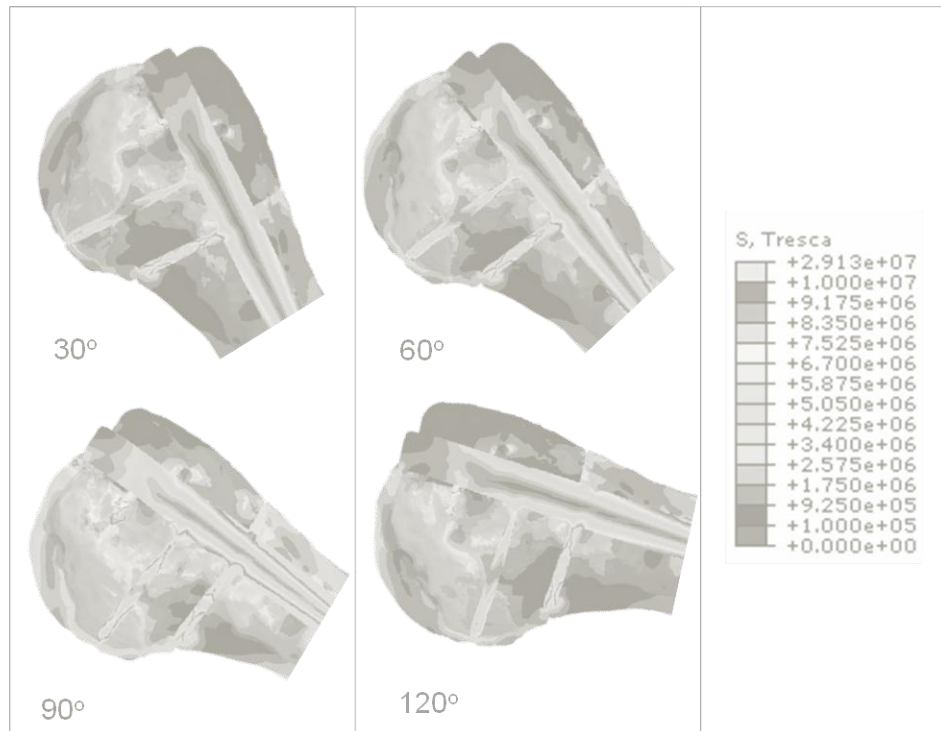
metallic fixation devices, simulations using CFPEEK devices were conducted for a locking plate and IM nail (Figure 4.12(C-D)). The maximum stresses within the cortical bone were significantly reduced when the fixation device was constructed from CFPEEK, compared to a metallic implant as shown by the bar chart in Figure 4.12(E). The maximum shear stress was significantly reduced from 112 MPa to 45 MPa when a CFPEEK plate was used instead of a metallic plate for unreinforced fixation. A similar trend was observed for an IM Nail. The corresponding reductions were less significant when devices were cement reinforced.



Feerick et al. (2012) *J Med Eng & Phys*, Article In Press,
<http://dx.doi.org/10.1016/j.medengphy.2012.07.016>

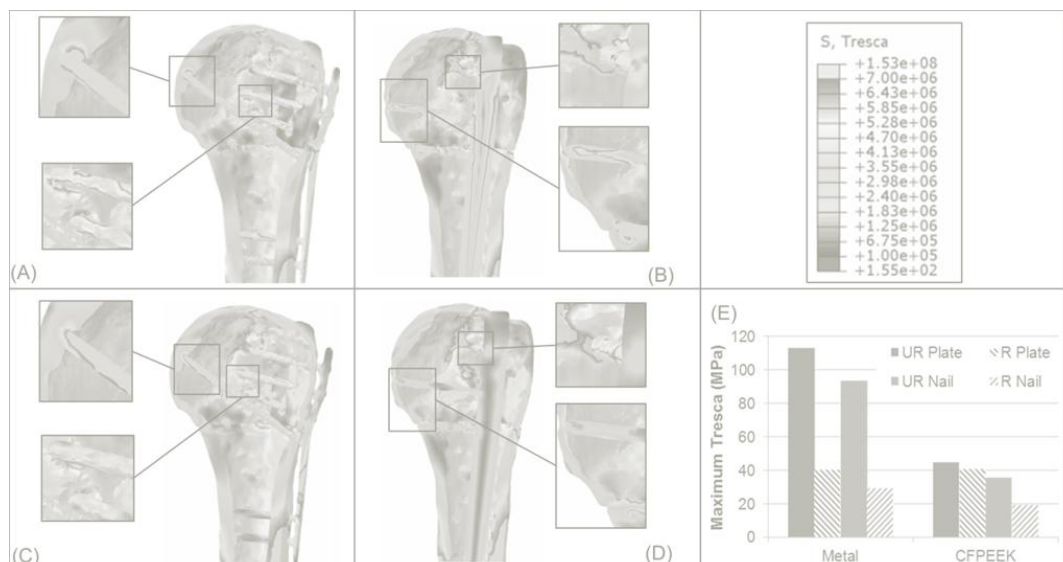
Figure 4.10 Computed shear stress (Tresca) (Pa) for unreinforced locking plate for four stages of abduction (30°, 60°, 90° and 120°).

Clearly the device material and cement reinforcement had a significant effect on cortical bone stress. The effect of cement modulus on cortical bone stress is shown in Figure 4.13(A-C) for a CFPEEK locking plate fixation. Cement moduli of 1.5GPa, 0.5GPa and 0.1GPa were considered and bone stresses were compared to the intact case (Figure 4.13(D)). With decreasing modulus of bone cement the average stress within the greater tuberosity and articular fragments increased, becoming a closer replication of the shear stress distribution of the intact case in this region.



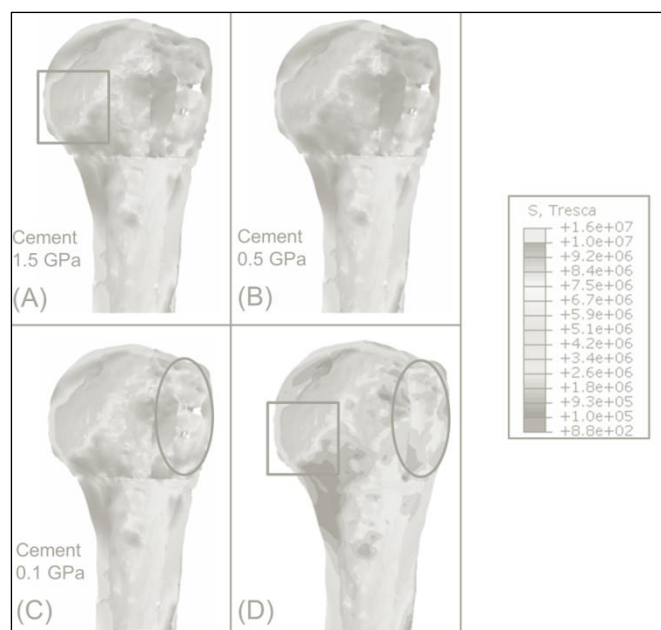
Feerick et al. (2012) *J Med Eng & Phys*, Article In Press,
<http://dx.doi.org/10.1016/j.medengphy.2012.07.016>

Figure 4.11 Computed shear stress (Tresca) (Pa) for unreinforced IM nail for four stages of abduction (30°, 60°, 90° and 120°).



Feerick et al. (2012) *J Med Eng & Phys*, Article In Press,
<http://dx.doi.org/10.1016/j.medengphy.2012.07.016>

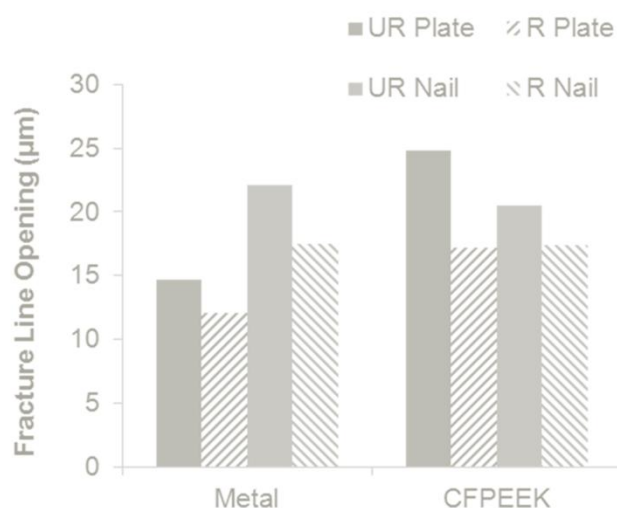
Figure 4.12 Shear stress section view of implant and cortical bone (A) unreinforced titanium locking plate, (B) unreinforced stainless steel IM nail, (C) unreinforced CFPEEK plate, (D) unreinforced CFPEEK IM nail, (E) Bar chart of maximum shear stresses for unreinforced (UR) and reinforced (R) metallic and CFPEEK devices.



Feerick et al. (2012) *J Med Eng & Phys*, Article In Press,
<http://dx.doi.org/10.1016/j.medengphy.2012.07.016>

Figure 4.13 Section view of shear stress distribution within the humerus cortical bone comparing intact humerus shear stress distribution to reinforced CFPEEK locking plate with cements of varying moduli; (A) Cement modulus (1.5 GPa), (B) Cement modulus (0.5 GPa), (C) Cement modulus (0.1 GPa), (D) Intact.

In addition to CFPEEK offering reduced peak stresses, it was necessary that reasonable stability was provided. Thus fracture line opening (FLO) (Figure 4.14(A)) between fracture fragments was compared to corresponding metallic devices. In the case of an unreinforced locking plate fixation, a CFPEEK device computed FLO of 25 μm , compared to a FLO of 15 μm for a metallic locking plate. A higher FLO was also computed for the CFPEEK device for a reinforced fixation. In the case of IM nail fixation, very similar levels of FLO were computed for CFPEEK and metallic devices. Overall, simulations suggested that the FLO for CFPEEK devices was of a similar order to that provided by metallic devices.



Feerick et al. (2012) *J Med Eng & Phys*, Article In Press,
<http://dx.doi.org/10.1016/j.medengphy.2012.07.016>

Figure 4.14 Comparison of metallic locking plate and IM nail versus CFPEEK for fracture line opening (FLO) between fracture fragments.

4.4 Discussion

This chapter provides, for the first time, a computational assessment of four fracture fixation techniques for proximal humerus fractures, with a specific focus on cortical bone stress, fracture fragment displacement, cement reinforcement and device material properties at 90° arm abduction. For all devices, it was found that cement reinforcement increases the stability, reducing the FLO as well as shear displacement between the fracture fragments. Unreinforced locking plates and IM nail fixation result in extremely high cortical bone stress concentration in the region surrounding screw tips. Predicted stresses exceed reported values of ultimate strength of osteoporotic cortical bone (95.1 MPa Dickenson et al. (1981)), indicating a high potential for screw pullout/pushout. This is a commonly reported clinical failure mode for these devices (Owsley and Gorczyca (2008)). We demonstrate that devices manufactured from short fibre CFPEEK will significantly reduce cortical bone stresses in the region of the screw tips, and may provide lower instances of device failure by screw pullout/pushout. We also demonstrate that CFPEEK devices provide a similar level of fixation stability to metallic implants in terms of FLO between fracture fragments.

One commonly reported issue with proximal humeral fracture fixation is that fixation methods are too stiff (Lill et al. (2003)), leading to block pullout of screws, or screw penetration into the glenoid (Owsley and Gorczyca (2008); Clavert et al. (2010); Dheerendra et al. (2011)). In the present chapter, localised maximum stresses computed for unreinforced models, at the implant anchor-screw interface with cortical bone for metallic devices, are an indicator of potential screw pullout/push out. These maximum stresses fall within the range for yield and potential fatigue failure for cortical bone, particularly if these devices were used to repair osteoporotic bone with a yield stress of 75.8 MPa and ultimate strength of 95.1 MPa (Dickenson et al. (1981)). The occurrence of these maximum stresses in the region of the screw tips motivated the study of cortical bone failure mechanisms during screw pullout in Chapter 5. Resch (2011) proposed the use of semi rigid constructs such as K-wires to reduce maximum stresses within the humeral head. This is supported by the results of the present chapter, which suggests that K-wire fixation results in lower stress concentrations in the cortical bone than a locking plate or IM nail fixation. However, the stability predicted for K-wire fixation is lower than these devices which is supported by clinical studies that reported issues with K-wire migration (Bogner et al. (2008); Brunner et al. (2010)). In the present chapter we demonstrate that carbon fibre reinforced PEEK (CFPEEK) locking plates and IM nails provide a less stiff fixation than metallic devices, resulting in lower stress concentrations at anchor sites. This suggests that CFPEEK devices will lower the risk of device failure due to screw pullout/pushout. An experimental and computational study by Bougherara et al. (2011) compared a composite hip stem to commercially available metallic equivalents. This study highlighted the reduced stress in the composite implant, suggesting it would better replicate the stress distribution within an intact femur. While the current chapter provides motivation for the development of CFPEEK devices, the application of composite materials for proximal humeral fracture fixation warrants further investigation in terms of design optimisation and fatigue performance (Sobieraj et al. (2009); Sobieraj et al. (2010)). In addition to significantly lowering maximum cortical bone stresses, CFPEEK devices do not compromise the stability of the fracture fragments compared to metallic equivalents. A recent study by Yáñez et al. (2010) proposed a new system for reducing the incidence of screw loosening and screw pullout using a PEEK screw locking element for metal fracture plates.

Stability is an important factor when selecting a method of fixation for proximal humeral fracture fixation. Focussing on metallic devices, a reinforced Bilboquet device has the lowest level of shear displacement, followed by a reinforced locking plate, followed by a reinforced intramedullary nail. An unreinforced K-wire fixation predicts the highest level of shear displacement between fracture fragments. However, reinforced K-wires predicted shear displacement lower than that of an unreinforced locking plate and intramedullary rod, as well as predicting the lowest peak stresses at the cortical bone-implant interface. This suggests that reinforced K-wires may be a viable option for proximal humeral fracture fixation. All devices exhibited a cumulative increase in shear displacement. In the case of unreinforced K-wire fixation, the large cyclic increment of shear displacement could prove problematic over a large numbers of loading cycles, leading to a loss of fracture surface overlap. Additionally, the computed FLO is highest for the unreinforced K-wires and the Bilboquet device, with cement reinforcement offering a significant reduction for both. The prediction of normal (FLO) and tangential (shear displacement) components of relative motion of fracture fragments, in the current chapter, provides an insight into the mechanisms of inter-fragmentary micro-motion. Previous experimental studies have reported relative motion between fracture fragments (Kwon et al. (2002); Rose et al. (2010)), without specifying the normal and tangential components.

The computed results suggest that cement reinforcement is advantageous for all four methods of fixation, predicting significant increases in fracture fixation stability. All reinforced simulations predicted lower FLO than an unreinforced simulation. This finding is supported by previous experimental studies (Kwon et al. (2002); Mathison et al. (2010)). Furthermore, a recent clinical study by Neviasser et al. (2011) reported lower complications with reinforced locking plates in regard to screw penetration/cutout or loss of reduction. While reinforcement was provided by an allograft strut in this clinical study, the simulations performed in the current chapter suggest that cement reinforcement would provide similar improvements. Due to the fact that K-wires and intramedullary rod fixations require small incisions for device insertion, it could be suggested that cement reinforcement would not be viable surgically, as commercially available cements require significantly larger openings for insertion. However, the development of percutaneous injectable calcium

phosphate bone cements (Low et al. (2010)) may facilitate the implementation of cement reinforced K-wires and intramedullary rod. In addition to lower modulus materials for each device, a parameter study of cement modulus provides motivation for developing lower modulus bone cements in order to better replicate the intact case in terms of cortical bone stress, while increasing stability.

The present chapter contains a number of limitations. Tied constraints are applied to contact surfaces between cement and surrounding bone or implants. The assumption that complete adhesion exists between these components may not be fully representative of the in vivo environment and merits further study. Each device is examined for one configuration of fixation, based on those selected by previous publications (Kwon et al. (2002); Koike et al. (2008)). The locking plate, IM nail and K-wires can have several configurations. The angles of the screws of a locking plate and intramedullary rod can be altered. Additionally, a large range of insertion and anchor points can be implemented for various numbers of K-wires. While the optimal for each has yet to be identified, the computational models developed in the current chapter can provide a platform for future device optimisation. Linear elastic material behaviour is assumed in the current chapter without consideration of plasticity or damage (Mullins et al. (2009); Kelly and McGarry (2012)). Simulations suggest that high stress concentrations in the regions of screw tips will lead to bone plasticity, damage and ultimately screw pullout. Given the high level of geometric detail incorporated into our models of the humerus and fixation devices, very large numbers of elements were used (>700,000), with full contact being implemented at fracture surfaces. It is important to note that five loading cycles required 24 hour run time, using 64 cores on a high performance workstation. Therefore it was not feasible to simulate large numbers of loading cycles for the devices considered. The loads applied to the humerus are simplified to a glenohumeral force at 90° arm abduction, with no muscle simulation included. The present chapter focuses primarily on 90° loading. Simulations over a range of loading orientations reveal that the highest stresses occur at this orientation. However, it is important to note that the load orientation does influence the distribution of stress in the bone and the device. It was assumed that the material properties of a composite plate could be directly applied to the same geometry of the metallic plate; this was justified by the fact that short carbon fibre reinforced PEEK can be injection moulded.

In conclusion, this chapter provides, for the first time, a computational assessment of four fracture fixation techniques for proximal humerus fractures. This chapter is also the first computational study to report cyclic loading and micro motion between contact surfaces of fracture fragments for proximal humeral fracture fixation. A previous study by Maldonado et al. (2003) conducted finite element simulations on a plate fixation of a two part humeral fracture by representing fracture lines as areas of low stiffness, providing limited insight into relative fracture fragment motion. Previous studies have evaluated the performance of composite materials as alternatives to metal for fracture plates (Fujihara et al. (2004); Kharazi et al. (2010); Kim et al. (2010)). The present study provides the first computational assessment of CFPEEK for proximal humeral fracture fixation. The findings presented offer further motivation for development of this material for fracture fixation devices as an alternative to current metallic equivalents.

4.5 References

- Bajammal, S. S., Zlowodzki, M., Lelwica, A., Tornetta, P., Einhorn, T. A. and Buckley, R., 2008. The use of calcium phosphate bone cement in fracture treatment. *J Bone Joint Surg Am* 90, 1186-1196.
- Bogner, R., Hubner, C., Matis, N., Auffarth, A., Lederer, S. and Resch, H., 2008. Minimally-invasive treatment of three- and four-part fractures of the proximal humerus in elderly patients. *J Bone Joint Surg Br* 90, 1602-1607.
- Bougherara, H., Zdero, R., Dubov, A., Shah, S., Khurshid, S. and Schemitsch, E. H., 2011. A preliminary biomechanical study of a novel carbon-fibre hip implant versus standard metallic hip implants. *Medical Engineering & Physics* 33, 121-128.
- Brunner, A., Weller, K., Thormann, S., Jöckel, J. A. and Babst, R., 2010. Closed Reduction and Minimally Invasive Percutaneous Fixation of Proximal Humerus Fractures Using the Humerusblock. *J Orthop Trauma* 24, 407-13.
- Clavert, P., Adam, P., Bevort, A., Bonnomet, F. and Kempf, J. F., 2010. Pitfalls and complications with locking plate for proximal humerus fracture. *J Shoulder Elbow Surg* 19, 489-494.
- Clavert, P., Zerah, M., Krier, J., Mille, P., Kempf, J. and Kahn, J., 2006. Finite element analysis of the strain distribution in the humeral head tubercles during abduction: comparison of young and osteoporotic bone. *Surg Radiol Anat* 28, 581-587.
- Cuny, C., Scarlat, M. M., Irrazi, M., Beau, P., Wenger, V., Ionescu, N. and Berrichi, A., 2008. The Telegraph nail for proximal humeral fractures: A prospective four-year study. *J Shoulder Elbow Surg* 17, 539-545.
- Dheerendra, S. K., Khan, W. S., Barber, J., Goddard, N. J. and Ahrens, P. M., 2011. Outcomes of locking plates in proximal humeral fractures: a systematic review. *Shoulder & Elbow* 3, 74-84.
- Dickenson, R. P., Hutton, W. C. and Stott, J. R., 1981. The mechanical properties of bone in osteoporosis. *Journal of Bone and Joint Surgery-British Volume* 63, 233-38.
- Doursounian, L., Grimberg, J., Cazeau, C., Jos, E. and Touzard, R., 2000. A new internal fixation technique for fractures of the proximal humerus-the Bilboquet device: A report on 26 cases. *J Shoulder Elbow Surg* 9, 279-288.
- Doursounian, L., Kilinc, A., Cherrier, B. and Nourissat, G., 2011. Complex proximal humeral fractures: A prospective study of 22 cases treated using the "Bilboquet" device. *Orthop. Traumatol. Surg. Res.* 97, 58-66.
- Faour, O., Dimitriou, R., Cousins, C. A. and Giannoudis, P. V., 2011. The use of bone graft substitutes in large cancellous voids: Any specific needs? *Injury* 42, Supplement 2, S87-S90.
- Frankenburg, E. P., Goldstein, S. A., Bauer, T. W., Harris, S. A. and Poser, R. D., 1998. Biomechanical and histological evaluation of a calcium phosphate cement. *J Bone Joint Surg Am* 80, 1112-1124.
- Fujihara, K., Huang, Z. M., Ramakrishna, S., Satknanantham, K. and Hamada, H., 2004. Feasibility of knitted carbon/PEEK composites for orthopedic bone plates. *Biomaterials* 25, 3877-3885.
- Jaberg, H., Warner, J. J. and Jakob, R. P., 1992. Percutaneous stabilization of unstable fractures of the humerus. *J Bone Joint Surg Am* 74, 508-15.
- Kelly, N. and McGarry, J. P., 2012. Experimental and numerical characterisation of the elasto-plastic properties of bovine trabecular bone and a trabecular bone

- analogue. *Journal of the Mechanical Behavior of Biomedical Materials* 9, 184-197.
- Kettler, M., Biberthaler, P., Braunstein, V., Zeiler, C., Kroetz, M. and Mutschler, W., 2006. Treatment of proximal humeral fractures with the PHILOS angular stable plate. Presentation of 225 cases of dislocated fractures. *Der Unfallchirurg* 109, 1032-40.
- Kharazi, A. Z., Fathi, M. H. and Bahmany, F., 2010. Design of a textile composite bone plate using 3D-finite element method. *Materials & Design* 31, 1468-1474.
- Kim, S. H., Chang, S. H. and Jung, H. J., 2010. The finite element analysis of a fractured tibia applied by composite bone plates considering contact conditions and time-varying properties of curing tissues. *Composite Structures* 92, 2109-2118.
- Kitsis, C. K., Marino, A. J., Krikler, S. J. and Birch, R., 2003. Late complications following clavicular fractures and their operative management. *Injury* 34, 69-74.
- Koike, Y., Komatsuda, T. and Sato, K., 2008. Internal fixation of proximal humeral fractures with a Polarus humeral nail. *J Orthopaed Traumatol* 9, 135-139.
- Koval, K. J., Blair, B., Takei, R., Kummer, F. J. and Zuckerman, J. D., 1996. Surgical neck fractures of the proximal humerus: a laboratory evaluation of ten fixation techniques. *J Trauma* 40, 778-83.
- Kurtz, S. M. and Devine, J. N., 2007. PEEK biomaterials in trauma, orthopedic, and spinal implants. *Biomaterials* 28, 4845-4869.
- Kwon, B. K., Goertzen, D. J., O'Brien, P. J., Broekhuysse, H. M. and Oxland, T. R., 2002. Biomechanical evaluation of proximal humeral fracture fixation supplemented with calcium phosphate cement. *J Bone Joint Surg Am* 84, 951-61.
- Lill, H., Hepp, P., Korner, J., Kassi, J. P., Verheyden, A. P., Josten, C. and Duda, G. N., 2003. Proximal humeral fractures: how stiff should an implant be? *Arch Orthop Trauma Surg* 123, 74-81.
- Lim Fat, D., Kennedy, J., Galvin, R., O'Brien, F., Mc Grath, F. and Mullett, H., 2012. The Hounsfield value for cortical bone geometry in the proximal humerus—an in vitro study. *Skeletal Radiology* 41, 557-568.
- Low, K. L., Tan, S. H., Zein, S. H. S., Roether, J. A., Mouriño, V. and Boccaccini, A. R., 2010. Calcium phosphate-based composites as injectable bone substitute materials. *Journal of Biomedical Materials Research Part B: Applied Biomaterials* 94B, 273-286.
- Maldonado, Z. M., Seebeck, J., Heller, M. O. W., Brandt, D., Hepp, P., Lill, H. and Duda, G. N., 2003. Straining of the intact and fractured proximal humerus under physiological-like loading. *J Biomech* 36, 1865-1873.
- Mathison, C., Chaudhary, R., Beaupre, L., Reynolds, M., Adeeb, S. and Bouliane, M., 2010. Biomechanical analysis of proximal humeral fixation using locking plate fixation with an intramedullary fibular allograft. *Clin Biomech* 25, 642-646.
- Muckter, H., Herzog, L., Becker, M., Vogel, W., Meeder, P. J. and Buchholz, J., 2001. Angle- and rotation-stable internal fixation of proximal humerus fractures with the humerus fixator plate. Early clinical experience with a newly developed implant. *Der Chirurg; Zeitschrift für alle Gebiete der operativen Medizin* 72, 1327-35.

- Müller, M. E., 1990. The comprehensive classification of fractures of long bones, Springer-Verlag.
- Mullins, L. P., Bruzzi, M. S. and McHugh, P. E., 2009. Calibration of a constitutive model for the post-yield behaviour of cortical bone. *Journal of the Mechanical Behavior of Biomedical Materials* 2, 460-470.
- Neviaser, A. S., Hettrich, C. M., Beamer, B. S., Dines, J. S. and Lorich, D. G., 2011. Endosteal Strut Augment Reduces Complications Associated With Proximal Humeral Locking Plates. *Clin. Orthop. Relat. Res*, 3300-3306.
- Owsley, K. C. and Gorczyca, J. T., 2008. Displacement/Screw Cutout After Open Reduction and Locked Plate Fixation of Humeral Fractures. *J Bone Joint Surg Am* 90, 233-240.
- Ponnappan, R. K., Serhan, H., Zarda, B., Patel, R., Albert, T. and Vaccaro, A. R., 2009. Biomechanical evaluation and comparison of polyetheretherketone rod system to traditional titanium rod fixation. *The Spine Journal* 9, 263-267.
- Poppen, N. K. and Walker, P. S., 1978. Forces at the Glenohumeral Joint in Abduction. *Clin Orthop* 135, 165-170.
- Resch, H., 2011. Proximal humeral fractures: current controversies. *J Shoulder Elbow Surg* 20, 827-832.
- Resch, H., Povacz, P., Frohlich, R. and Wambacher, M., 1997. Percutaneous fixation of three-and four-part fractures of the proximal humerus. *J Bone Joint Surg Br* 79, 295-300.
- Rho, J. Y., Hobatho, M. C. and Ashman, R. B., 1995. Relations of mechanical properties to density and CT numbers in human bone. *Medical Engineering & Physics* 17, 347-355.
- Ring, D., McKee, M. D., Perey, B. H. and Jupiter, J. B., 2001. The use of a blade plate and autogenous cancellous bone graft in the treatment of ununited fractures of the proximal humerus. *Journal of Shoulder and Elbow Surgery* 10, 501-507.
- Rose, D. M., Sutter, E. G., Mears, S. C., Gupta, R. R. and Belkoff, S. M., 2010. Proximal Humeral Fractures. *Geriatric Orthopaedic Surgery & Rehabilitation* 1, 73-7.
- Rose, P. S., Adams, C. R., Torchia, M. E., Jacofsky, D. J., Haidukewych, G. G. and Steinmann, S. P., 2007. Locking plate fixation for proximal humeral fractures: initial results with a new implant. *J Shoulder Elbow Surg* 16, 202-207.
- Sobieraj, M. C., Kurtz, S. M. and Rimnac, C. M., 2009. Notch sensitivity of PEEK in monotonic tension. *Biomaterials* 30, 6485-6494.
- Sobieraj, M. C., Murphy, J. E., Brinkman, J. G., Kurtz, S. M. and Rimnac, C. M., 2010. Notched fatigue behavior of PEEK. *Biomaterials* 31, 9156-9162.
- Viceconti, M., Ricci, S., Pancanti, A. and Cappello, A., 2004. Numerical model to predict the longterm mechanical stability of cementless orthopaedic implants. *Med Biol Eng Comput* 42, 747-753.
- Yamada, M., Briot, J., Pedrono, A., Sans, N., Mansat, P., Mansat, M. and Swider, P., 2007. Age- and gender-related distribution of bone tissue of osteoporotic humeral head using computed tomography. *Journal of Shoulder and Elbow Surgery* 16, 596-602.
- Yáñez, A., Carta, J. A. and Garcés, G., 2010. Biomechanical evaluation of a new system to improve screw fixation in osteoporotic bones. *Medical Engineering & Physics* 32, 532-541.

4.6 Appendix 4A

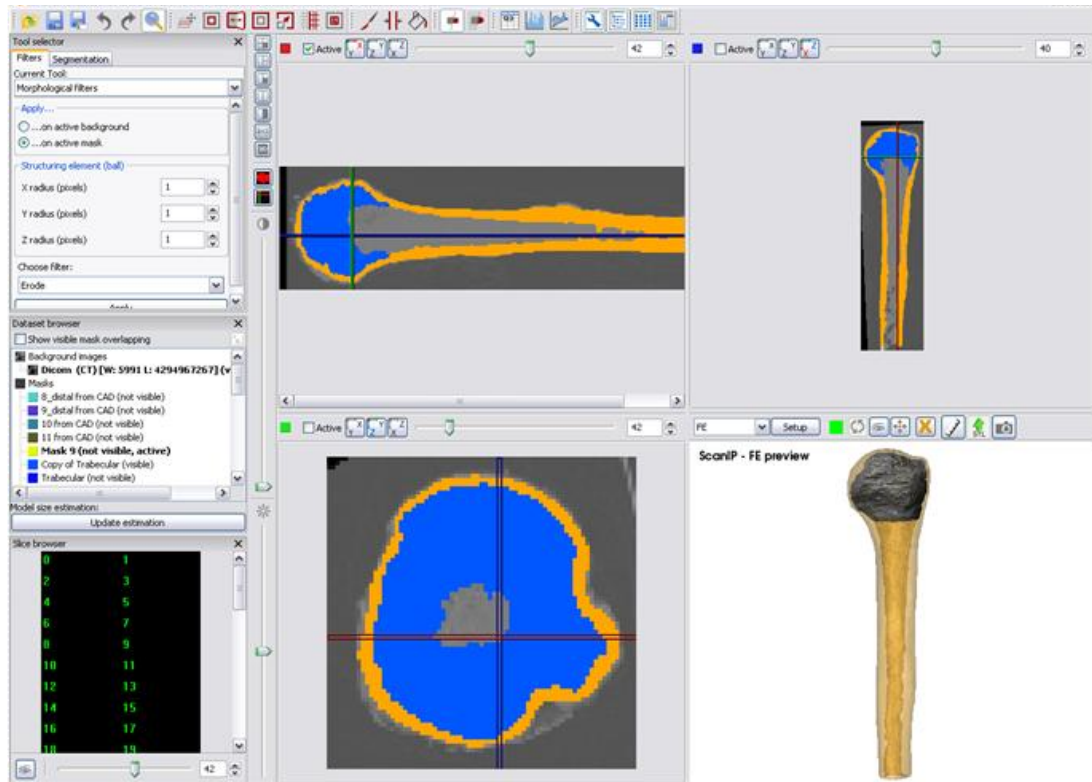


Figure 4A.1 Model Generation of intact specimen model of cortical and cancellous bone volumes from CT scans using Simpleware

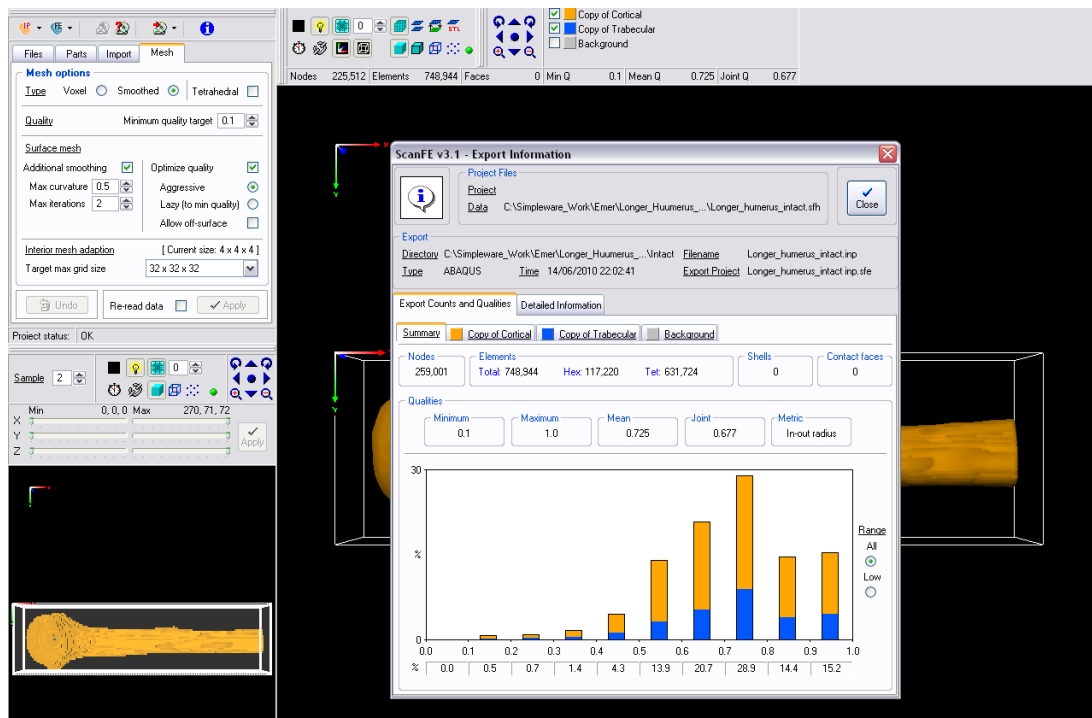


Figure 4A.2 Mesh data for intact humerus model generated using Simpleware

Chapter 5

Experimental Study of Cortical Bone Screw Pullout

Abstract

An experimental study of screw pullout from cortical bone has been conducted. A novel modification of standard screw pullout tests, which provided real time image capture of damage mechanisms during pullout, was developed. Pullout forces, measured using the novel test rig, were validated against standard pullout tests. Osteon alignment was considered during pullout tests, to investigate the effect of osteons aligned parallel to the axis of the orthopaedic screw (longitudinal pullout), as well as the effect of osteons aligned perpendicular to the axis of the screw (transverse pullout). Distinctive alternate failure mechanisms were uncovered for longitudinally and transversely orientated cortical bone during screw pullout. Vertical crack propagation, parallel to the axis of the screw, was observed for a longitudinal pullout. Horizontal crack propagation, perpendicular to the axis of the screw, was observed for a transverse pullout.

5.1 Introduction

Cortical bone is a naturally occurring composite. The constituents can be classified as organic and inorganic phases and water. The organic phase consists of impure hydroxyapatite, while the inorganic phase consists mainly of collagen. At the micro-scale, arrangement of the constituents can be seen as stacks of concentric collagen sheets with a central Haversian canal forming osteons which are embedded in an interstitial matrix of hydroxyapatite. In long whole bones, osteons are aligned parallel to the central axis of the bone (Rho et al. (1998); Cowin (2001)).

Orthopaedic screws are used as the primary mode of fixation for applications such as fracture plates (Kwon et al. (2002)), intramedullary rods (Cuny et al. (2008)), spinal devices (GainesJr (2000)) and suture anchors (Barber et al. (2008)). Screw pullout is a commonly reported clinical problem (Owsley and Gorczyca (2008)). Maximising the insertion depth of screws in cortical bone has been shown to significantly increase the pullout strength of orthopaedic screws. Pollard et al. (2010) reported that a bicortical fixation, with a screw inserted through the lateral cortex and anchored in

the opposite cortical wall, significantly increased the strength of fixation. The ability of devices to perform as designed is dictated by the pullout strength of the screws anchoring them. The failure mechanisms that lead to screw pullout have not previously been uncovered.

The objective of Chapter 5 is to experimentally identify the failure mechanisms that lead to screw pullout from cortical bone. In order to uncover these failure mechanisms, a novel test rig was developed. This modification of standard pullout tests (ASTMF543-07) facilitates live imaging of crack initiation and propagation as the screw is removed from the bone.

5.2 Materials and Methods

5.2.1 Sample preparation

Cortical bone samples (24x20x10mm) were extracted from the mid-diaphysis of a bovine metacarpus, parallel to the central axis of the bone. A sample extracted with osteons aligned parallel to the cut direction was referred to as a longitudinal sample. A sample extracted with osteons aligned perpendicular to the cut direction was referred to as a transverse sample. An illustration of osteon alignment within samples is shown in Figure 5.1. The bovine bone was obtained from an abattoir within a few hours post mortem. The samples were extracted within 24 hours and were kept hydrated in saline solution while refrigerated at 3° C until testing. All testing was carried out within 14 days post mortem. A high speed bandsaw (Jubilee VBS 360, Addison Saws Ltd., West Midlands, UK) was used to make initial extraction of samples. Samples were sanded in saline solution to obtain polished surfaces for testing.

5.2.2 Orthopaedic Cortical Bone Screws

Commercially available 3.5mm cortical bone screws (Arthrex Inc., Naples, Florida, USA) were used for the pullout tests (Figure 5.2). These screws are used in the Arthrex Humeral Suture Locking Plate (Arthrex Inc., Naples, Florida, USA). These screws are self tapping with an inner diameter of 2.5 mm. Guidelines provided by the manufacturer stated that a pilot hole of 2.5 mm should be drilled prior to insertion.

The self-tapping screw was inserted into all samples with torque limited to 1.5Nm (as specified by manufacturer).

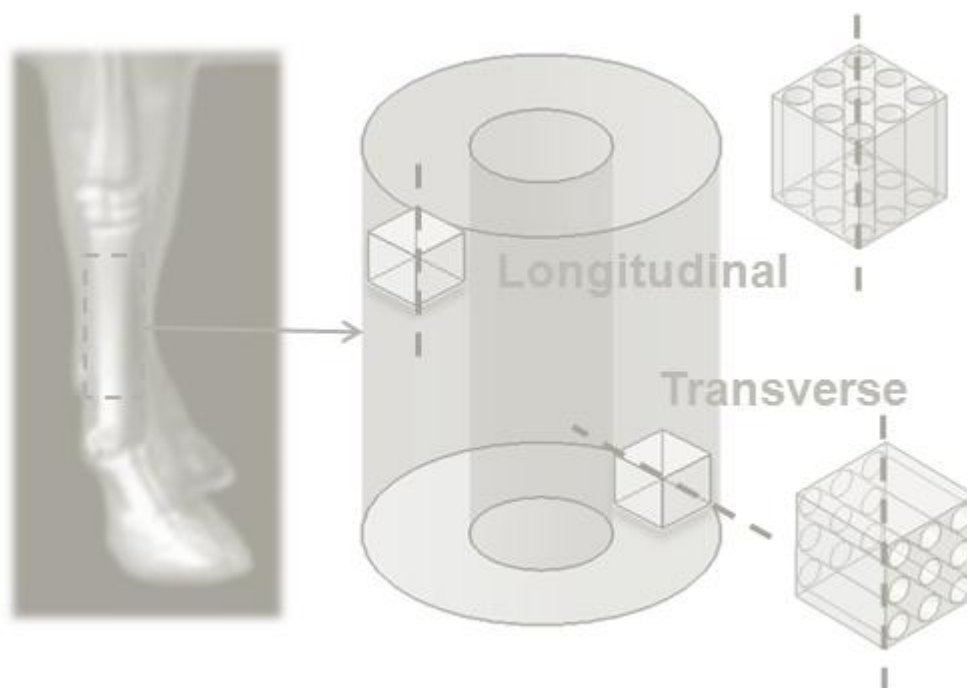


Figure 5.1 Samples extracted from bovine metacarpus considering osteon alignment. A sample extracted with osteons aligned parallel to the cut direction was referred to as a longitudinal sample. A sample extracted with osteons aligned perpendicular to the cut direction was referred to as a transverse sample.

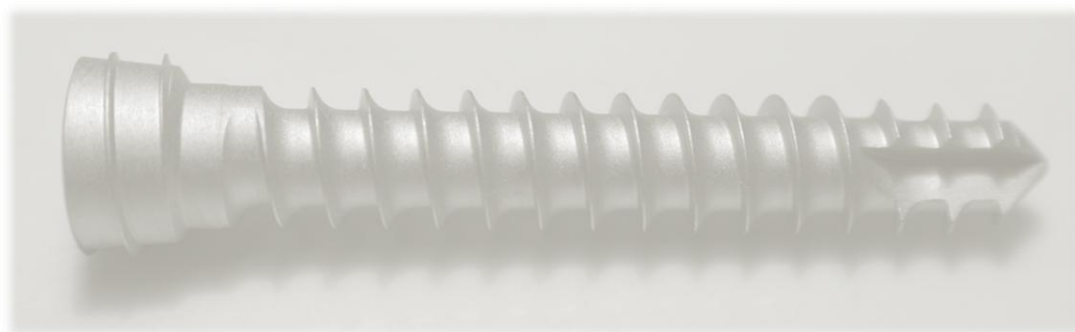


Figure 5.2 3.5 mm cortical bone screws with an inner diameter of 2.5 mm. The screws are self tapping with a cutting flute detail at the tip of the screw. The head of the screw is also threaded so that the screw locks into the threaded holes of the plate.

5.2.3 Standard Pullout Tests

Standard pullout tests were conducted according to ASTM F543-07, where screws were fully embedded in cortical bone blocks. The test rig for complete pullout is shown in the Figure 5.3. The bone sample was clamped on all four sides. The top plate of the rig, with a square window of 24 x 20 mm, prevented the sample moving upwards. A pilot hole of 2.5 mm was drilled in the secured sample and screws were inserted at a depth of 8mm. Insertion torque did not exceed 1.5 Nm. The screw heads were gripped using a clamp for load application. Tests were carried out using an Instron (Model 8500, Instron, UK) 10kN load cell. The test set up is illustrated in the images of Figure 5.4.

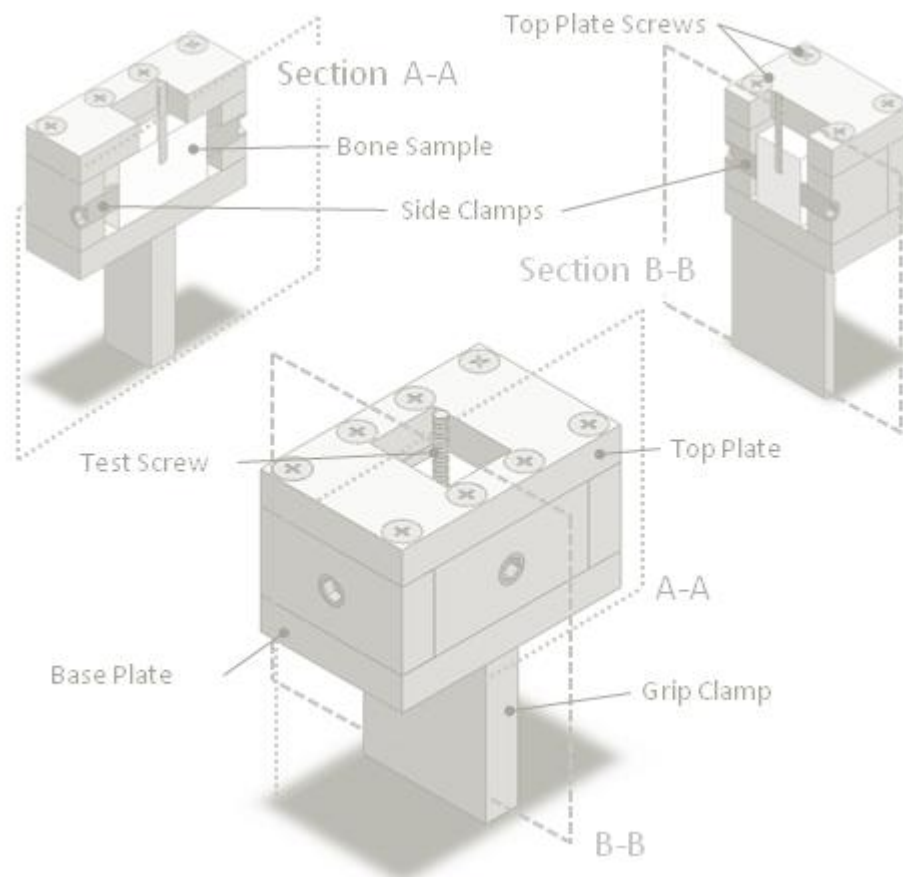


Figure 5.3 Complete pullout test rig. Samples were clamped on four sides with top plate preventing upward motion of sample. Section views highlight clamping of sample.

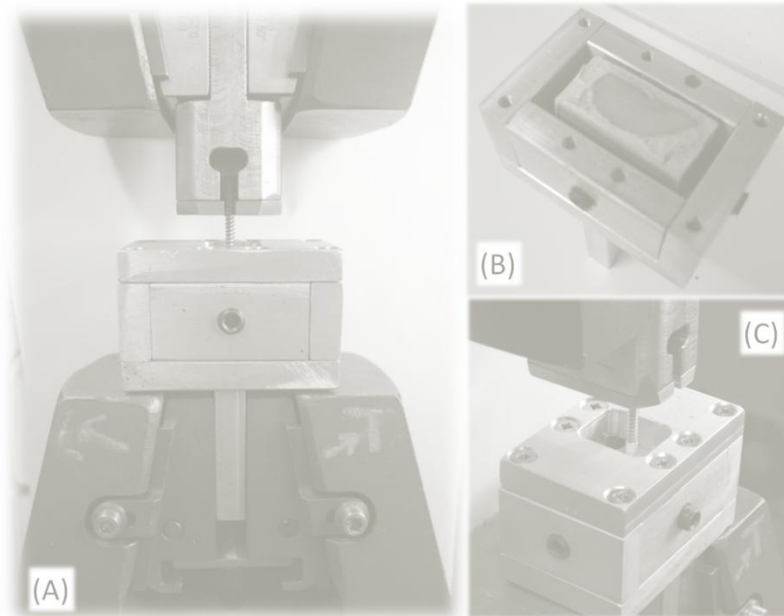


Figure 5.4 Complete pullout test rig; (A) Test rig clamped in Instron test machine with screw head gripped in upper rig; (B) Bone sample embedded in resin to facilitate tighter clamping of samples; (C) Side view of screw removed from sample.

5.2.4 Screw Pullout Damage Visualisation Test (SPDV)

A novel test rig was developed to facilitate real-time imaging of bone damage during screw pullout, which this chapter refers to as a Screw Pullout Damage Visualisation (SPDV) test. A schematic of the SPDV rig is shown in Figure 5.5, illustrating key design components [A-H]. The rig created a 180° symmetric pullout test. The bone was held in position in the x and z directions by three clamping screws at the sides and rear of the sample (Figure 5.5D). The bone was held in position in the y direction by a retaining plate (Figure 5.5E). Half of the screw (Figure 1A) was embedded in cortical bone (Figure 5.5B) while the remaining half was embedded in a poly methyl methacrylate slider (Figure 5.5C). This created a window to monitor crack initiation and propagation (Figure 5.6). The slider was free to move upwards in the y direction and acted as a guide during the pullout test. The slider was prevented from moving in the z direction by a poly methyl methacrylate window (Figure 5.5F), which was bolted to the test rig frame. In summary, the slider and window provided screw guidance and symmetric constraints on the cortical bone during pullout. It is important to note that the slider merely underwent rigid body motion with the screw in the y-direction, so that pullout force was dictated exclusively by the cortical bone.

Forces due to friction between the slider and the bone were found to be negligible (< load cell sensitivity of 0.5N).

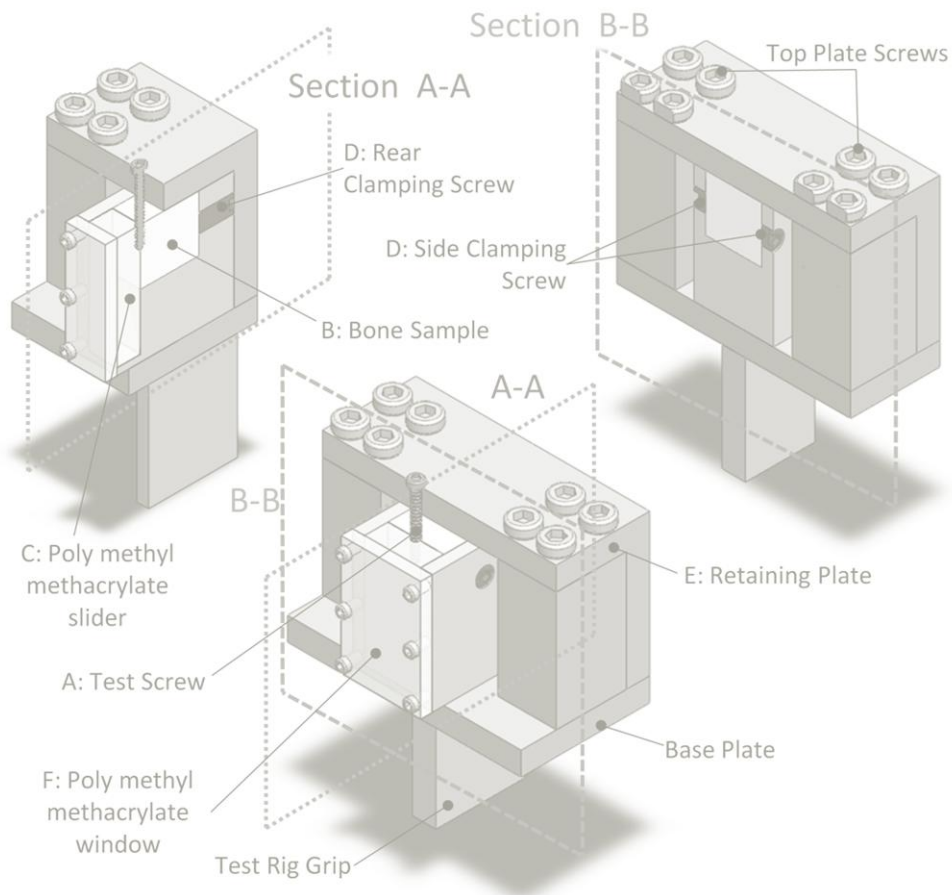


Figure 5.5 Schematic of Experimental test rig for SPDV test with section view A-A and B-B highlighting inner test rig components

A 2.5mm pilot hole was drilled at the interface between the slider and the cortical bone, which created a shaft of radius 1.25mm in both materials. The self-tapping screw was inserted to a depth of 8mm into the bone and Perspex slider, with the maximum applied torque limited to 1.5 Nm (as specified by the screw manufacturer). The samples were positioned in the test rig with osteons aligned parallel and perpendicular to the axis of the screw. Tests conducted with osteons aligned parallel to the axis of the screw, as shown in Figure 5.7A, were referred to as “longitudinal pullout tests”. Tests conducted with osteons aligned perpendicular to the screw axis, as shown in Figure 5.7B, were referred to as “transverse pullout tests”. Two sample t-tests were conducted to determine the statistical significance of the results ($\alpha < 0.05$).

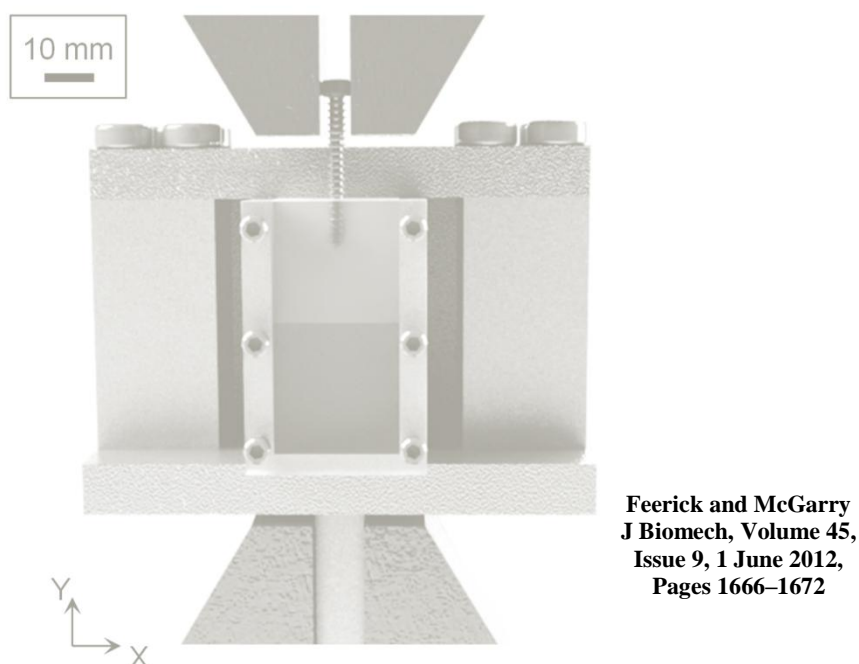


Figure 5.6 Experimental test rig for SPDV test. Front view, highlighting the screw embedded in bone

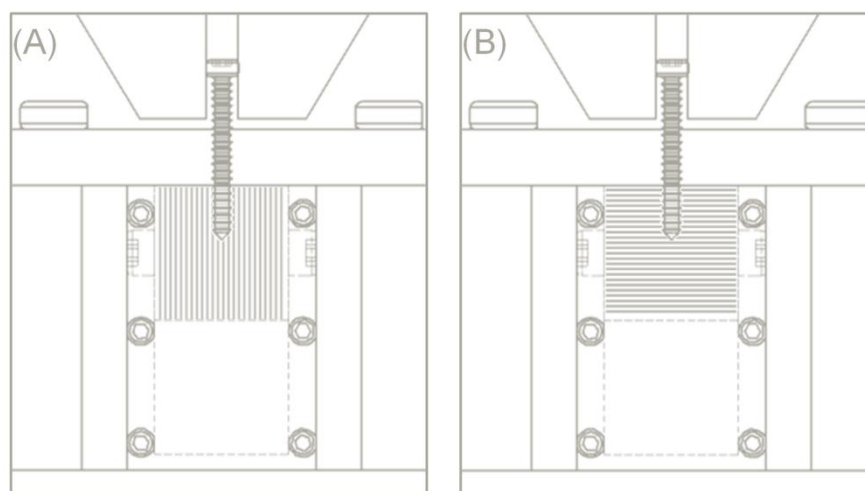


Figure 5.7 (A) Longitudinal SPDV test, with osteons aligned parallel to the axis of the screw; (B) Transverse SPDV test, with osteons aligned perpendicular to the axis of the screw

5.2.5 Comparison of Standard Pullout and SPDV Tests

Measured forces recorded for a complete pullout were multiplied by a factor of 0.5; in order to validate forces measured using the Screw Pullout Damage Visualisation (SPDV) test method. This was due to the fact that only half of the screw was embedded in cortical bone for an SPDV test compared to a complete pullout test.

Therefore, the pullout force exerted on the screw should be half the value recorded for a complete pullout. Each set of experimental tests had a sample size of five. Two sample t-tests were conducted to determine statistical significance of the results ($\alpha < 0.05$).

5.2.6 SPDV Test Image Capture

A dual camera system was used to record the pullout test and load data simultaneously (Figure 5.8). A magnification (X10) lens captured an optical window of 24x8 mm during the pullout test, at a rate of 60 frames per second. Simultaneously, a second camera recorded the load displacement data displayed on the Instron console. The cameras were synchronised prior to testing to determine the time lag between them. A circular fluorescent light was used to aid visualisation of the sample during the test.

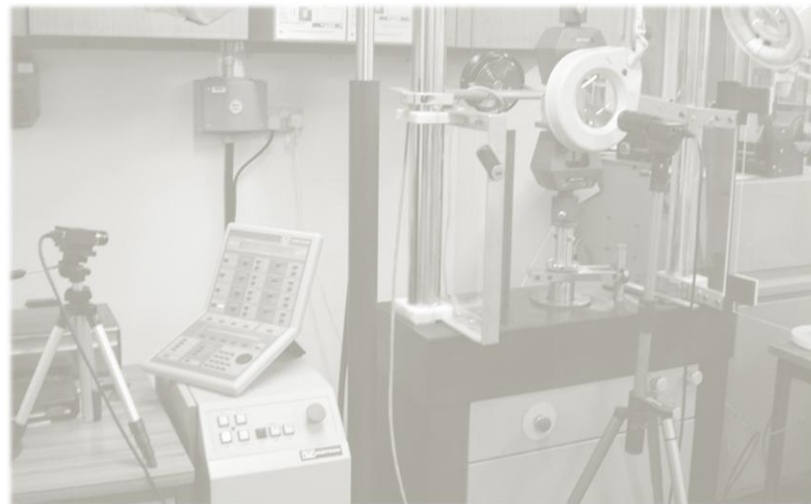


Figure 5.8: Dual camera live imaging of load displacement data and failure mode as screw was removed from the bone sample.

5.3 Results

The results of this chapter are presented in two parts. The results from a standard complete pullout are first presented for both longitudinally and transversely aligned cortical bone. The results obtained from the SPDV test are then presented with comparison to the load displacement data observed for complete pullout. A summary of the pullout forces for each sample is provided in Table 5.1.

Table 5.1: Pullout forces recorded for standard pullout and SPDV tests, for longitudinal and transverse samples

Sample	Standard Pullout Force (kN)		SPDV Pullout Force (kN)	
	Longitudinal	Transverse	Longitudinal	Transverse
1	2.19	5.00	1.62	1.67
2	2.66	3.91	0.86	1.69
3	2.21	4.76	0.57	2.15
4	2.44	4.03	1.51	2.19
5	2.45	3.85	1.11	1.96
Average	2.39	4.31	1.13	1.93
Standard Deviation	0.19	0.54	0.44	0.24

5.3.1 Complete Pullout

5.3.1.1 Longitudinal Pullout Results

The experimental failure mode observed for a complete longitudinal pullout is summarised in Figure 5.9 below. The bone between the screw threads remained between the threads after removal as shown by Figure 5.9(A & C). When the screw was removed from the bone a cleared out hole remained, with no visible bone deformation. Whitening was observed in the area immediately surrounding the edge of the hole, as highlighted in Figure 5.9B.

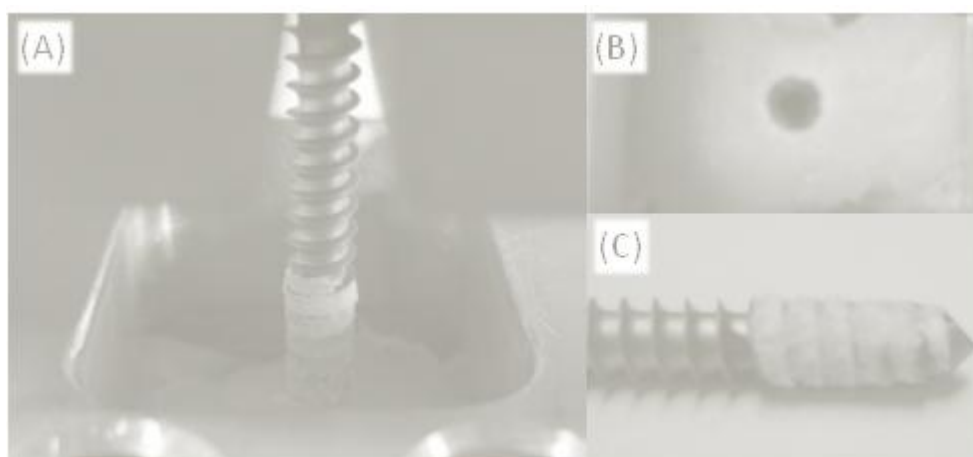


Figure 5.9 Longitudinal complete pullout failure mode; (A) Side view of standard pullout post test; (B) Cortical bone top surface; (C) Bone remains between screw threads once the screw is removed.

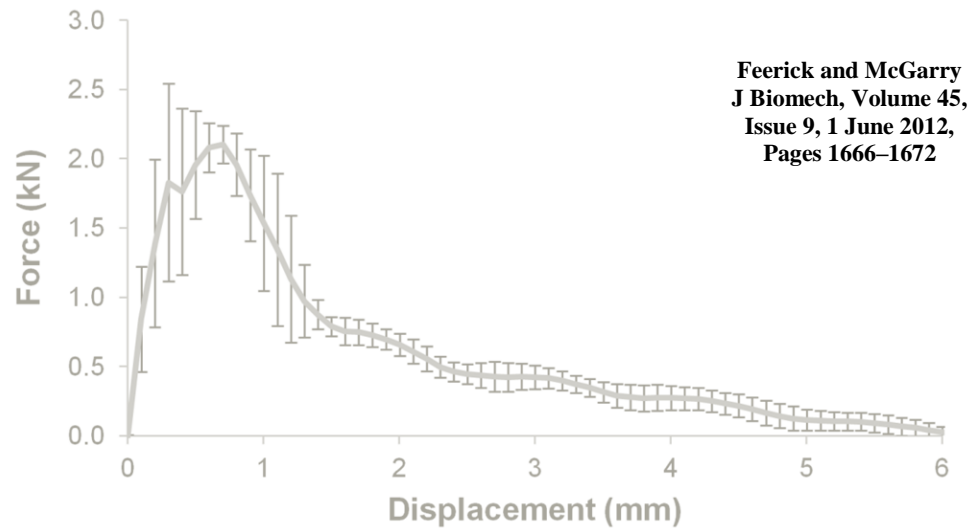


Figure 5.10 Average longitudinal complete pullout load displacement curve.

The average load displacement data for a longitudinal complete pullout is shown in Figure 5.10. The material followed a non linear response up to a peak load of 2.39 kN at 0.7 mm, with an average standard deviation of ± 0.19 kN. There was minimal plastic deformation observed prior to failure of the material. Once the peak load was reached an immediate drop in load occurred followed by a gradual degradation of the loading curve as the screw was removed from the bone. It is suggested that this gradual degradation of the loading curve was due to friction between the fracture surfaces as the screw was removed.

5.3.1.2 Transverse Pullout Results

The experimental failure mode observed for a transverse complete pullout is shown in Figure 5.11. Large deformation and whitening of the material was observed several millimetres away from the screw edge. Figure 5.11B shows the fracture fragments observed post pullout. It was observed that less material remained between the screws threads (Figure 5.11C) in comparison with a longitudinal pullout.

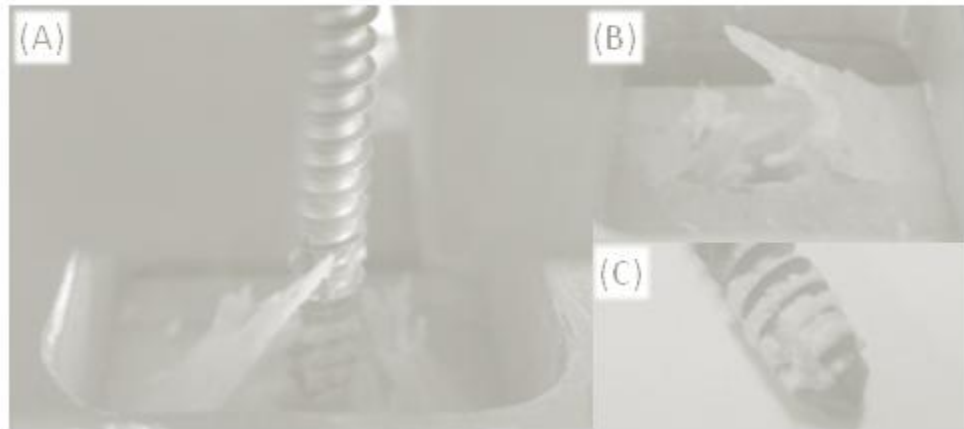


Figure 5.11 Transverse complete pullout failure mode; (A) Side view of standard pullout post test; (B) Cortical bone top surface; (C) Bone remained between screw threads once the screw was removed.

The average load displacement data for a transverse complete pullout is shown in Figure 5.12. An average peak load of 4.31 kN was observed at 0.8 mm, with an average standard deviation of 0.54 kN. Plastic deformation was observed prior to failure. The peak load recorded for a transverse pullout was a factor of 2 higher than a longitudinal pullout. Once the peak load was reached, an immediate drop in load occurred, followed by a more rapid degradation of load compared with longitudinal pullout, as the screw was removed from the bone.

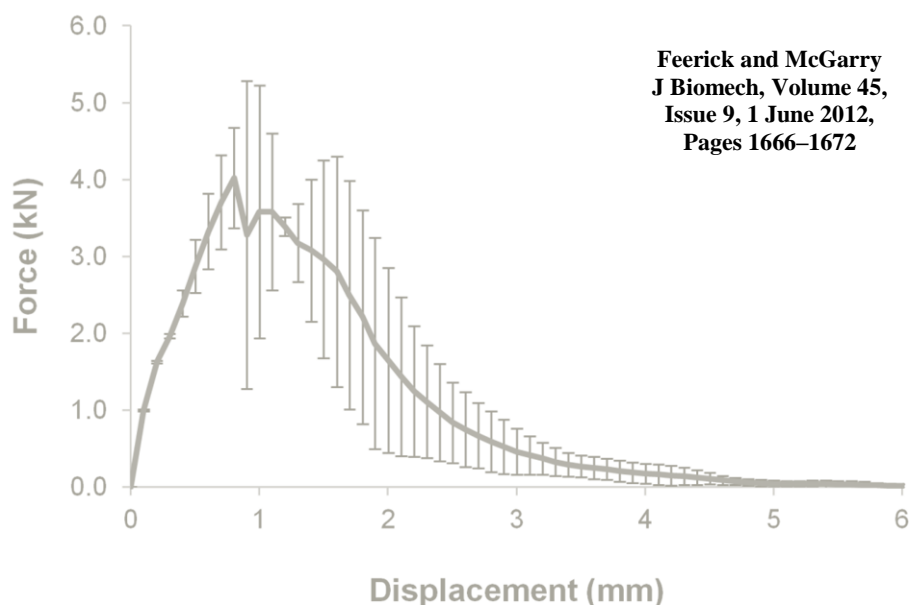


Figure 5.12 Average transverse complete pullout load displacement curve.

5.3.2 Screw Pullout Damage Visualisation

5.3.2.1 SPDV Longitudinal Pullout Results

The force displacement curve for a longitudinal SPDV test is shown in Figure 5.13. The average peak load recorded for the longitudinal SPDV test was 1.13 kN, with a standard deviation of 0.44 kN. In order to determine the accuracy of the SPDV test, the average peak load recorded for 5 complete pullouts was halved (1.195 kN), no statistical significance between tests was observed ($p=0.763$).

Images of the failure mechanisms, captured during a longitudinal SPDV test, are collated in Figure 5.14. The initial position of the screw is shown in Figure 5.14(i). Once peak load was reached some areas of localised whitening were evident at the screw tips (Figure 5.14(ii)). Once the peak load was reached (Figure 5.14(iii)), vertical cracks formed upwards from the screw thread tips, the bone between the screw threads detached and was removed with the screw (Figure 5.14(v)). This left a cleared out hole with no thread definition, as shown in Figure 5.14(vi).

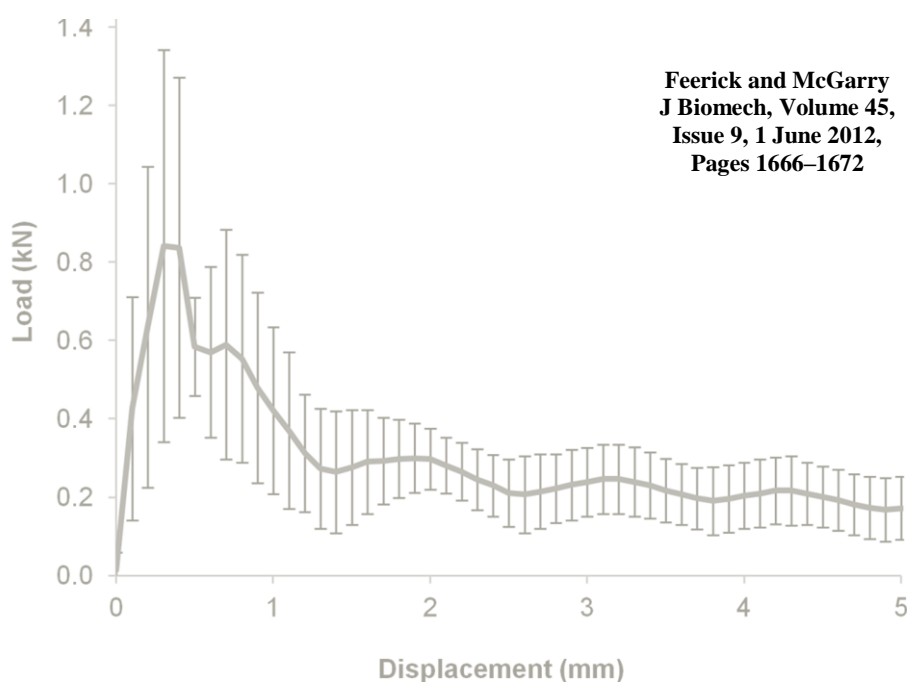


Figure 5.13 Average Load displacement for longitudinal SPDV test.

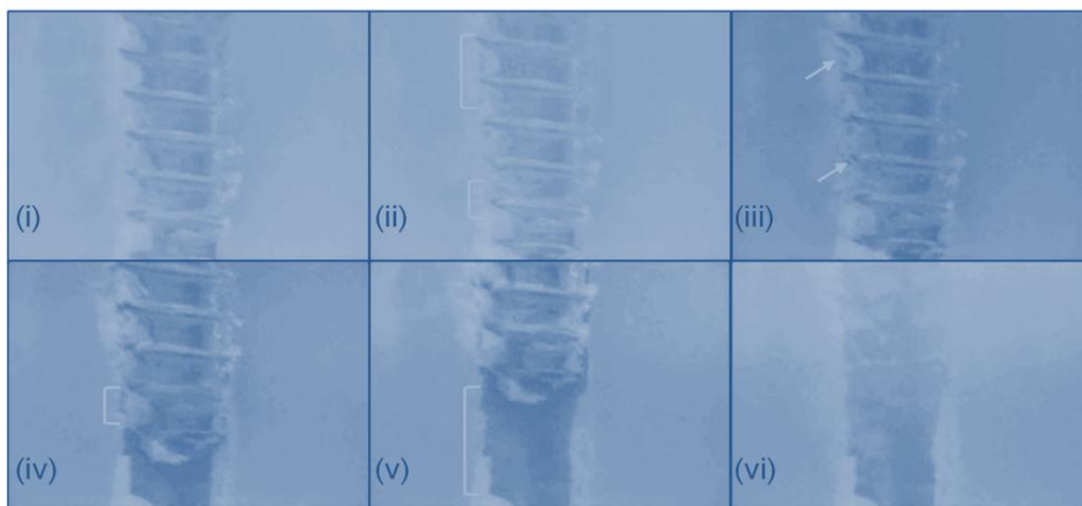


Figure 5.14 Longitudinal SPDV test experimental failure mode images: (i) Initial screw position, (ii) At peak load, areas of localised whitening were evident at the screw thread tips; (iii) Crack initiation occurred immediately post peak load; (iv) Cracks propagated vertically upwards from screw thread tips; (v) Material detachment occurred as cracks propagated further, bone remained between screw threads as screw was removed; (vi) Final position, smoothed fracture surface remained with no thread definition.

Magnified images of the failure surface, post testing, for a longitudinal pullout are shown in Figure 5.15. The jagged surface following pullout was clearly visible as well as the localised deformation with no obvious material deformation away from the failure surface.

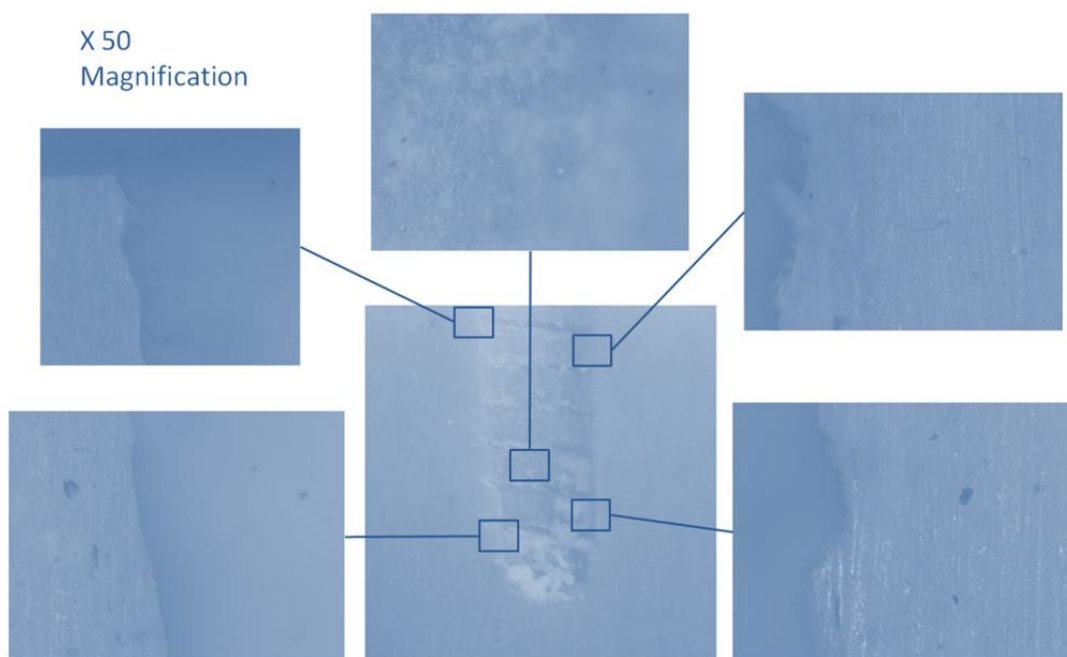


Figure 5.15 Magnified (x50) fracture surface images post longitudinal SPDV test

5.3.2.2 SPDV Transverse Pullout Results

The average peak load for the transverse SPDV test (Figure 5.16) was 1.93 kN, with a standard deviation of 0.24 kN. The halved average peak load (2.155 kN) for transverse complete pullout tests also revealed no statistical difference between the peak loads ($p=0.21$).

In both tests we saw that the transverse pullout tests required a peak load which was a factor of two higher than in the longitudinal direction. This validated the force data reported by the SPDV test, which facilitated failure mode viewing as well as reliable load data.

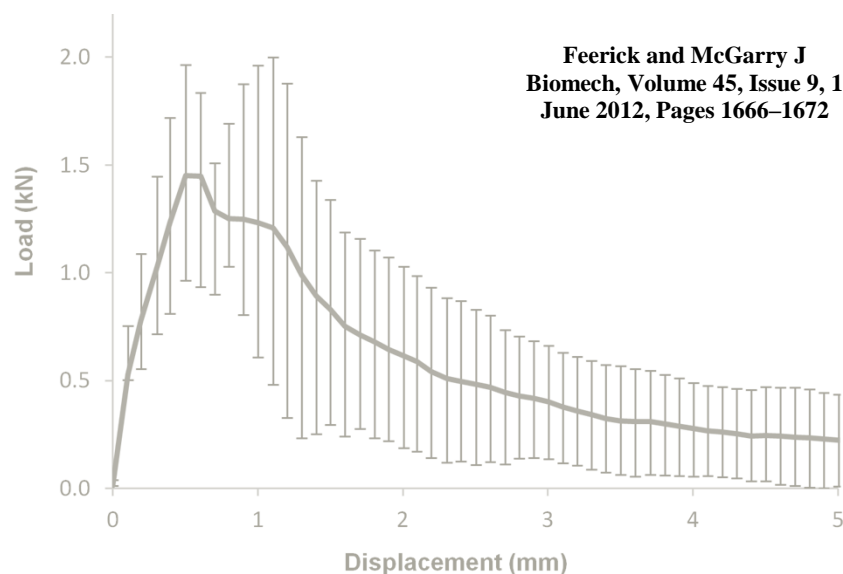


Figure 5.16 Force displacement curve from transverse SPDV tests.

Images of the failure mechanisms, captured during a transverse SPDV test, are collated in Figure 5.17 with initial position shown in Figure 5.17(i). At peak load (Figure 5.17(ii)), whitening of the material extended horizontally outwards from the screw threads. This whitening was much more extensive than observed during longitudinal pullout. Crack initiation occurred at these whitened locations (Figure 5.17(iii)). Importantly, cracks were oriented in the horizontal direction. As the test progressed, further whitening occurred and horizontal cracks propagated into the bone (Figure 5.17(iv)). As the screw was removed, the bone above the horizontal cracks underwent bending and detached itself from undeformed bone, as highlighted in Figure 5.17(v). Following complete screw pullout, a jagged irregular fracture

surface was revealed. Clearly this failure mode was distinctly different to the failure mode observed during the longitudinal SPDV, which resulted in localised vertical crack formation, with no significant bone deformation observed beyond the screw thread tips (Figure 5.14(vi)).

Magnified images of the failure surface, post testing, for a transverse pullout is summarised in Figure 5.18. The horizontal cracks that propagated were clearly visible, with the crack tip extending several millimetres into the surrounding bone.

Feerick and McGarry *J Biomech*, Volume 45, Issue 9, 1 June 2012, Pages 1666–1672

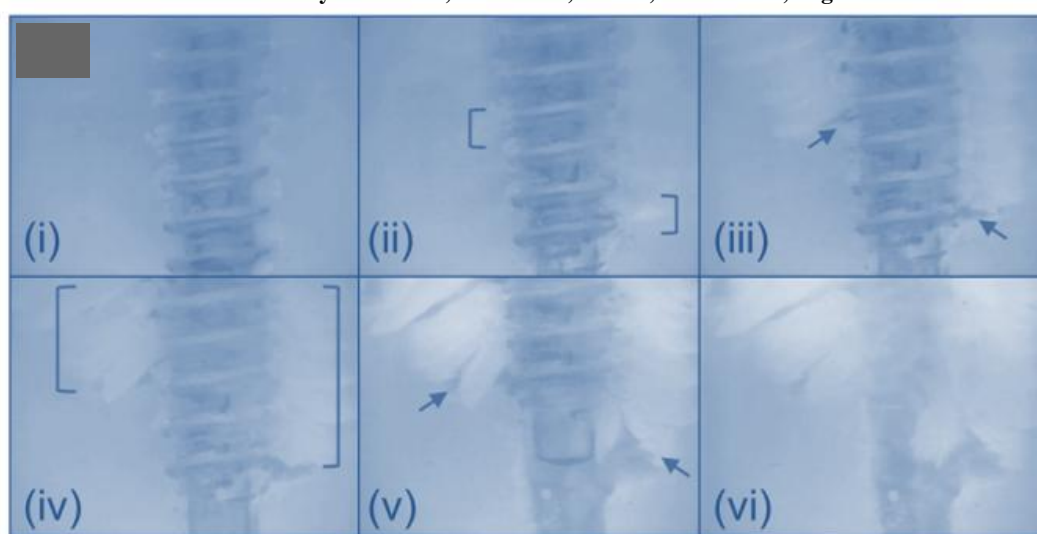


Figure 5.17 Transverse SPDV test experimental failure mode images: (i) Initial screw position, (ii) At peak load, whitening of bone extended horizontally outwards from the screw threads; (iii) Crack initiation occurred in the horizontal direction; (iv) Crack progression was observed in the horizontal direction with further whitening of the bone; (v) Material detachment occurred as the bone underwent bending and further deformation as the screw was removed; (vi) Final position, a jagged irregular fracture surface remained.

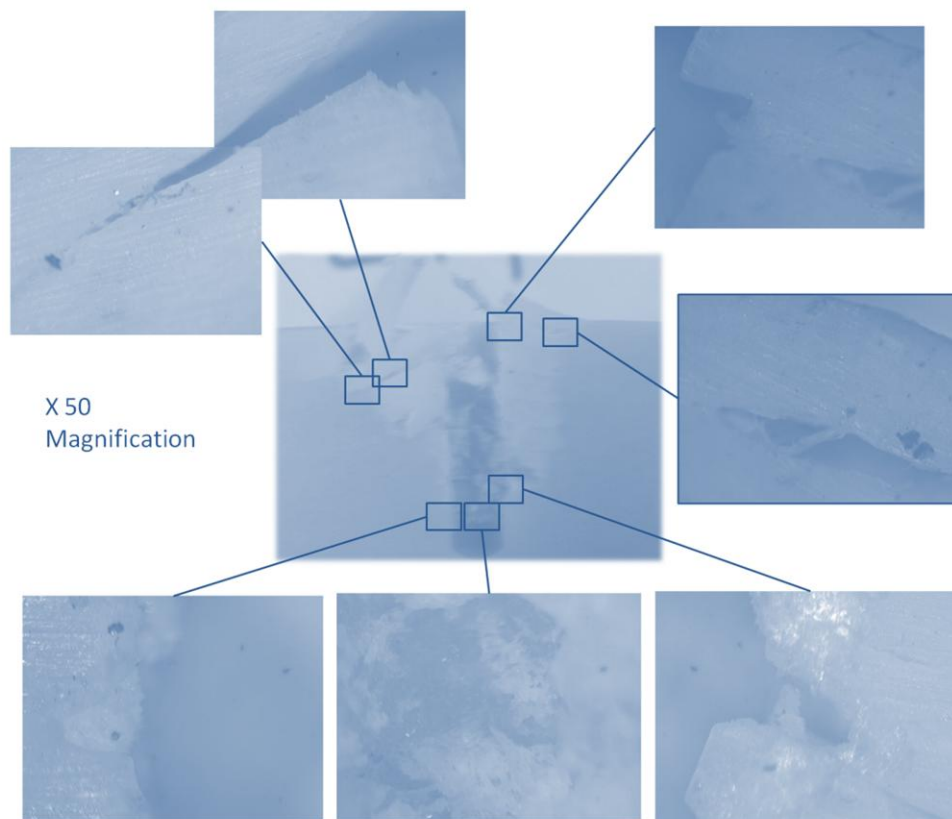


Figure 5.18 Magnified (x50) fracture surface images post transverse SPDV test

5.4 Discussion

The novel experimental SPDV test rig developed for this chapter, uncovers for the first time the distinctive alternate failure mechanisms for longitudinally and transversely orientated cortical bone during screw pullout. The test rig reveals these failure modes in real time as the screw is removed from the cortical bone.

Previous experimental studies of cortical bone have reported significant differences in stiffness and strength in longitudinal and transverse directions (Reilly and Burstein (1975); Ashman et al. (1984)). Higher forces have been documented for transverse pullout compared to longitudinal pullout (Seebeck et al. (2004)), but no failure mechanisms have previously been uncovered. Previous experimental studies of screw pullout have conducted pullout tests from synthetic materials such as Sawbone polyurethane foam (Chapman et al. (1996); Chatzistergos et al. (2010)).

The former study reported the effect of several screw design parameters, such as thread shape factor, major diameter of screw and the length of engagement of the screw. However, due to the fact that the testing was conducted on homogeneous polyurethane foam, the effect of microstructure alignment of the anchoring material could not be investigated. Similarly, Chatzistergos et al. (2010) conducted pullout from polyurethane foam, in this case the samples were cut post testing to examine the fracture surface following screw pullout. Again, since no microstructural representation of bone was possible with these synthetic materials, clean fracture lines were observed with materials between screw threads being removed with the screw. Advancing on previous work, the present chapter experimentally uncovers significantly different failure mechanisms for longitudinal and transverse screw pullout, in addition to differences in pullout force.

Furthermore, the SPDV test demonstrated that damage and crack propagation perpendicular to the screw axis for transverse pullout required large material deformation prior to screw removal. This resulted in higher pull out forces than observed for longitudinal tests, in which crack propagation occurred in a localised region between the screw tips, facilitating screw removal with little deformation of the surrounding bone.

In conclusion, for the first time, the present experimental chapter uncovered the relationship between osteon alignment, crack patterns and failure force for cortical bone screw pullout.

5.5 References

- Ashman, R. B., Cowin, S. C., Van Buskirk, W. C. and Rice, J. C., 1984. A continuous wave technique for the measurement of the elastic properties of cortical bone. *Journal of Biomechanics* 17, 349-361.
- Barber, F. A., Herbert, M. A., Beavis, R. C. and Barrera Oro, F., 2008. Suture Anchor Materials, Eyelets, and Designs: Update 2008. *Arthroscopy: The Journal of Arthroscopic & Related Surgery* 24, 859-867.
- Chapman, J. R., Harrington, R. M., Lee, K. M., Anderson, P. A., Tencer, A. F. and Kowalski, D., 1996. Factors Affecting the Pullout Strength of Cancellous Bone Screws. *Journal of Biomechanical Engineering* 118, 391-398.
- Chatzistergos, P. E., Magnissalis, E. A. and Kourkoulis, S. K., 2010. A parametric study of cylindrical pedicle screw design implications on the pullout performance using an experimentally validated finite-element model. *Medical Engineering & Physics* 32, 145-154.
- Cowin, S. C., 2001. Bone mechanics handbook, CRC press USA.
- Cuny, C., Scarlat, M. M., Irrazi, M., Beau, P., Wenger, V., Ionescu, N. and Berrichi, A., 2008. The Telegraph nail for proximal humeral fractures: A prospective four-year study. *J Shoulder Elbow Surg* 17, 539-545.
- Gaines Jr, R. W., 2000. The Use of Pedicle-Screw Internal Fixation for the Operative Treatment of Spinal Disorders. *The Journal of Bone and Joint Surgery (American)* 82, 1458-1458.
- Kwon, B. K., Goertzen, D. J., O'Brien, P. J., Broekhuysse, H. M. and Oxland, T. R., 2002. Biomechanical evaluation of proximal humeral fracture fixation supplemented with calcium phosphate cement. *J Bone Joint Surg Am* 84, 951-61.
- Owsley, K. C. and Gorczyca, J. T., 2008. Displacement/Screw Cutout After Open Reduction and Locked Plate Fixation of Humeral Fractures. *J Bone Joint Surg Am* 90, 233-240.
- Pollard, J. D., Deyhim, A., Rigby, R. B., Dau, N., King, C., Fallat, L. M. and Bir, C., 2010. Comparison of Pullout Strength between 3.5-mm Fully Threaded, Bicortical Screws and 4.0-mm Partially Threaded, Cancellous Screws in the Fixation of Medial Malleolar Fractures. *The Journal of foot and ankle surgery : official publication of the American College of Foot and Ankle Surgeons* 49, 248-252.
- Reilly, D. T. and Burstein, A. H., 1975. The elastic and ultimate properties of compact bone tissue. *Journal of Biomechanics* 8, 393-396, IN9-IN11, 397-405.
- Rho, J.-Y., Kuhn-Spearing, L. and Zioupos, P., 1998. Mechanical properties and the hierarchical structure of bone. *Medical Engineering & Physics* 20, 92-102.
- Seebeck, J., Goldhahn, J., Städele, H., Messmer, P., Morlock, M. M. and Schneider, E., 2004. Effect of cortical thickness and cancellous bone density on the holding strength of internal fixator screws. *Journal of Orthopaedic Research* 22, 1237-1242.

5.6 Appendix 5A: Test Rig CAD Assembly Drawings

Content Removed Due to Copyright

Content Removed Due to Copyright

5.7 Appendix 5B: Computational Assessment of SPDV Test

Content Removed Due to Copyright

Chapter 6

Computational Study of Cortical Bone Screw Pullout using Element Deletion

Abstract

A computational study of screw pullout from cortical bone has been conducted. Finite element simulation of screw pullout, incorporating material damage and crack propagation, was performed. Simulations revealed that a homogeneous material model for cortical bone predicts vertical crack propagation patterns for both longitudinal and transverse screw pullout. A biphasic multi-layered composite model representing cortical bone microstructure was developed. A unique set of material and damage properties was used for both transverse and longitudinal pullout simulations, with only layer orientations being changed. Simulations predicted: (i) Higher pullout forces for transverse pullout; (ii) Horizontal crack paths perpendicular to screw axis for transverse pullout, whereas vertical crack paths were computed for longitudinal pullout. Computed results agreed closely with experimental observations of Chapter 5 in terms of pullout force and crack propagation.

6.1 Introduction

The objective of this chapter is to develop a predictive computational model capable of replicating the experimentally observed failure modes and peak forces reported in Chapter 5, for screw pullout. Previous computational studies, investigated pullout with homogeneous, isotropic materials (Zhang et al. 2006; Chatzistergos et al. 2010). The current chapter highlights the importance of modelling cortical bone as an inhomogeneous microstructure to simulate realistic pullout failure modes, as crack propagation is dependent upon osteon alignment. A calibrated microstructure model for cortical bone would provide efficient evaluation of thread designs for application specific devices.

6.2 Materials and Methods

All computational simulations were conducted using the finite element solver Abaqus/Explicit 6.9 (Simulia, Providence, RI, USA). A 2D axisymmetric model was created based on the geometry of the screws used for experimental tests. A structured mesh consisting of 35,472 bilinear axisymmetric reduced integration elements (CAX4R), was generated by partitioning the cortical bone geometry (Abaqus, 2009). An element length of 50 μm was used. A mesh sensitivity analysis was conducted for element lengths of 10-200 μm , with convergence of failure load and crack patterns being observed for element lengths of 50 μm or less. Internal (IE) and kinetic (KE) energies were monitored for all simulations, to ensure that KE never exceeded 5% of IE, as shown in Figure 6.1. This ensured inertia effects were insignificant for explicit simulations (Abaqus, 2009).

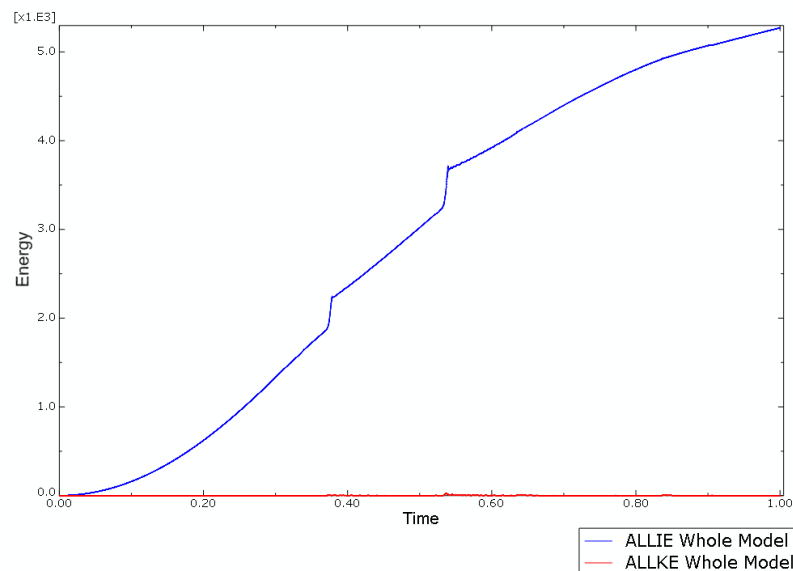


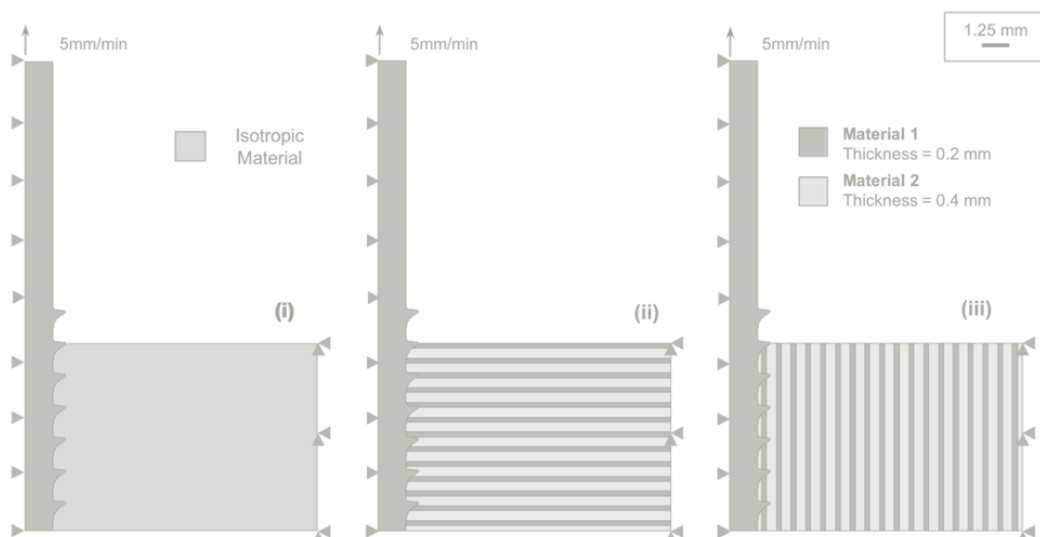
Figure 6.1 Plot of kinetic (ALLKE) and internal (ALLIE) energy of the model during pullout simulation.

Initially, the cortical bone was modelled as a homogeneous elasto-plastic material (Model A, Figure 3(i)). Inelastic material behaviour was modelled using Drucker-Prager plasticity (Table 6.1)(Drucker and Prager (1952); Derikx et al. (2011)) (Further detail of Drucker Prager model provided in Chapter 3).

Table 6.1 Fixed parameters for all computational models

Density (kg/m^3)	1960
Drucker Prager Flow Stress Ratio (K)	1
Drucker Prager Friction Angle (β)	43.5°
Drucker Prager Dilation Angle (ψ)	0

In addition to the homogeneous Model A, a second model representing cortical bone microstructure was developed (Model B). A layered structure consisting of two distinctly different materials was constructed, one a stiff and strong material, the second a compliant and weak material. This composite model was a phenomenological representation of the complex microstructure of cortical bone. The significant differences in layer stiffness are representative of the individual properties of the main constituents of cortical bone, namely collagen and hydroxyapatite. The layer thicknesses (Material 1: 0.2mm and Material 2: 0.4mm) were based upon experimental measurements of cortical bone (Rho et al. 1998; Gong et al. (1964); Kutz (2003)). Both materials were modelled as isotropic elasto-plastic, again using Drucker-Prager plasticity. The layers of Model B were orientated to represent osteon alignment for transverse and longitudinal pullout simulations, as shown in Figure 6.2(ii) and (iii), respectively.



Feerick and McGarry *J Biomech*, Volume 45, Issue 9, 1 June 2012, Pages 1666–1672

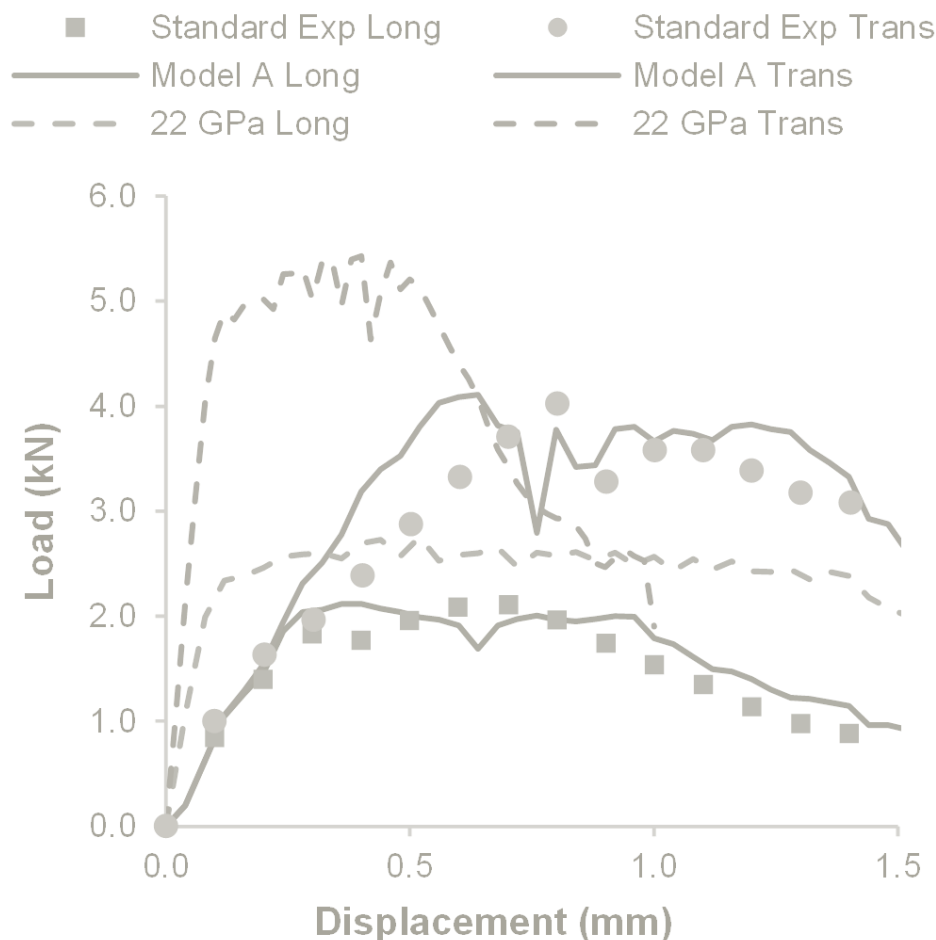
Figure 6.2 Boundary conditions: (i) Model A; (ii) Model B transverse osteon orientation; (iii) Model B longitudinal osteon orientation

Boundary conditions applied to all models are highlighted in Figure 6.2. Hard surface to surface contact was included between the screw threads and bone, with a coefficient of friction of 0.3 (Viceconti et al. (2004)). No significant changes were computed when frictionless contact was assumed between the screw surface and the bone.

A damage process was incorporated in the models to simulate crack initiation and propagation. A critical plastic strain was calibrated for each material by conducting extensive parameter studies, until simulated damage initiation patterns agreed with experimental observations. A critical plastic displacement was also calibrated for each material. Once an element was deformed by the critical plastic displacement it was removed from the mesh facilitating crack propagation in the model (Further detail provided in Chapter 3) (Abaqus (2009)).

6.3 Results

Initial simulations for Model A were conducted using a modulus of 22 GPa as this had previously been reported experimentally for cortical bone. Results of the 22 GPa modulus are summarised in Figure 6.3. A modulus of 22 GPa proved too stiff when compared to experimental results for screw pullout for a transverse and longitudinal simulation. The modulus was incrementally reduced until a modulus of 2.2 GPa replicated the slope of the experimental data for both longitudinal and transverse simulations (Figure 6.3).



Feerick and McGarry *J Biomech*, Volume 45, Issue 9, 1 June 2012, Pages 1666–1672

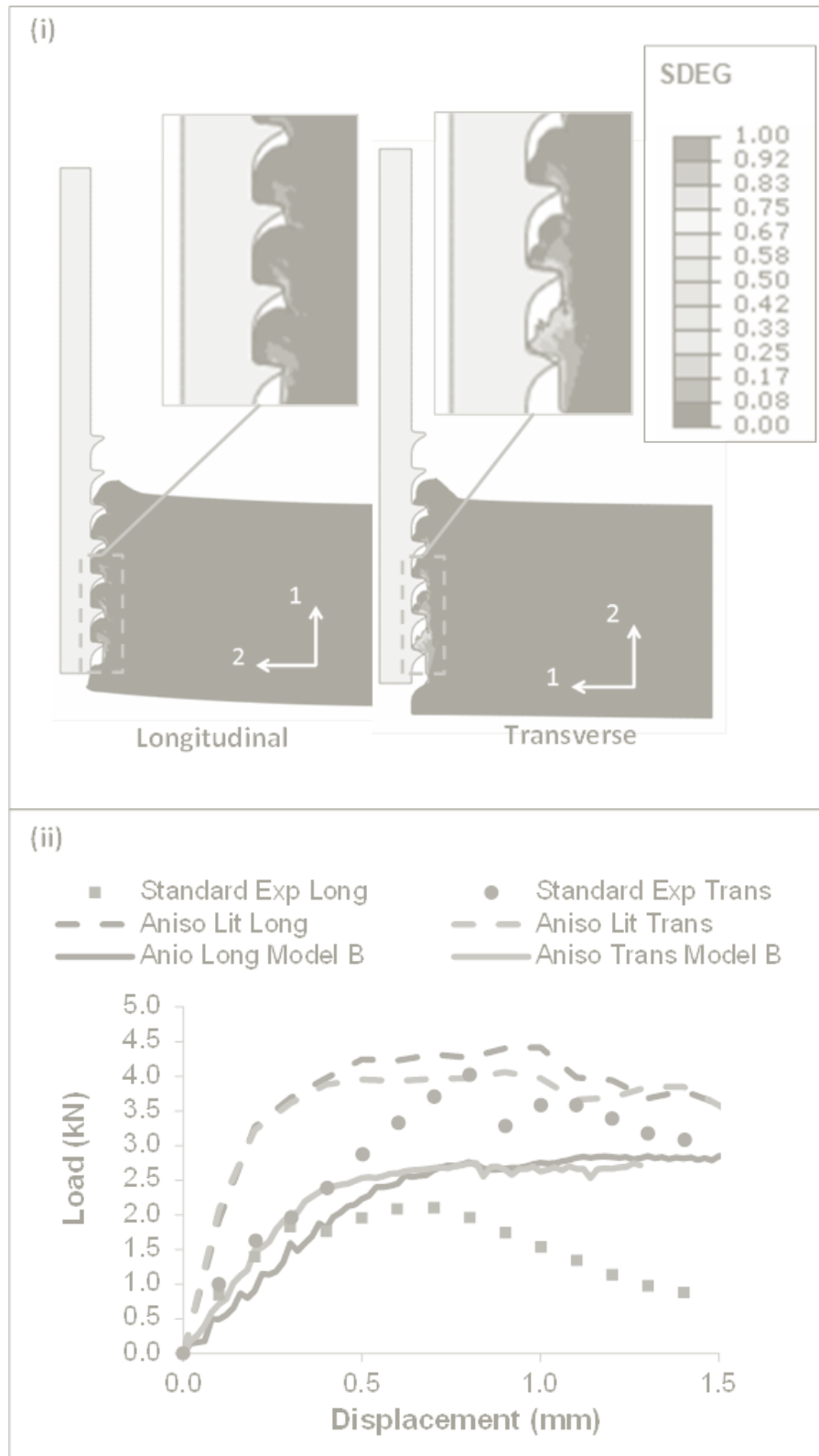
Figure 6.3 Force displacement curves for: (i) Experimental standard longitudinal and transverse pullout tests, (ii) Computational results for modulus of 22 GPa (iii) Computational results for modulus of 2.2 GPa.

The use of a homogeneous anisotropic material model was investigated for the simulation of the experimentally observed peak loads and crack patterns. Simulations were conducted using commonly reported values for cortical bone from the literature (Reilly and Burstein (1975); Rho et al. (1998)). Simulations were also conducted using the material properties calibrated for Model B. Despite the significantly different material properties assigned in the 1 and 2 directions, the same crack patterns were predicted for both a longitudinal and transverse simulation, as shown by the stiffness degradation contour plots of Figure 6.4(i). Increasing the difference between the material properties (using Model B parameters, decreasing E_2 to 800 MPa and reducing E_{12} to 500 MPa, shown in Table 6.2) failed to alter this pattern. Additionally, looking at the load displacement curves of Figure 6.4(ii), we see that the same peak loads were predicted for longitudinal and transverse

simulations for both sets of material properties, in contrast to the significantly different pullout forces observed experimentally in Chapter 5 for longitudinal and transverse pullout tests. From these results, the necessity for a phenomenological representation of the cortical bone microstructure was apparent; in order to capture the key differences between longitudinal and transverse pullout forces and failure mechanisms.

Table 6.2 Anisotropic Material Properties

	Reilly et al.	Model B Parameters
E_1 (GPa)	22.1	22.1
E_2 (GPa)	10.1	0.8
G_{12} (GPa)	3.3	0.5
ν	0.3	0.3
σ_{y1} (MPa)	200	200
σ_{y2} (MPa)	100	100
σ_{y12} (MPa)	50	50



Feerick and McGarry J Biomech, Volume 45, Issue 9, 1 June 2012, Pages 1666–1672

Figure 6.4 (i) Stiffness degradation for longitudinal and transverse pullout simulations with bands of stiffness degradation localised vertically upwards from screw thread tips; (ii) Force displacement curves for: (a) Experimental standard longitudinal and transverse pullout tests, (b) Computational force displacement data for anisotropic material properties from literature (c) Computational force displacement data for Model B material properties.

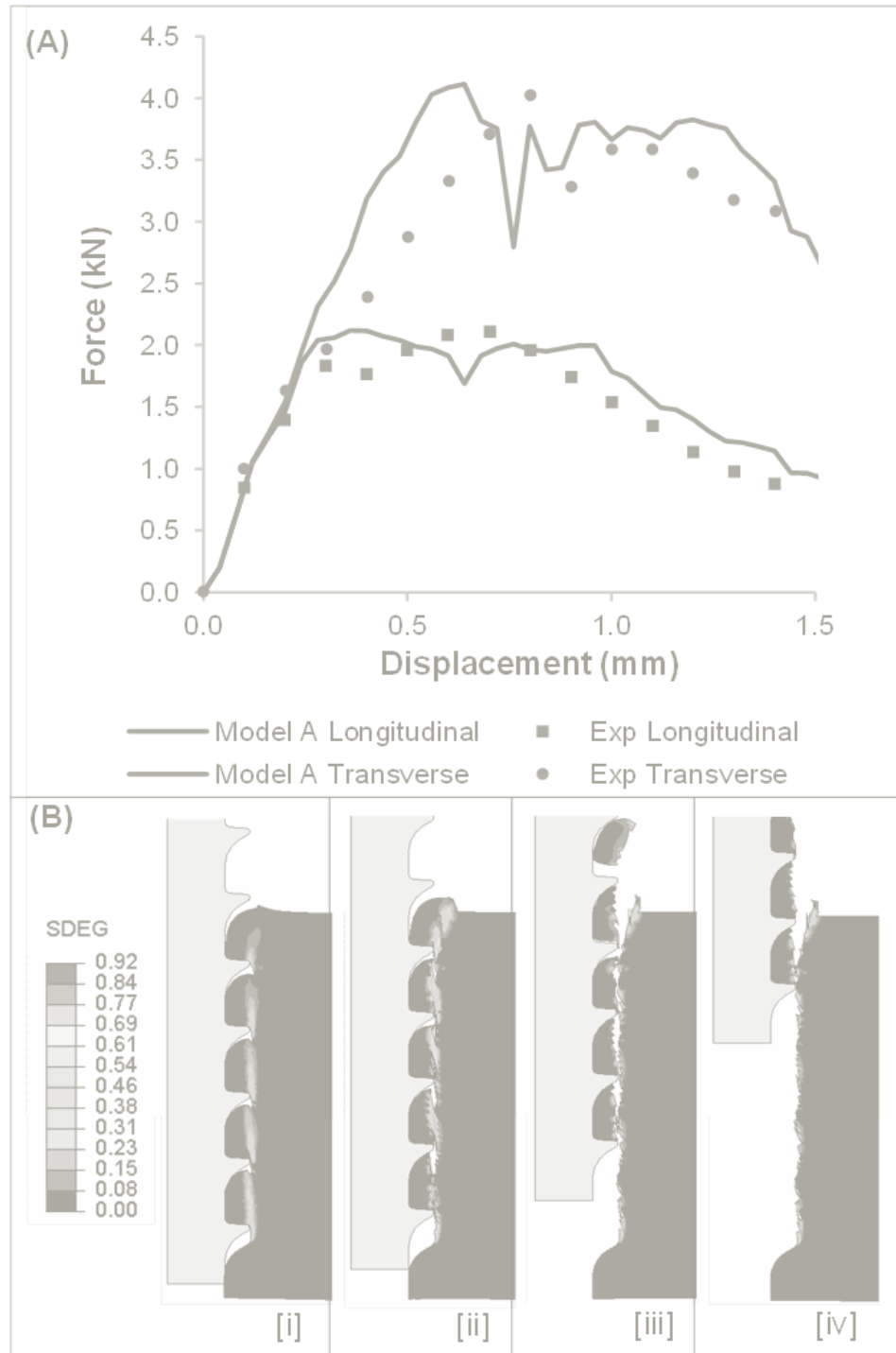
Calibrated model parameters are summarised in Table 6.3. Force deformation curves computed using the homogeneous Model A, are compared to standard and SPDV experimental results in Figure 6.5A. Firstly, it should be noted that an excellent correlation was obtained with the longitudinal results (blue curve) for a shear yield stress of 50MPa (Table 6.3). A peak force of 2 kN was computed at 0.4mm and by calibrating the damage initiation and evolution variables, a loading plateau and load reduction curve similar to the experimental data was obtained. Crack initiation and propagation was predicted vertically upwards from the screw thread tips (Figure 6.5B(i-iv)), similar to experiments of Chapter 5. The bone between the screw threads detached as the screw was displaced upwards leaving a smoothed failure surface with no thread definition. Next, focusing on the transverse pullout data, also Figure 6.5A (red curve), it should be noted the shear yield stress of Model A was increased to 80MPa (Table 6.3), in order to capture the higher pullout forces recorded experimentally. Critically, however, the damage mechanism predicted by this homogeneous model was identical to that shown in Figure 6.5B, simulating vertical cracks. This does not resemble the horizontal crack propagation observed experimentally for transverse pullout tests (Chapter 5 Figure 5.17).

Table 6.3 Calibrated model parameters for Model A and B

	Model A		Model B	
			Material 1	Material 2
Ti Screw Elastic Modulus (GPa)	110			
Cortical Bone Elastic Modulus (MPa)	2200		22100	800
Drucker Prager Hardening	Long	Trans	800	50
Shear Yield Stress (MPa)	50	80		
Damage Initiation	0.025		0.04	0.025
Damage Evolution (mm)	2.0		0.8	0.3

Over 200 simulations were conducted to calibrate a unique set of elasto-plastic and damage material properties for Model B (Table 6.3). This property set satisfied three

distinct criteria for replicating experimental tests: (i) Slope of the loading curve prior to the peak load; (ii) Peak (failure) forces; (iii) Crack propagation patterns.

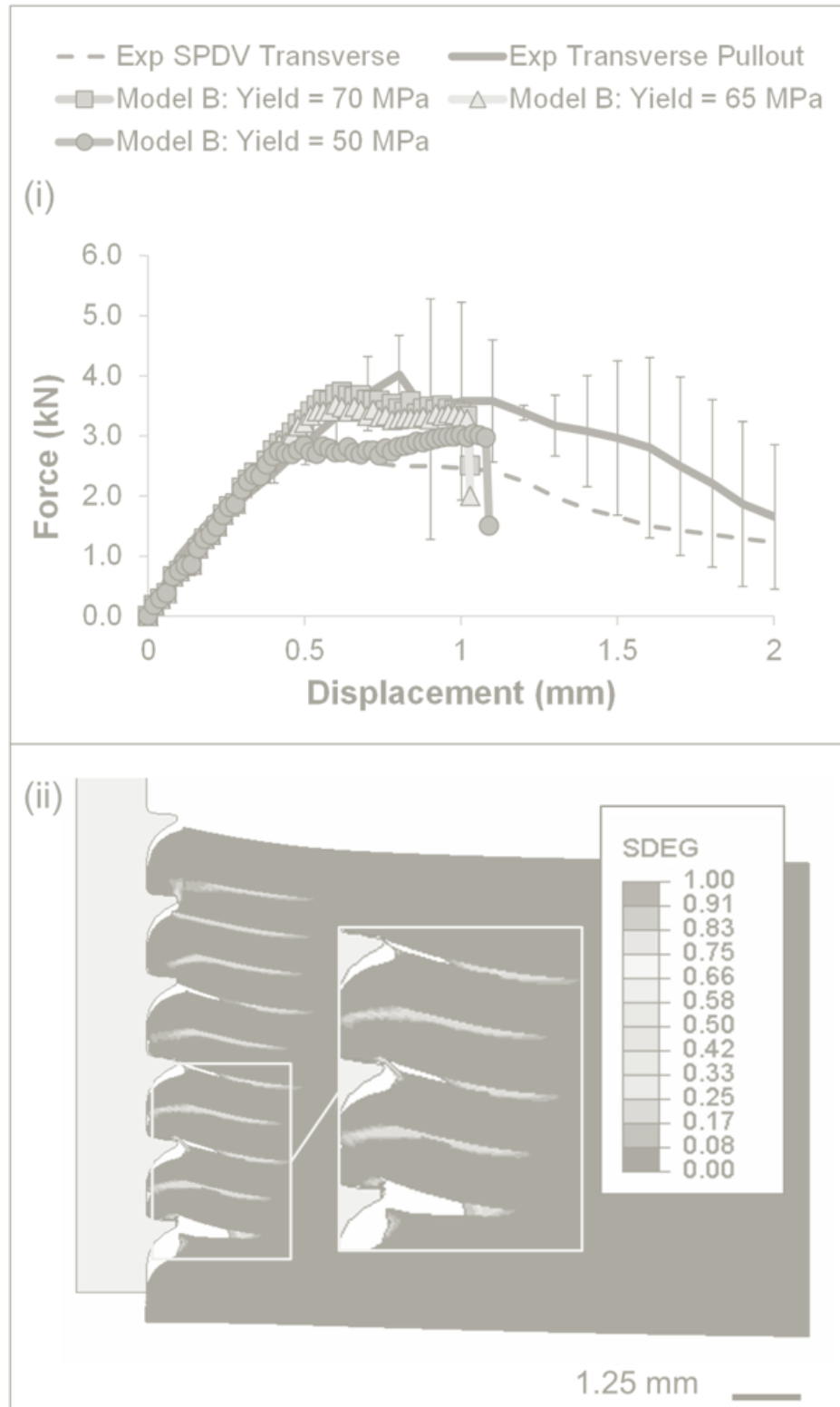


Feerick and McGarry *J Biomech*, Volume 45, Issue 9, 1 June 2012, Pages 1666–1672

Figure 6.5 (A) Model A: Drucker-Prager predicted force displacement curve versus average experimental load data for longitudinal and transverse orientations; (B) Contour plot of material stiffness degradation factor (SDEG) with damage evolution at four time points; vertical crack propagation failure mode computed for both longitudinal and transverse pullout simulations.

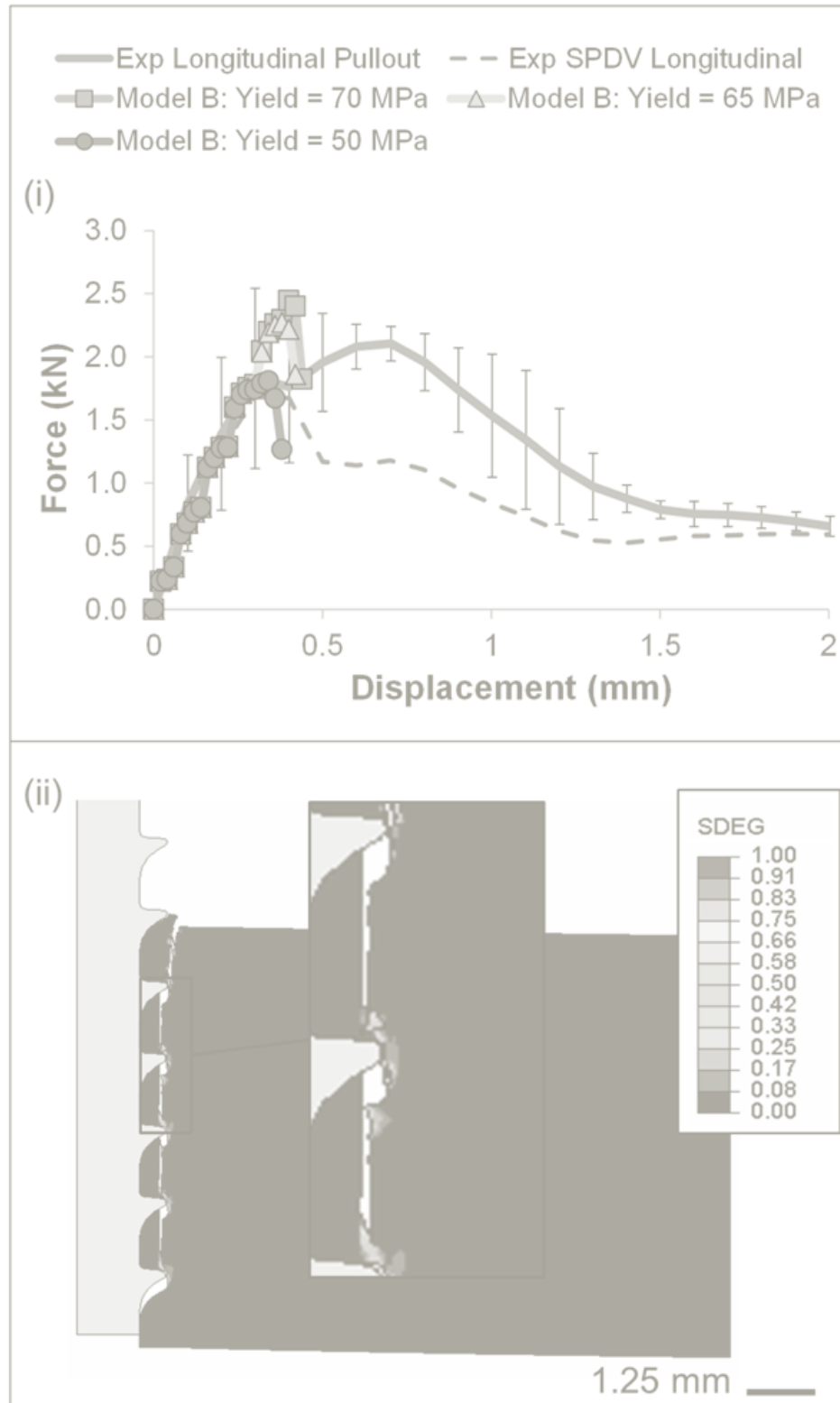
Model B predicted horizontal crack propagation and extensive regions of material damage for transverse pullout simulations, as shown in Figure 6.6(ii). This pattern of damage corresponds closely to that observed experimentally (Chapter 5). Material properties were calibrated so that the predicted force displacement curve matched experimental measurement for the transverse test, with a peak pullout force of 3.52kN (Figure 6.6(i)). When identical material properties were used to simulate the longitudinal pullout test, computed peak forces were on average 36.1% lower than corresponding transverse simulations. This agreed with experimental data where a 47.5% reduction was observed. Most importantly, the mode of failure predicted for a longitudinal simulation (Figure 6.7(ii)) was also similar to experimental observations (Chapter 5), with vertical crack prediction.

The load data, produced by Model B, did not match the post-peak experimentally recorded data as closely as Model A, as the plastic displacement prior to element deletion was much lower. Increasing plastic displacement prior to deletion in Model B resulted in higher stress localisation at the screw threads for transverse pullout, thereby altering the path of element deletion so that horizontal cracks were no longer predicted.



Feerick and McGarry *J Biomech*, Volume 45, Issue 9, 1 June 2012, Pages 1666–1672

Figure 6.6 Model B composite pullout simulation: (i) Transverse pullout force data compared to experimental force data with Model B simulations for increasing matrix yield stress (50 MPa, 65 MPa, 70 MPa); (ii) Contour plot of stiffness degradation factor with failure progression for transverse pullout



Feerick and McGarry *J Biomech*, Volume 45, Issue 9, 1 June 2012, Pages 1666–1672

Figure 6.7 Model B composite pullout simulation: (i) Longitudinal pullout load data compared to experimental load data with Model B simulations for increasing matrix yield stress (50 MPa, 65 MPa, 70 MPa); (ii) Contour plot of stiffness degradation with failure progression for longitudinal pullout

6.4 Discussion

This chapter highlights the inability of a homogeneous material model (Model A) to predict the crack propagation patterns during in cortical bone for transverse pullout. Additionally, investigating the use of a homogeneous anisotropic material model failed to predict the alternate failure loads/modes observed experimentally. A biphasic multilayered composite model (Model B) for cortical bone is proposed, which is capable of predicting the alternate failure modes uncovered by experimental tests for both longitudinal and transverse pullout simulations. To the author's knowledge, this composite model is the first inhomogeneous model developed for simulating cortical bone screw pullout. The model accurately predicts experimentally measured pullout forces for both longitudinal and transverse pullout, with the latter being significantly higher.

Developing an inhomogeneous model of cortical bone microstructure incorporating damage demonstrates that crack propagation perpendicular to the screw axis for transverse pullout requires large material deformation prior to screw removal. This resulted in higher pullout forces than those predicted for longitudinal simulations; in which vertical crack propagation occurred between the screw thread tips, with lower deformation of bone during pullout. Simulation of alternate pullout forces and crack propagation patterns, by varying the orientation of layers of Model B, represents a significant advance on previous models of screw pullout. For example, previous studies have modelled pullout from homogeneous isotropic materials without damage prediction as a representation of bone (Zhang et al. (2004); Wirth et al. (2010)). A study by Chatzistergos et al. (2010) modelled screw pullout using a homogeneous material model with cohesive zone surfaces applied along predefined paths. Thus, these previous models are not capable of predicting the alternate crack patterns and pullout forces determined by osteon alignment relative to the screw axis.

Homogeneous material models have been used for cortical bone (Mercer et al. (2006); Mullins et al. (2009)). However, in the present chapter we highlight the deficiency of homogeneous isotropic damage modelling of cortical bone for screw pullout. An inhomogeneous, computational unit cell model highlights the necessity

of accounting for material orientation in large scale models as the effects are not negligible (Mullins et al. (2007)). Use of XFEM has been reported for 2D models of cortical bone, incorporating a representation of the microstructure of cortical bone. These models report the altered trajectories of crack propagation depending on osteon alignment and cement lines during cortical bone fracture (Budyn and Hoc (2010); Abdel-Wahab et al. (2012)). Without incorporating detailed geometries of the microstructure of cortical bone, the present chapter demonstrates that a phenomenological representation of the cortical bone microstructure is sufficient to capture the key differences between longitudinal and transverse pullout failure mechanisms, namely increased pullout force and horizontal crack propagation for transverse pullout.

The findings of the present chapter are relevant to the design and clinical implantation of fracture fixation devices (Gaines Jr 2000; Kwon et al. 2002; Barber et al. 2008; Cuny et al. 2008). Of particular relevance are devices, such as polyaxial locking plates, where screw insertion angle can be selected during surgery (Wilkins et al. (2008); Königshausen et al. (2012)). Screw pullout is a commonly reported failure mode for locking plates (Owsley et al. 2008). For the first time, the present chapter models the relationship between osteon alignment, crack patterns and failure force for cortical bone screw pullout. These findings will provide a useful design paradigm for application specific fracture fixation devices, offering a better understanding of potential failure mechanisms. Using these computational and experimental (Chapter 5) techniques, device designers can determine precise guidelines for surgeons regarding screw orientation, screw thread design selection, and spacing of screws. The importance of screw spacing was highlighted in Chapter 5 due to the alternate crack propagation paths observed for transverse and longitudinal pullout. During transverse pullout, significant crack propagation was observed perpendicular to the screw axis. Commercially available locking plates contain a large number of screw insertion points, providing the surgeon with several options for screw placement (Smith et al. (2007)). Placing screws too closely together may lead to uniting of cracks and extensive regions of bone damage, adding significant complications to revision surgery. Additionally, the techniques presented in this chapter provide a powerful design tool for the investigation of new materials and screw geometries (Goldhahn et al. (2006); Yáñez et al. (2010)).

Limitations of the microstructure Model B have been identified. Firstly, while the model provides an excellent match up to peak load, there is a sudden reduction in load post peak, in contrast with the slower force reduction observed experimentally. Secondly, a 2D axisymmetric representation of 3D helical screw geometry is used. 3D simulation of cortical bone fracture, using the phenomenological model developed in the current chapter, was not possible due to excessive computational demand. Therefore, an alternate computational modelling methodology is proposed in Chapter 7 that is computationally viable for 3D simulations.

In conclusion, Model B, developed in the current chapter, captures the damage mechanisms and failure modes of cortical bone during screw pullout, as observed experimentally in Chapter 5. Additionally, the calibrated Model B is capable of predicting both the failure modes and peak loads for longitudinal and transverse pullout simulations. This provides a useful paradigm that can be used to evaluate screw thread design for application specific fracture fixation.

6.5 References

- Abaqus, 2009. Abaqus Users Manual 6.9, Dassault Systemes Simulia Corp., Providence
- Abdel-Wahab, A. A., Maligno, A. R. and Silberschmidt, V. V., 2012. Micro-scale modelling of bovine cortical bone fracture: Analysis of crack propagation and microstructure using X-FEM. *Computational Materials Science* 52, 128-135.
- Barber, F. A., Herbert, M. A., Beavis, R. C. and Barrera Oro, F., 2008. Suture Anchor Materials, Eyelets, and Designs: Update 2008. *Arthroscopy: The Journal of Arthroscopic & Related Surgery* 24, 859-867.
- Budyn, É. and Hoc, T., 2010. Analysis of micro fracture in human Haversian cortical bone under transverse tension using extended physical imaging. *International Journal for Numerical Methods in Engineering* 82, 940-965.
- Derikx, L. C., Vis, R., Meinders, T., Verdonschot, N. and Tanck, E., 2011. Implementation of asymmetric yielding in case-specific finite element models improves the prediction of femoral fractures. *Computer Methods in Biomechanics and Biomedical Engineering* 14, 183-193.
- Drucker, D. and Prager, W., 1952. Soil Mechanics and Plastic Analysis or Limit Design. *Quarterly of applied mathematics* 10, 157.
- Goldhahn, J., Reinhold, M., Stauber, M., Knop, C., Frei, R., Schneider, E. and Linke, B., 2006. Improved anchorage in osteoporotic vertebrae with new implant designs. *Journal of Orthopaedic Research* 24, 917-925.
- Gong, J. K., Arnold, J. S. and Cohn, S. H., 1964. Composition of trabecular and cortical bone. *The Anatomical Record* 149, 325-331.
- Königshausen, M., Kübler, L., Godry, H., Citak, M., Schildhauer, T. A. and Seybold, D., 2012. Clinical outcome and complications using a polyaxial locking plate in the treatment of displaced proximal humerus fractures. A reliable system? *Injury* 43, 223-231.
- Kutz, M., 2003. *Standard Handbook of Biomedical Engineering and Design*, McGraw-Hill. 8.1-8.23.
- Mercer, C., He, M. Y., Wang, R. and Evans, A. G., 2006. Mechanisms governing the inelastic deformation of cortical bone and application to trabecular bone. *Acta Biomaterialia* 2, 59-68.
- Mullins, L. P., Bruzzi, M. S. and McHugh, P. E., 2009. Calibration of a constitutive model for the post-yield behaviour of cortical bone. *Journal of the Mechanical Behavior of Biomedical Materials* 2, 460-470.
- Mullins, L. P., McGarry, J. P., Bruzzi, M. S. and McHugh, P. E., 2007. Micromechanical modelling of cortical bone. *Computer Methods in Biomechanics and Biomedical Engineering* 10, 159-169.
- Reilly, D. T. and Burstein, A. H., 1975. The elastic and ultimate properties of compact bone tissue. *Journal of Biomechanics* 8, 393-396, IN9-IN11, 397-405.
- Rho, J.-Y., Kuhn-Spearing, L. and Zioupos, P., 1998. Mechanical properties and the hierarchical structure of bone. *Medical Engineering & Physics* 20, 92-102.
- Smith, W. R., Ziran, B. H., Anglen, J. O. and Stahel, P. F., 2007. Locking plates: tips and tricks. *The Journal of Bone and Joint Surgery (American)* 89, 2298-2307.
- Viceconti, M., Ricci, S., Pancanti, A. and Cappello, A., 2004. Numerical model to predict the longterm mechanical stability of cementless orthopaedic implants. *Med Biol Eng Comput* 42, 747-753.

- Wilkins, K. J., Curtiss, S. and Lee, M. A., 2008. Polyaxial locking plate fixation in distal femur fractures: a biomechanical comparison. *Journal of Orthopaedic Trauma* 22, 624.
- Wirth, A., Mueller, T., Vereecken, W., Flaig, C., Arbenz, P., Müller, R. and van Lenthe, G., 2010. Mechanical competence of bone-implant systems can accurately be determined by image-based micro-finite element analyses. *Archive of Applied Mechanics* 80, 513-525.
- Yáñez, A., Carta, J. A. and Garcés, G., 2010. Biomechanical evaluation of a new system to improve screw fixation in osteoporotic bones. *Medical Engineering & Physics* 32, 532-541.
- Zhang, Q. H., Tan, S. H. and Chou, S. M., 2004. Investigation of fixation screw pull-out strength on human spine. *Journal of Biomechanics* 37, 479-485.

6.6 Appendix 6A: Model B Calibration

Content Removed Due to Copyright

Content Removed Due to Copyright

Chapter 7

Anisotropic Mode Dependent Damage of Cortical Bone using the Extended Finite Element Method (XFEM)

Abstract

Anisotropic damage initiation criteria were developed for extended finite element method (XFEM) prediction of crack initiation and propagation in cortical bone. This anisotropic damage model was shown to accurately predict the dependence of crack propagation patterns and fracture toughness on mode mixity and on osteon orientations, as observed experimentally. Three initiation criteria were developed to define crack trajectories relative to osteon orientations and maximum principal stress direction for single and mixed mode fracture. Alternate failure strengths for tensile and compressive loading were defined to simulate the asymmetric failure of cortical bone. The dependence of cortical bone elasticity and failure properties on osteon orientation is analogous to the dependence of composite properties on fibre orientation. Hence, two of the criteria developed in the present chapter were based upon the Hashin damage criterion, commonly implemented in composite damage modelling. The third criterion developed was defined in terms of the maximum principal stress. This criterion initiated off axis crack growth perpendicular to the direction of the maximum principal stress. This unique set of calibrated parameters accurately predicted; (i) the relationship between fracture energy and osteon alignment, (ii) the alternate crack patterns for both varying osteon orientations and loading angle. Application of the developed anisotropic damage models to cortical bone screw pullout highlights the potential application for orthopaedic device design evaluation.

7.1 Introduction

Several studies have investigated cortical bone fracture toughness and crack trajectory as a function of microstructural alignment of osteons. (Norman et al. (1996); Zimmermann et al. (2009); Zimmermann et al. (2010); An et al. (2011); Olvera et al. (2012)). The dependence of osteon orientation on screw pullout force

and crack propagation during screw pullout has been demonstrated in Chapter 5. In Chapter 6, in order to simulate crack patterns and pullout force, a phenomenological representation of cortical bone was employed. Chapter 6 implemented a process of element deletion to simulate crack growth in computational models that was mesh dependent and as a result required mesh densities that were not computationally viable for 3D simulations. Other computational studies have developed geometric representations of the microstructure of cortical bone to simulate the fracture and establish crack trajectories (Budyn and Hoc (2010); Abdel-Wahab et al. (2012)). Again, upscaling these detailed microstructural geometries, in macroscale simulations of fracture, would be computationally unfeasible. The present chapter attempts to use anisotropic damage initiation criteria, in conjunction with the XFEM method, to model cortical bone fracture at a lower computational expense.

XFEM is a method developed for computationally modelling crack initiation and propagation without the need for adaptive remeshing (Melenk and Babuška (1996); Sukumar et al. (2004)). Unlike cohesive zone modelling, in which a crack path is predefined, XFEM can be used to predict crack initiation and propagation along an arbitrary, solution dependent path (Abaqus (2012)). A process of damage initiation and evolution are implemented to simulate fracture opening. Damage initiation is predicted according to a defined failure criterion. Once a crack initiates, for a particular element, it is split into two. The fragments of the split element are free to displace independently of each other, once the defined fracture energy is exceeded. Contact interactions can be applied to the newly exposed surfaces, following crack propagation, to prevent non-physical overclosure of elements that may come into contact.

The objective of the present chapter is to develop anisotropic elasticity material models with anisotropic damage initiation failure criterion. Implementation of these failure criteria, in conjunction with XFEM, is used to model mixed mode fracture of cortical bone. Screw-pullout simulations are also presented, demonstrating that anisotropic damage criteria can be used to compute complex fracture patterns in cortical bone at the macroscale.

7.2 Materials & Methods

7.2.1 Cortical Bone Failure Criteria

Three failure criteria are defined for cortical bone (equations 7.1-7.3), with a specific crack direction being defined for each criterion, as indicated in Figure 7.1(i-iii). A material orientation was assigned to the model geometries to represent fibre (osteon) direction (Figure 7.1(i)). As indicated in equations 7.1-7.3, once any of the failure criteria ($\bar{\sigma}_f, \bar{\sigma}_m, \bar{\sigma}_p$) reaches a value of 1, damage is initiated for that criterion. Cortical bone microstructure has previously been compared to a composite consisting of a fibre and matrix (Rho et al. (1998)). The dependence of cortical bone elasticity and failure properties on osteon orientation is analogous to the dependence of composite properties on fibre orientation. Hence, failure criteria 1&2 are based upon Hashin damage (Hashin (1980)), a commonly reported damage criterion for composite failure (Matzenmiller et al. (1995); Lapczyk and Hurtado (2007)). Failure criterion 1 (fibre failure $\bar{\sigma}_f$) is defined in terms of the axial σ_{ff} and shear $\sigma_{f\tau}$ fibre strengths relative to σ_{11} and σ_{12} (equation 7.1). When failure criterion 1 is initiated, crack growth occurs perpendicular to the osteon direction (Figure 7.1(i)). Failure criterion 2 (matrix failure $\bar{\sigma}_m$) is defined in terms of the axial σ_{mm} and shear $\sigma_{m\tau}$ matrix strengths relative to σ_{22} and σ_{12} (equation 7.2). When failure criterion 2 is initiated, crack growth occurs parallel to the osteon direction (Figure 7.1(ii)). To account for off axis crack prediction a third failure criterion ($\bar{\sigma}_p$) was defined by equation 7.3. The angle of the maximum principal stress relative to the fibre direction (θ) is used to define an effective strength based upon the fibre (σ_{ff}) and matrix (σ_{mm}) strengths. When the maximum principal stress (σ_p) exceeds the effective strength, failure criterion 3 initiates and crack growth occurs perpendicular to the maximum principal stress direction, as shown in Figure 7.1(iii). Cortical bone has previously been shown to exhibit asymmetric failure strengths (Reilly and Burstein (1975)). Therefore, alternate failure strengths were defined for fibre and matrix failures under tension and compression, hence six failure parameters are defined for the anisotropic damage initiation criteria for cortical bone.

$$\text{Failure Criterion 1: } \bar{\sigma}_f = \sqrt{\left(\frac{\sigma_{11}}{\sigma_{ff}}\right)^2 + \left(\frac{\sigma_{12}}{\sigma_{f\tau}}\right)^2} = 1 \quad (7.1)$$

$$\text{Failure Criterion 2: } \bar{\sigma}_m = \sqrt{\left(\frac{\sigma_{22}}{\sigma_{mm}}\right)^2 + \left(\frac{\sigma_{12}}{\sigma_{m\tau}}\right)^2} = 1 \quad (7.2)$$

$$\text{Failure Criterion 3: } \bar{\sigma}_p = \frac{\sigma_p}{\sqrt{\sigma_{ff}^2 \cos^2 \theta + \sigma_{mm}^2 \sin^2 \theta}} = 1 \quad (7.3)$$

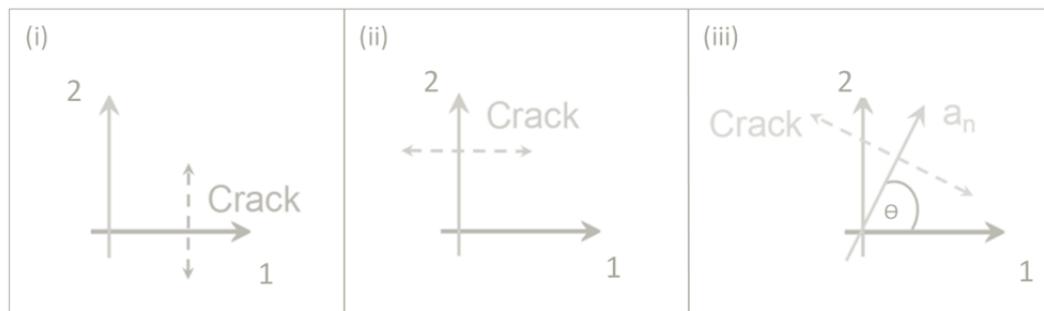
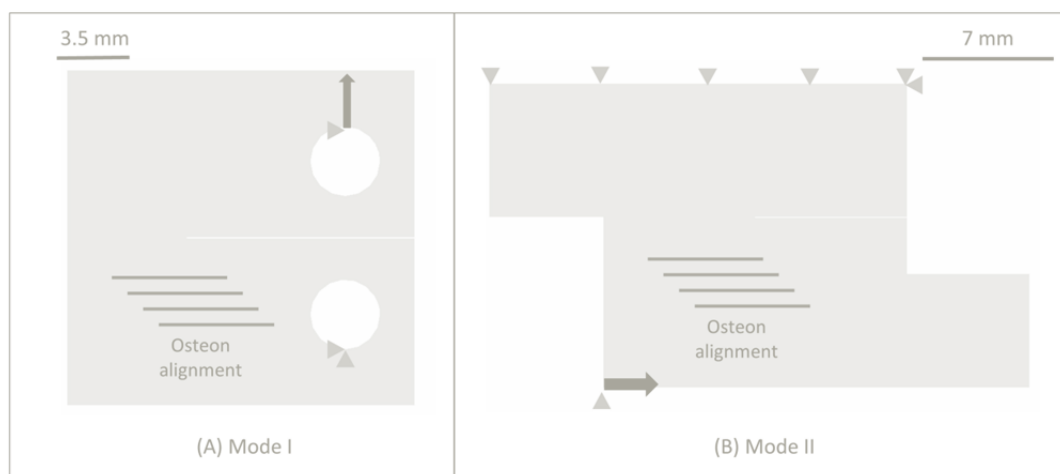


Figure 7.1 Crack trajectories for each failure criteria; (i) Failure criterion 1 crack trajectory: normal to the fibre orientation (direction 1); (ii) Failure criterion 2 crack trajectory: parallel to the fibre orientation (direction 2); (iii) Failure criterion 3 crack trajectory: normal to the maximum principal stress direction (a_n)

The failure criteria defined in equations 7.1-7.3 were implemented using the FORTRAN user sub routine UDMGINI, in conjunction with XFEM, using Abaqus 6.12 Standard for crack propagation modelling. Regions of the mesh in which XFEM fracture modelling was implemented are referred to as enrichment zones. Once damage was initiated, split element fragments were free to displace independently of each other when the defined critical fracture energy was exceeded as outlined in Chapter 3. All simulations were conducted using anisotropic linear elastic material properties. Hard contact was implemented on the newly exposed split element surfaces, to prevent non-physical over closure, with a coefficient of friction of 0.3.

7.2.2 Material Parameter Longitudinal Calibration

The first simulations used to calibrate the anisotropic damage model were those of Norman et al. (1996). The dimensions and boundary conditions shown in Figure 7.2 were based upon those reported by Norman et al. (1996). The latter study reported load displacement data for mode I and mode II tests that were used to partially calibrate the anisotropic elasticity and anisotropic damage parameters. Simulations were conducted using Abaqus 6.12 standard.



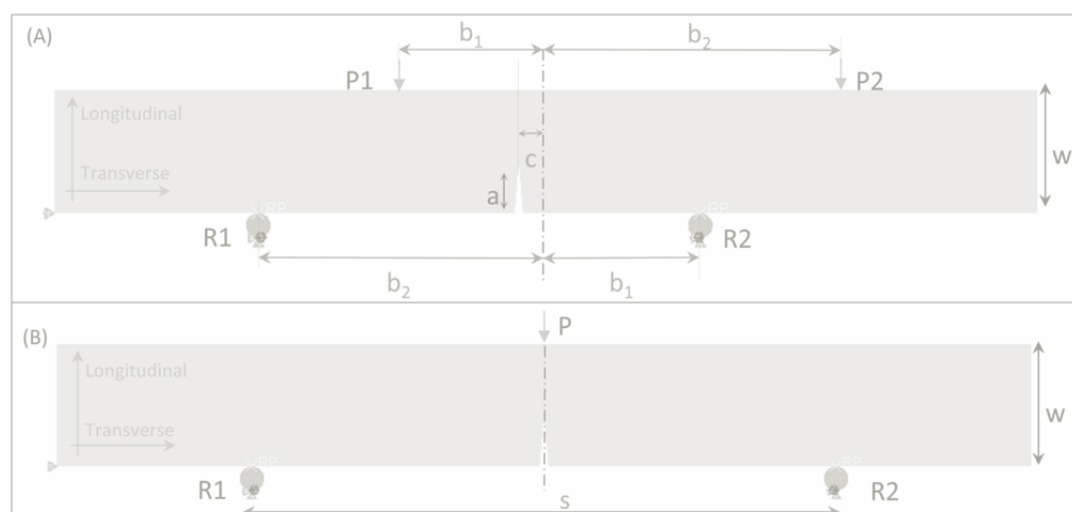
Feerick et al. (2013) *JMBBM*, Article In Press, <http://dx.doi.org/10.1016/j.jmbbm.2012.12.004>

Figure 7.2 (A) Mode I and (B) Mode II boundary conditions for simulations of Norman et al (1996) cortical bone fracture experiments.

7.2.3 Material Parameter Transverse/Longitudinal Calibration

Following the simulation of longitudinal experiments of Norman et al. (1996) experimental tests of Zimmerman et al. (2009) were next simulated to provide a complete calibration and validation of the anisotropic damage initiation criteria. The geometry of the models of Figure 7.3 was based upon the experimental tests performed by Zimmerman et al (summarised in Table 7-1). Mixed mode simulations (phase angles 15° - 90°) were simulated using an asymmetric four point bend test. The boundary conditions applied for the asymmetric four point bend simulations are shown in Figure 7.3(A) (He (2000)). Two rigid supports (R1 & R2) were positioned at the base of sample, while two loading points (P1 & P2) were applied at the top of the sample. A notch located at the centre of the sample represented a pure mode II test. Positioning of the notch by a distance “c” from the centre of the specimen produced a mixed mode test. As the magnitude of “c” increases, the mode mixity

tends towards mode I. Simulations were conducted for longitudinally and transversely orientated cortical bone for mode I (phase 0), mode II (phase 90), phase 15, phase 30 and phase 60. Additionally, pure mode I simulations were conducted using a three point bend test (Figure 7.3B). Material orientations were applied to represent longitudinal and transverse alignment of osteons, as illustrated in Figure 7.3.



Feerick et al. (2013) *JMBBM*, Article In Press, <http://dx.doi.org/10.1016/j.jmbbm.2012.12.004>

Figure 7.3 2D asymmetric four and three point bend tests (A) Asymmetric four point bend test; (B) Three point bend test. The fibre orientation assigned to represent transverse and longitudinal osteon alignment loadings are indicated by the transverse and longitudinal arrows of (A) and (B).

The force data from the simulations was used to calculate the fracture toughness in terms of the strain energy release rate (G) for cortical bone (He (2000); Marsavina and Piski (2010)). The shear force (Q) and the bending moment (M) were determined by the position of the loading (P). The stress intensity factors K_I and K_{II} were calculated according to equations 7.4 & 7.5 for four point bend tests. K_I (equation 7.6) is calculated for a 3 point bend test according to the ASTM standard EI1290-08.

Table 7.1 Geometry of samples associated with Figure 7.3

	(mm)		(mm)		c (mm)
a	2.0	s	16.0	Phase 30	1.10
W	5.0	b1	6.0	Phase 60	0.35
a/w	0.4	b2	12.0	Phase 90	0.00

4Pt Bend:

$$K_I = \frac{6cQ}{W^2} \sqrt{\pi a} F_I \left(\frac{a}{W} \right) \quad (7.4)$$

$$K_{II} = \frac{Q}{\sqrt{W}} \frac{\left(\frac{a}{W} \right)^{\frac{3}{2}}}{\sqrt{1 - \left(\frac{a}{W} \right)}} F_{II} \left(\frac{a}{W} \right) \quad (7.5)$$

where, $Q = R_1 - P_1$; $M = R_1(b_2 + c) - P_1(b_1 + c)$ as shown in Figure 7.3A

3Pt Bend:

$$K_I = \frac{6P}{W} \sqrt{a} \left(\frac{1.99 - \left(\frac{a}{W} \right) \left(1 - \frac{a}{W} \right) \left(2.15 - 3.39 \left(\frac{a}{W} \right) + 2.7 \left(\frac{a}{W} \right)^2 \right)}{\left(1 + 2 \left(\frac{a}{W} \right) \right) \left(1 - \left(\frac{a}{W} \right)^{\frac{3}{2}} \right)} \right) \quad (7.6)$$

where, $Q = 0$; $M = \left(\frac{Ps}{2} \right)$ as shown in Figure 7.3B

F_I and F_{II} were calculated in accordance with He (2000). As the ratio of notch height to sample width (a/W) is 0.4 equations (7.7 & 7.8) are used to define F_I and F_{II} .

$$F_I = 1.122 - 1.121 \left(\frac{a}{W} \right) + 3.740 \left(\frac{a}{W} \right)^2 + 3.873 \left(\frac{a}{W} \right)^3 - 19.05 \left(\frac{a}{W} \right)^4 + 22.55 \left(\frac{a}{W} \right)^5 \quad (7.7)$$

$$F_{II} = 7.264 - 9.37 \left(\frac{a}{W} \right) + 2.74 \left(\frac{a}{W} \right)^2 + 1.87 \left(\frac{a}{W} \right)^3 - 1.04 \left(\frac{a}{W} \right)^4 \quad (7.8)$$

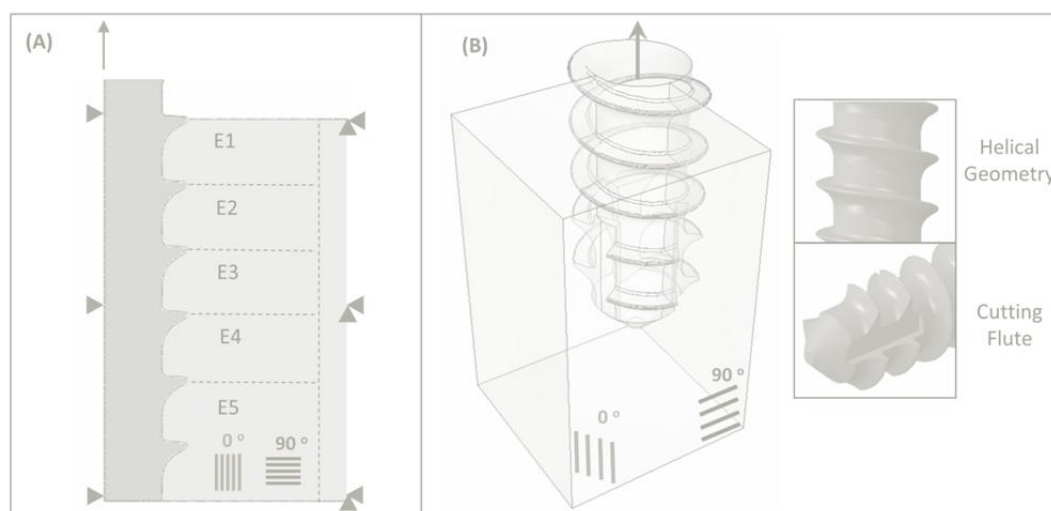
The strain energy release rate (G_c) is calculated according to equation 7.9.

$$G_c = \left(\frac{K^2}{E'} \right) = \left(\frac{K_I^2}{E'_I} + \frac{K_{II}^2}{E'_{II}} \right) \quad (7.9)$$

To replicate the methods of Zimmermann et al. (2009) (plane stress calculations) a single effective modulus ($E' = E'_I = E'_{II}$) was used to calculate G_c in equation 7.9.

7.2.4 XFEM Application: 2D and 3D Screw Pullout

Following calibration of the model using the experimental data of (Norman et al. (1996); Zimmermann et al. (2009)), 2D & 3D simulations were conducted for cortical bone screw pullout. The geometry of the models was taken from the previous experimental and computational studies of screw pullout in Chapters 5 and 6. 3D simulations were conducted to investigate the effect of geometrically complex features, such as the cutting flute and helix of self tapping screws (Figure 7.4B). The geometry and boundary conditions applied to the 2D (35,392 elements) and 3D (183,552 elements) models are illustrated in Figure 7.4. As crack initiation was expected to occur in more than one region of the model, it was necessary to apply multiple enrichment regions between each of the screw threads, as illustrated in Figure 7.4A. 2D simulations were conducted with material orientations to represent longitudinal and transverse screw pullout (Figure 7.4A). 3D simulations were also conducted for varied osteon alignment (Figure 7.4B).



Feerick et al. (2013) *JMBBM*, Article In Press, <http://dx.doi.org/10.1016/j.jmbbm.2012.12.004>

Figure 7.4 2D & 3D screw pullout schematic (A) 2D screw pullout boundary conditions highlighting the material orientations for longitudinal, transverse simulations with multiple enrichment zones (E1-E5); (B) 3D screw pullout to investigate unsymmetrical features including helical geometry and cutting flute.

7.3 Results

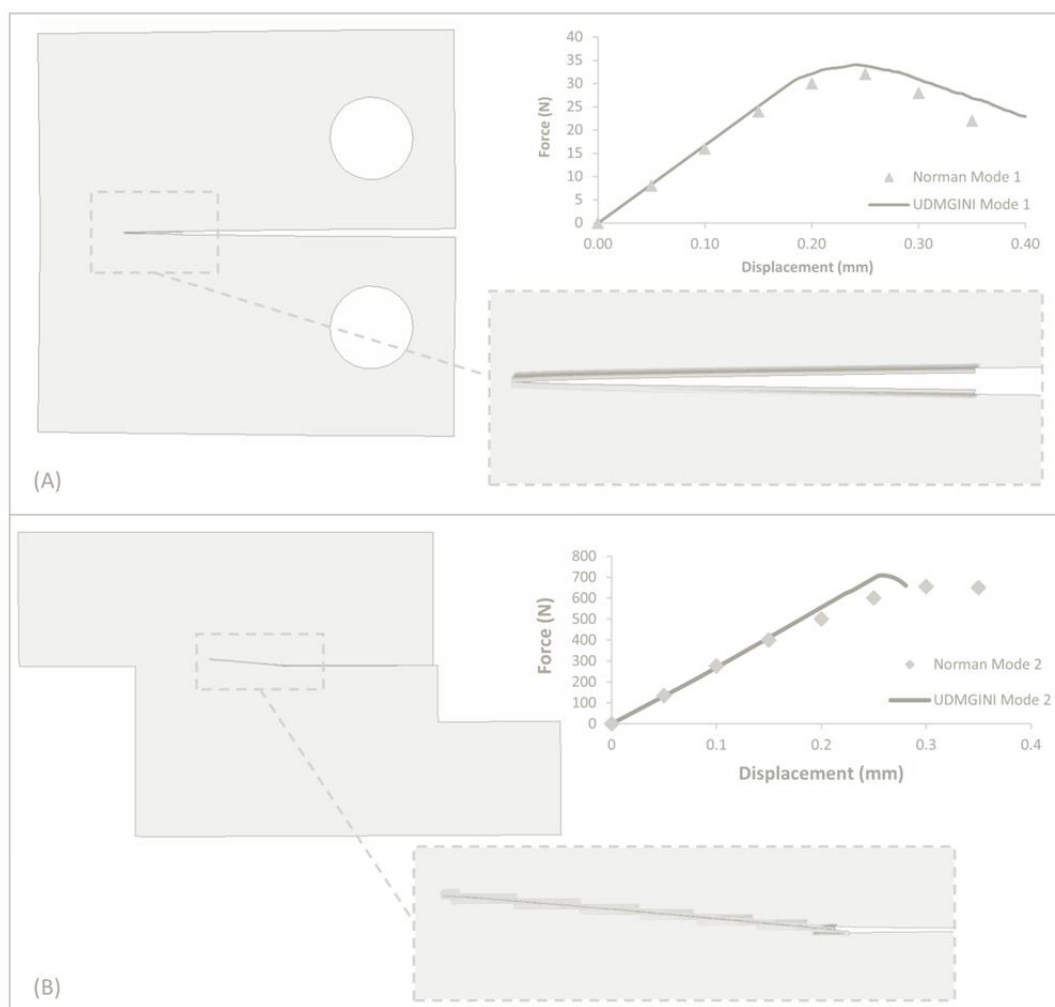
7.3.1 Material Parameter Longitudinal/Transverse Calibration

Cortical bone is a transversely orthotropic material. It was necessary to conduct parametric studies to calibrate the unique set of parameters for anisotropic elasticity

($E_{11}, E_{22}, E_{12}, E_{23}$) and failure strengths (σ_{ff} & σ_{mm} (tensile), σ_{ff} & σ_{mm} (compression), $\sigma_{f\tau}, \sigma_{m\tau}$) for the homogenised representation of cortical bone. The simulation of the experimental studies of Norman et al. (1996) and Zimmermann et al. (2009), provided the validation for the calibration of these parameters. The experimental studies of Norman et al. (1996) focussed on the fracture of longitudinal alignment of cortical bone. Therefore, the critical parameters calibrated from the experimental data of Norman et al. were E_{22} , E_{12} , σ_{mm} (tensile), $\sigma_{f\tau}$ and $\sigma_{m\tau}$. Following an extensive parametric study, a unique set of values for the aforementioned parameters was identified (Table 7.1), so that the mode I and mode II test results of Norman et al. were accurately predicted by the model. The load displacement curve for a mode I compact tension simulation is shown in Figure 7.5A. The anisotropic elasticity properties provided the calibration of the initial slope, with the failure criteria determining the failure force. The damage evolution criteria defined the post peak load curve as unloading occurred with crack propagation. The predicted failure force of 35 N at 0.23 mm displacement was similar to the experimental results of Norman et al. (1996). The predicted crack patterns are illustrated in Figure 7.5A, parallel to the direction of the osteons, with crack propagation clearly visible with the opening of the crack surface. The predicted failure mode and load displacement curve for a mode II simulation are shown in Figure 7.5B. Compared to the crack trajectories of a mode I simulation, Figure 7.5B shows a slight deviation of the crack from the osteon direction. The predicted failure force of 700 N was close to the experimentally observed value of 675 N reported by Norman et al.

The experimental testing conducted by Zimmermann et al. (2009) provided the data to complete the identification of a unique parameter set for cortical bone (Table 7.2). The results of a longitudinal cortical bone bend test simulation are shown in Figure 7.6. Mode I failure resulted in vertical crack prediction parallel to the direction of osteon alignment (Figure 7.6A). As shown in Figure 7.6 (A-D), as the phase angle increased from mode I (0°) to mode II (90°), the direction of crack propagation gradually deviated from the osteon direction, so that the mode II crack direction was almost perpendicular to the osteon direction. As cortical bone is strongest in the osteon direction (fibre direction), the predicted fracture toughness (defined in terms of strain energy release rate) increased with increasing phase angle (Figure 7.6E).

The 6 fold increase in computed fracture toughness, from mode I to mode II, strongly correlates with the experimental data of Zimmerman et al., (also shown in Figure 7.6E).

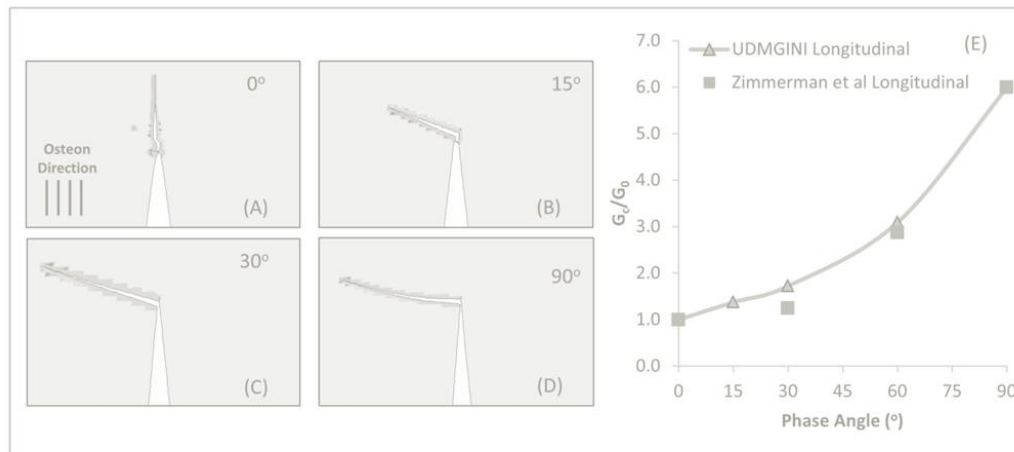


Feerick et al. (2013) *JMBBM*, Article In Press, <http://dx.doi.org/10.1016/j.jmbbm.2012.12.004>

Figure 7.5 (A) Mode I predicted crack pattern and failure load compared to experimental load displacement curve reported by Norman et al (1996), (B) Mode II predicted crack pattern and failure load compared to experimental load displacement curve reported by Norman et al (1996).

As shown in Figure 7.7 (A-D), as the phase angle increased from mode I (0°) to mode II (90°), the direction of crack propagation gradually deviated from perpendicular to the osteon direction, so that the mode II crack direction was parallel to the osteon direction. This computed, mode dependent crack orientation that is extremely similar to that observed by Zimmermann et al. (2009), as shown in Figure 7.7F. In contrast to the longitudinally aligned bend test results (Figure 7.6E), the predicted fracture toughness for a transversely aligned sample decreased with

increasing phase angle (Figure 7.7E). In this case the predicted fracture toughness decreased by a factor of 2.6 from mode I to mode II. This reduction in fracture toughness from mode I to mode II is similar to the experimental results of Zimmerman et al for a transversely aligned specimen, as shown in Figure 7.7E. Finally, it should be noted that a mesh sensitivity study was conducted to assess the mesh independence of XFEM, as summarised in Appendix 7A.

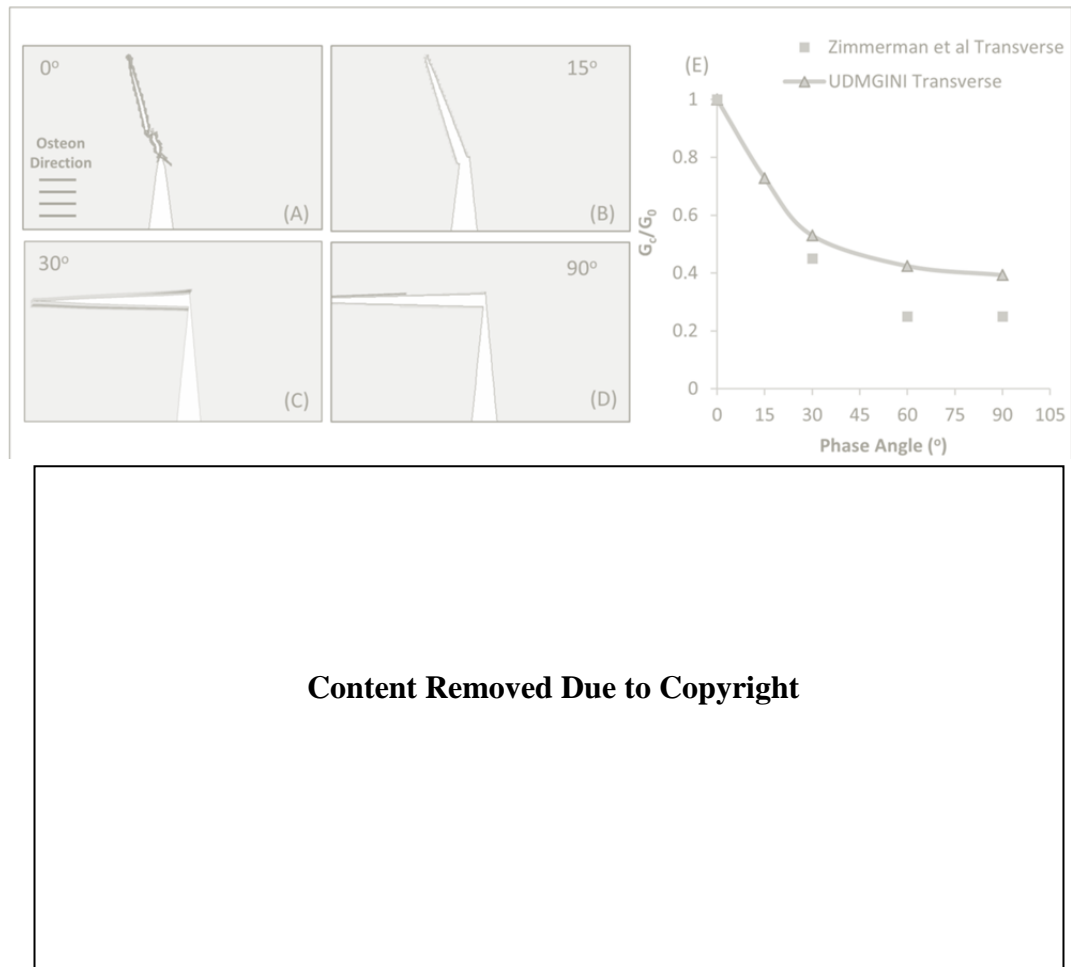


Feerick et al. (2013) JMBBM, Article In Press, <http://dx.doi.org/10.1016/j.jmbbm.2012.12.004>

Figure 7.6 Fracture pattern and strain energy release rate for longitudinally aligned cortical bone for varying phase angles: (A) Mode I (Phase 0°); (B) Phase 15°; (C) Phase 30°; (D) Phase 90° and (E) Normalised predicted strain energy release rates compared to experimental data reported by Zimmerman et al.

Table 7.2 Assigned elasticity, strength and damage evolution parameters

Elastic Modulus	(MPa)	Initiation Criteria Failure Strengths	(MPa)	Evolution Criteria	(J/m²)
E₁₁	4500	σ_{ff} (tensile)	150	Fibre	800
E₂₂	2200	σ_{mm} (tensile)	65	Matrix	300
E₃₃	2200	σ_{ff} (compression)	280		
G₁₂	1000	σ_{mm} (compression)	213		
G₂₃	846	$\sigma_{f\tau}$	84		
v₂₃	0.3	$\sigma_{m\tau}$	132		



Content Removed Due to Copyright

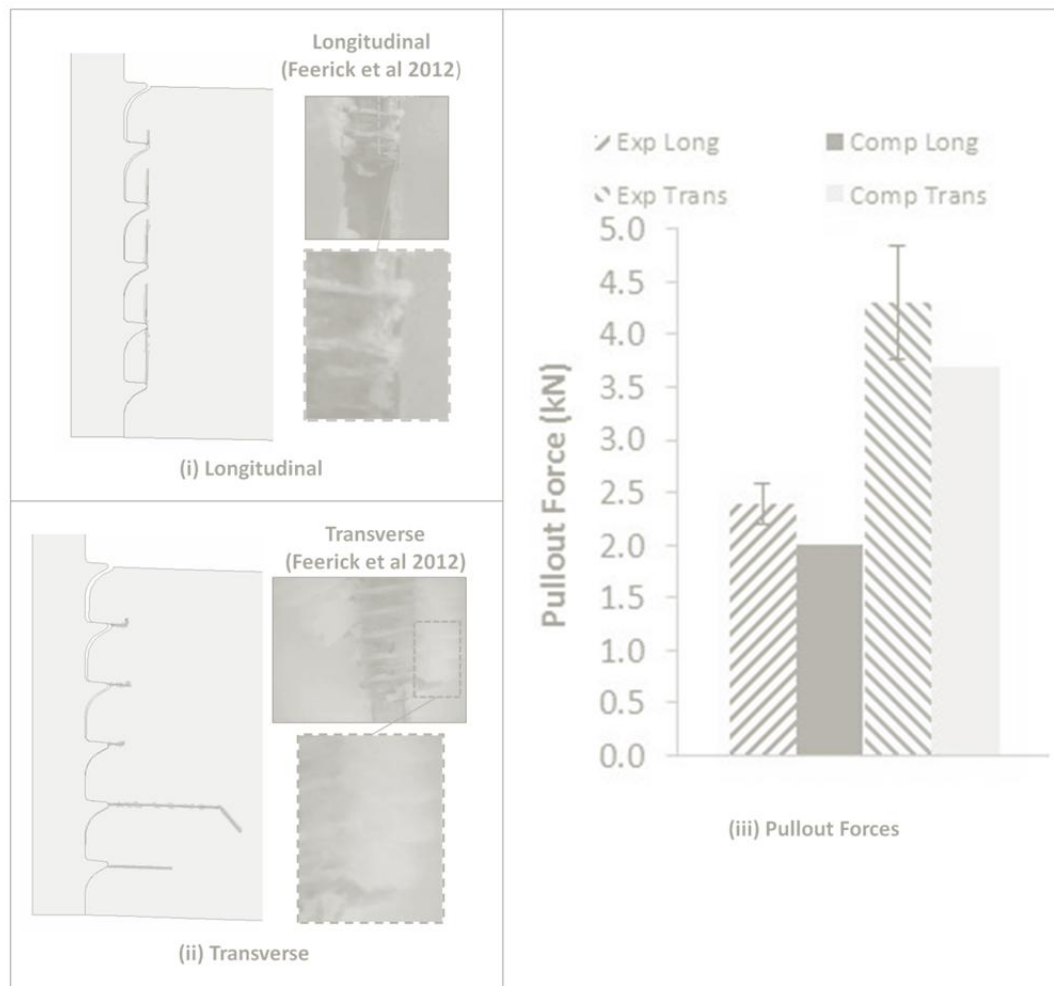
Feerick et al. (2013) *JMBBM*, Article In Press, <http://dx.doi.org/10.1016/j.jmbbm.2012.12.004>

Figure 7.7 Fracture pattern and strain energy release rate for transversely aligned cortical bone for varying phase angles: (A) Mode 1 (Phase 0°); (B) Phase 15°; (C) Phase 30°; (D) Phase 90° and (E) Predicted strain energy release rates normalised against phase 0° strain energy release rate compared to experimental data reported by Zimmerman et al. (2009), (F) Experimental crack pattern images reported for transversely aligned cortical bone fracture by Zimmerman et al (2009) taken from *Elsevier Biomaterials* 30, 5877-5884.

7.3.2 2D application: Screw pullout

Having calibrated the unique property set for anisotropic elasticity and damage initiation criteria for cortical bone (Table 7.2), using the experimental data of Zimmermann et al. (2009) and Norman et al. (1996), the data was then used to simulate screw pullout. The results of a 2D simulation of screw pullout for a longitudinal and transverse screw pullout are summarised in Figure 7.8. Five enrichment regions were applied to the mesh as cracks were expected to initiate in multiple regions, based on previous experimental observations of Chapter 5. Cracks primarily occurred parallel to the direction of the osteons, as shown in Figure 7.8 (i-ii). The predicted patterns of crack propagation replicate those observed

experimentally for longitudinal and transverse screw pullout in Chapter 5. The predicted pullout forces are summarised in Figure 7.8(iii), a significant increase in pullout force for a transverse pullout simulation correlates well with the experimental data of Chapter 5. The importance of subdivision of the finite element mesh into multiple enrichment zones, was found to be critical, for accurate failure prediction of multiple cracks, as discussed in Appendix 7B.

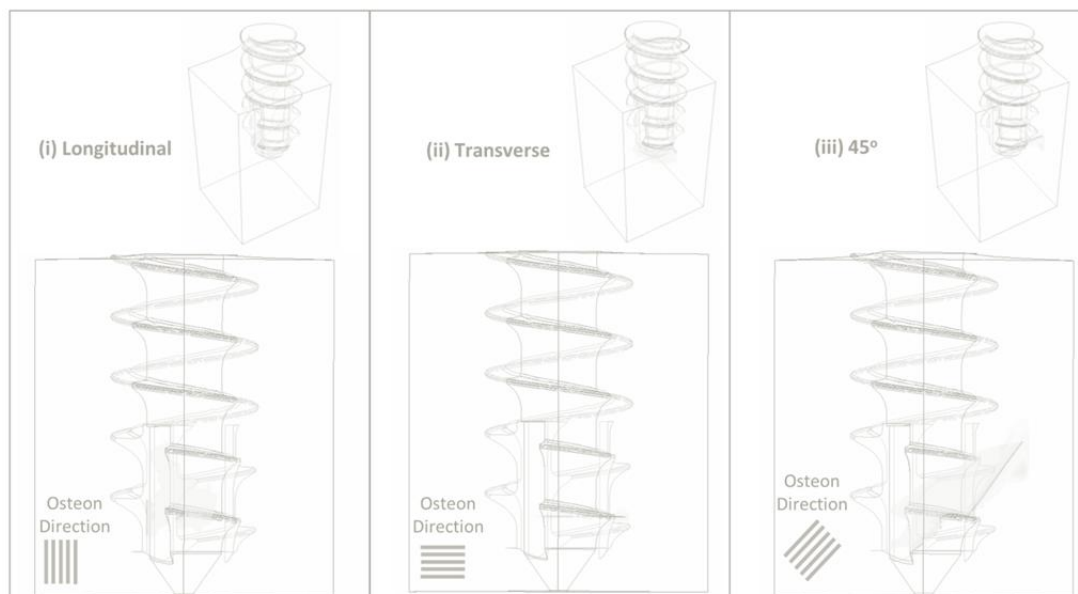


Feerick et al. (2013) *JMBBM*, Article In Press, <http://dx.doi.org/10.1016/j.jmbbm.2012.12.004>

Figure 7.8 Fracture pattern predicted by 2D screw pullout simulation compared to the experimental failure mechanisms observed for (i) Longitudinally and (ii) Transversely orientated cortical bone; (iii) Experimental and computational pullout forces for longitudinal and transverse screw pullout.

The results of a 3D simulation of screw pullout for a longitudinal, transverse and 45 degree screw pullout simulation are summarised in Figure 7.9. Results for the crack directions were generally the same as 2D simulations, all cracks occurred parallel to the direction of the osteons. The location of crack initiation was influenced by the

helical geometry of the screw. For all simulations, cracks were not predicted to initiate in the region of the cutting flute.



Feerick et al. (2013) *JMBBM*, Article In Press, <http://dx.doi.org/10.1016/j.jmbbm.2012.12.004>

Figure 7.9 Crack pattern predicted for 3D screw pullout simulation for (i) longitudinally, (ii) transversely and (iii) 45 degree orientated cortical bone.

7.4 XFEM Application: 3D Proximal Humeral Fracture Fixation

7.4.1 Materials and Methods

The 3D models generated for an unreinforced locking plate repaired three part fractured humerus in Chapter 4, were used for a macroscale device level application of the damage criteria, calibrated for cortical bone, in the current chapter. The model set up is shown in Figure 7.10. The osteon orientation applied to the model is also shown in Figure 7.10A. Osteon direction was applied parallel to the central axis of the medullary canal, in the shaft of the humerus (Rho et al. (1998)). A circumferential osteon orientation was applied to articular and greater tuberosity fragments of the proximal humerus (Heřt et al. (1994); Rho et al. (1998)). A pressure load was applied to represent 90 degree arm abduction at the glenohumeral joint. The applied pressure load was ramped up linearly. Simulations were conducted for a metallic (titanium (modulus of 110 GPa)) and CFPEEK locking plate (modulus of 18 GPa). Both materials were modelled as linear elastic, as was the case in Chapter 4.

7.4.2 Results

Damage was initiated for a metallic plate at a load of 411.42 N. A higher force of 573.9 N (a factor of 1.39 higher) was required to initiate damage in a CFPEEK repaired humerus. The predicted crack patterns are shown for each of the fracture fragments, for both metallic and CFPEEK devices (Figures 7.11-7.13). The glenohumeral loading was linearly increased to 1.28 kN to compare the level of crack growth in each of the fragments. The crack patterns predicted in the articular fragment of the humerus are shown in Figure 7.11. The exterior view of the articular fragment shows significantly higher crack growth parallel to the applied osteon direction compared to that predicted for a CF PEEK locking plate (Figure 7.11A and B)). Higher levels of crack growth were also observed for a titanium locking plate on the interior surface of the articular fragment. Additional cracks were predicted at the cortical bone central stabilising screw interface (Figure 7.11C). Damage was not initiated at this location for a CF PEEK locking plate (Figure 7.11D). The predicted crack patterns for the greater tuberosity fracture fragment are shown in Figure 7.12. The key difference between locking plate materials in this case was that crack prediction occurred on different surfaces of the greater tuberosity. Cracks were predicted on the interior surface of the greater tuberosity for a titanium locking plate, in contrast with crack prediction on the external surface of the greater tuberosity for a CFPEEK locking plate. No difference was observed in the crack pattern prediction for the humeral shaft fragment (Figure 7.13). Cracks were predicted perpendicular to the osteon direction in the same locations on the external surface of the humerus for both titanium and CF PEEK locking plates.

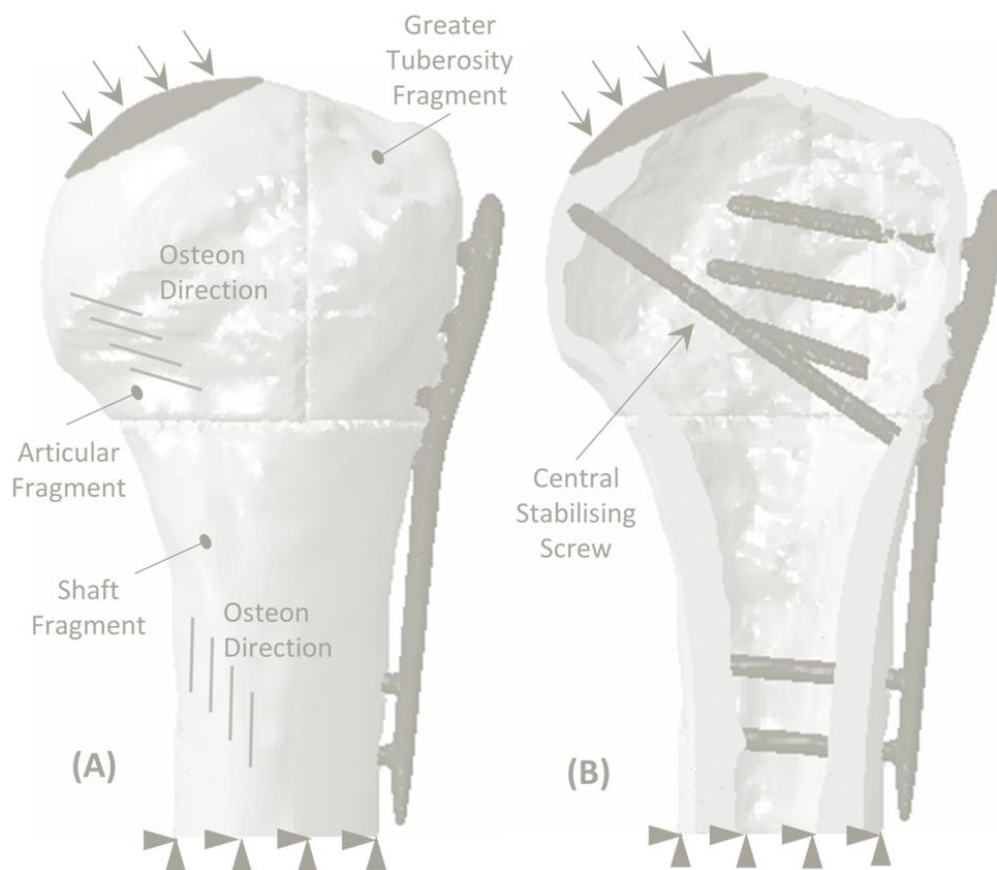


Figure 7.10 Loading and boundary conditions of 3D locking plate proximal humeral fracture fixation; (A) Pressure load applied to simulate 90 degree arm abduction. Osteon orientations applied to humerus highlighted on outer surface of bone; (B) Section view of humerus highlighting loading relative to locking plate position.

These initial simulations of three part proximal humeral fracture fixation under glenohumeral loading provided some insight into the critical locations at which screw pullout/pushout may occur. Comparison of titanium and CFPEEK materials highlight that the risk of screw pullout/pushout is even higher for stiffer materials, relative to the stiffness of cortical bone (in this case titanium). Although the geometry of the screws of the locking plate did not contain detailed thread shape geometry, it did highlight the potential for future application of the computational methodologies of this chapter in the development and design evaluation of the next generation of orthopaedic devices.

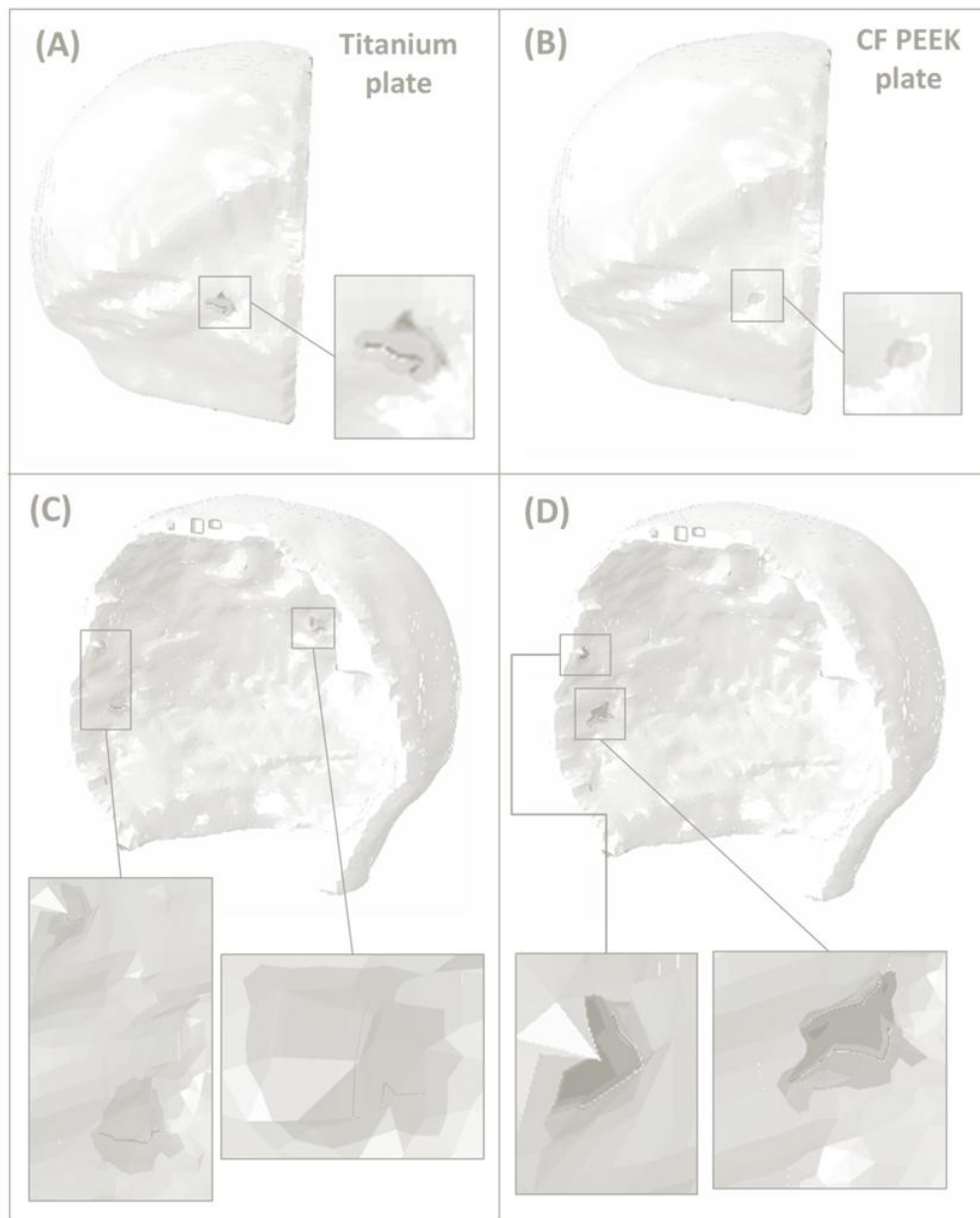


Figure 7.11 Crack initiation and propagation in the articular fragment for glenohumeral load of 1.28 kN; (A-B) Exterior view of articular fragment for titanium and CF PEEK locking plates respectively; (C-D) Interior view of articular fragment for titanium and CF PEEK locking plates respectively.

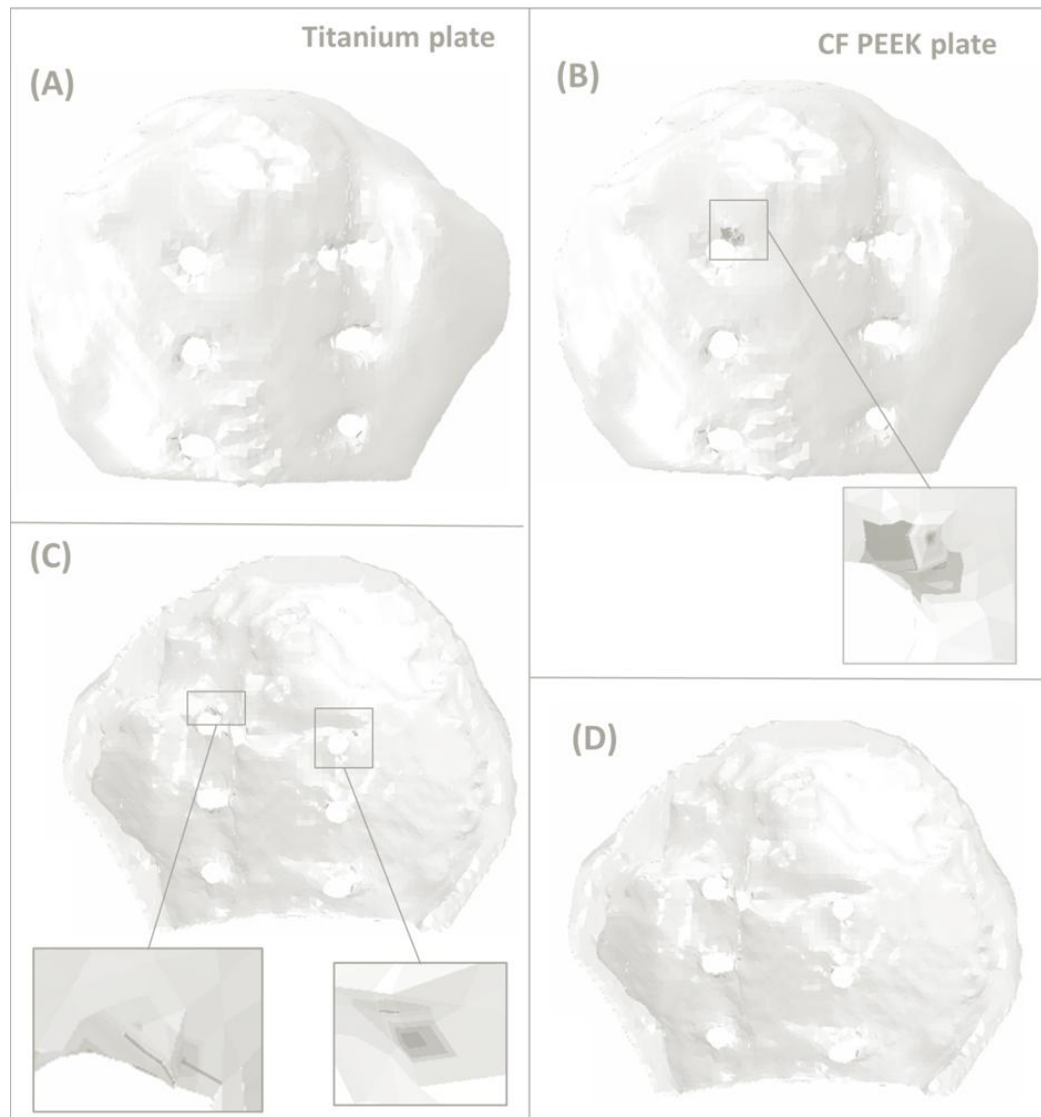


Figure 7.12 Crack initiation and propagation in the greater tuberosity fragment for glenohumeral load of 1.28 kN; (A-B) Exterior view of greater tuberosity fragment for titanium and CF PEEK locking plates respectively; (C-D) Interior view of greater tuberosity fragment for titanium and CF PEEK locking plates respectively.

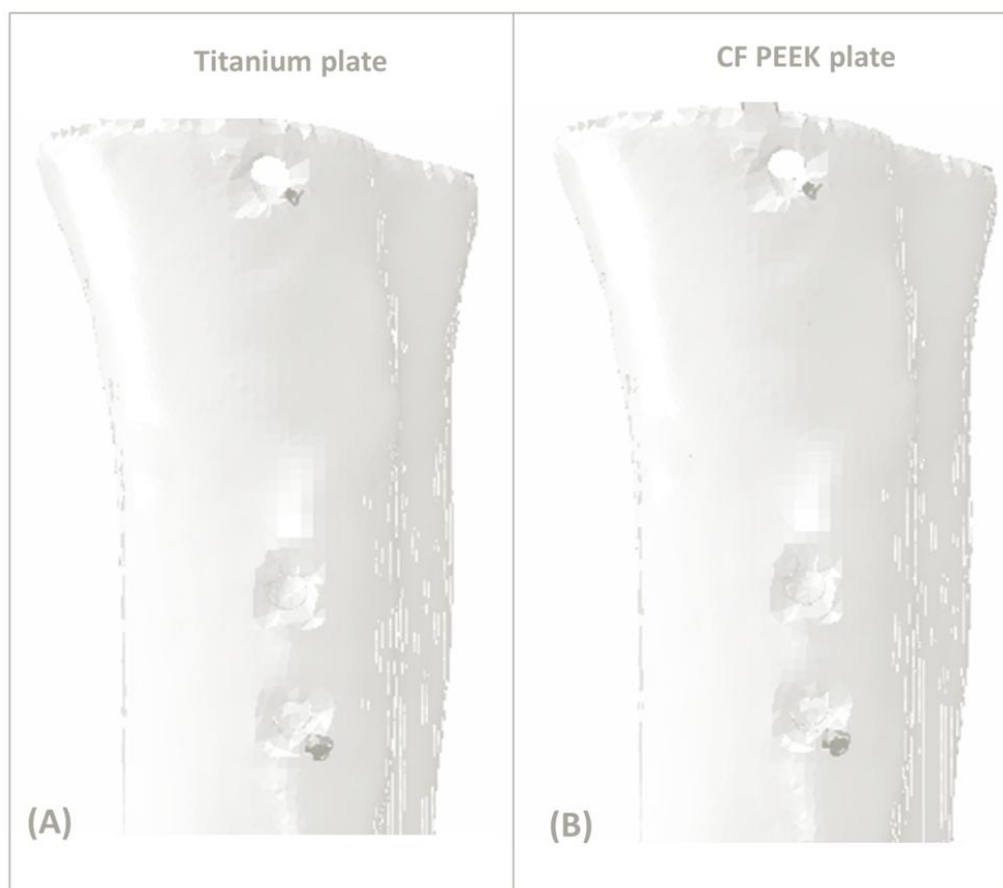


Figure 7.13 Crack initiation and propagation in the humeral shaft fragment for glenohumeral load of 1.28 kN; (A) Exterior view of humeral shaft fragment for titanium locking plate; (B) Exterior view of articular fragment for CF PEEK locking plate.

7.5 XFEM Application: CF PEEK orthopaedic screws

The results of the current chapter combined with Chapter 4 content, suggests the risk of screw pullout / pushout is reduced when CFPEEK devices are used. Therefore, simulations using the XFEM method were conducted to investigate the suitability of CFPEEK for direct replacement of metallic designs. CFPEEK can be injection moulded, therefore, the same geometries of metallic screws could be replicated. An investigation of the performance of CFPEEK was conducted using the 2D screw pullout models, presented in the current chapter. The material properties assigned to the CFPEEK were sourced from the literature for 30 % CF reinforced PEEK, the properties are summarised in Table 7.3 below (Kurtz and Devine (2007)).

Table 7.3 Material properties of carbon fibre reinforced PEEK

	Modulus of Elasticity (GPa)	Ultimate Strength (MPa)	Poisson's Ratio
30 % Carbon Fibre PEEK	20	170	0.4

The results for longitudinal pullout simulations are shown in Figure 7.14 for varying thread depths. For all screw depths, damage was initiated, not only in the cortical bone but also in the CF reinforced PEEK. This was due to the stress concentrations at the base of the screw threads as they merge into the central shaft. This design feature was not an issue for metals as the ultimate strengths were sufficiently higher than cortical bone. Therefore, when designing with CF reinforced PEEK care must be taken to avoid features that may give rise to such stress concentrations.

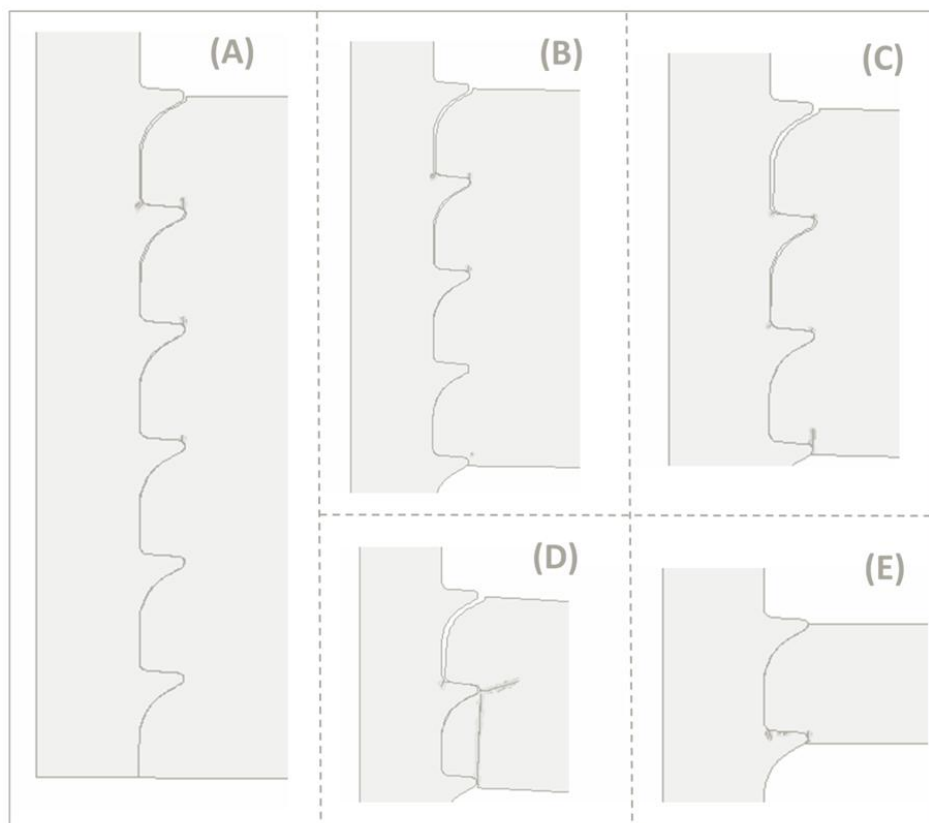


Figure 7.14 Longitudinal screw pullout simulations from cortical bone with CF reinforced PEEK screws for varying screw depths; (A) 5 threads of the screw were embedded in cortical bone; (B) 4 threads of the screw were embedded in cortical bone; (C) 3 threads of the screw were embedded in cortical bone; (D) 2 threads of the screw were embedded in cortical bone; (E) 1 thread of the screw was embedded in cortical bone.

7.6 Discussion

Cortical bone has a distinct aligned microstructure with microscale geometric features, determining the fracture patterns at the macroscale. Many previous computational studies investigating the damage and fracture of cortical bone have focussed on microscale simulations, incorporating details of the cortical bone microstructure (Budyn and Hoc (2010); Abdel-Wahab et al. (2012)). Upscaling of such a microstructural modelling approach to simulate macroscale fracture patterns (e.g. crack propagation during screw pullout) is not currently feasible due to excessive computational demand. In the present chapter an anisotropic damage initiation criteria is developed for the extended finite element method (XFEM) prediction of crack initiation and propagation in cortical bone. This anisotropic damage model is shown to accurately predict the dependence of crack propagation patterns and fracture toughness on mode mixity and on osteon orientations, as reported in previous experimental studies (Norman et al. (1996); Zimmermann et al. (2009)). This modelling approach is also used to simulate cortical bone failure mechanisms during screw pullout. Crack propagation patterns are found to correspond closely to the experimental observations of Chapter 5, for longitudinal and transverse osteon orientation.

The anisotropic behaviour of cortical bone has been well established (Reilly and Burstein (1975); Cowin (2001)). Previous studies have investigated the fracture toughness of cortical bone (Norman et al. (1996); Feng et al. (2000); Zimmermann et al. (2009); Zimmermann et al. (2010); An et al. (2011); Olvera et al. (2012)). These studies have reported a distinct relationship between the fracture toughness and microstructure alignment. Based on the findings of Zimmermann et al. (2009), Feng et al. (2000) and the present chapter content, mode II fracture toughness for longitudinally aligned cortical bone is higher than mode I. Feng et al. (2000) also reported that Mode II fracture toughness was higher than Mode I for transversely aligned cortical bone which conflicts with the opposing trend reported by Zimmermann et al. (2009) and by the present chapter. Zimmermann et al. (2009) attributed this to the fact that Feng et al. (2000) generated large notches in samples relative to sample thickness. Similar to the dependence in fracture toughness on osteon orientation in cortical bone, several natural/manmade composites exhibit a

dependence of mechanical and fracture properties on fibre alignment (Jernkvist (2001); Kondo et al. (2011)). The Hashin damage criteria has been developed to predict anisotropic damage in fibre reinforced laminates (Hashin (1980)). As these laminates are fibre reinforced, damage initiation predominately occurs in the matrix, with the crack trajectories being dependent on fibre direction. This is comparable to the trend observed for cortical bone, with crack patterns influenced by osteon orientation. Hence, the Hashin damage type criteria are an appropriate selection for the damage initiation criteria (Failure Index1&2) of the current chapter. The Hashin type failure criteria (1&2), used in the present chapter, capture the influence of osteon orientation on crack direction. Additionally, the current chapter implements alternate strengths in tension and compression, as motivated by previous experimental results for cortical bone (Bayraktar et al. (2004); Mercer et al. (2006)). The aforementioned Hashin type criteria, limit crack propagation to directions parallel or perpendicular to osteons. However, based on the experimental finding of Zimmermann et al. (2009), it is clear that the binary crack pattern that would be predicted by the Hashin type criteria would fail to predict the sensitivity of crack propagation to mode mixity, hence a third failure criterion must be implemented. The third failure criterion directs crack growth perpendicular to the direction of the maximum principal stress. This criterion is responsible for off axis crack growth prediction for the mixed mode case studies of four point bend and screw pullout. Thus, the combined failure criteria of the present chapter predicts; (i) the relationship between fracture energy and osteon alignment, (ii) the alternate crack patterns for both varying osteon orientations and loading angle, (iii) distinctive patterns of crack propagation during screw pullout.

Previous models of screw pullout from cortical and cancellous bone have been reported (Zhang et al. (2004); Wirth et al. (2010)). However, damage initiation and crack propagation were not incorporated into these models. A study by Chatzistergos et al. (2010) modelled screw pullout using predefined cohesive zone surfaces to simulate damage. XFEM offers an advance on this approach, as it eliminates the requirement to predefine the path of the crack. The experimental observations of Chapter 6 demonstrate significantly different failure mechanisms for longitudinal and transverse screw pullout, in addition to differences in pullout force, highlighting the importance of a modelling approach that is not limited to predefined crack paths.

In order to predict crack paths during screw pullout a 2D computational microstructure model with damage initiation and element removal was developed in Chapter 6. Both crack paths and predicted pull-out forces were found to correlate strongly with experimental observations. However, this modelling approach is dependent on the phenomenological representation of the microstructural features of cortical bone and on the resolution of the finite element mesh. Hence, the extension of this approach to 3D simulations is not computationally feasible. In contrast, the present chapter demonstrates that the XFEM modelling approach can reliably predict crack propagation patterns as a function of osteon orientation for both 2D and 3D screw pullout simulations. The ability to conduct 3D simulations of screw pullout allows for the investigation of several unsymmetrical features of screws such as the helix and the cutting flute of a self tapping screw.

Chapter 4 evaluated the performance of metallic and CFPEEK devices for fracture fixation, including locking plates, intramedullary rods and k-wires. The computational study of Chapter 4 relied on the identification of peak stress concentrations as indicators of potential failure. The methodologies developed in the current chapter, applied to an unreinforced locking plate fixation of a humerus, highlights the potential future application in designing the next generation of orthopaedic fracture fixation devices. The modelling technique could also be applied across a range of applications including suture anchors and a range of internal and external fracture fixation devices (GainesJr (2000), Kwon et al. (2002) Barber et al. (2008); Cuny et al. (2008)). In summary, the implementation of XFEM for device evaluation offers a powerful design tool. It can be used to evaluate, not only the design of the device but also the suitability of the site chosen to anchor the device.

In conclusion, the predicted transition in crack direction and fracture toughness as a function of osteon orientation and mode mixity, correspond closely with the results of previous experimental studies of cortical bone (Norman et al. (1996); Zimmermann et al. (2009)) and screw pullout (Chapter 5). The techniques developed in the current chapter are not limited to applications that consider cortical bone, but rather any composite material containing a known microstructural alignment. To the author's knowledge, this chapter is the first to implement anisotropic damage initiation criteria in conjunction with XFEM for cortical bone. The proposed

homogenised representation of cortical bone, coupled with anisotropic damage initiation criteria of the present chapter, predict: (i) the relationship between fracture energy and osteon alignment; (ii) the alternate crack patterns for both varying osteon orientations and loading angle; (iii) distinctive patterns of crack propagation during screw pullout.

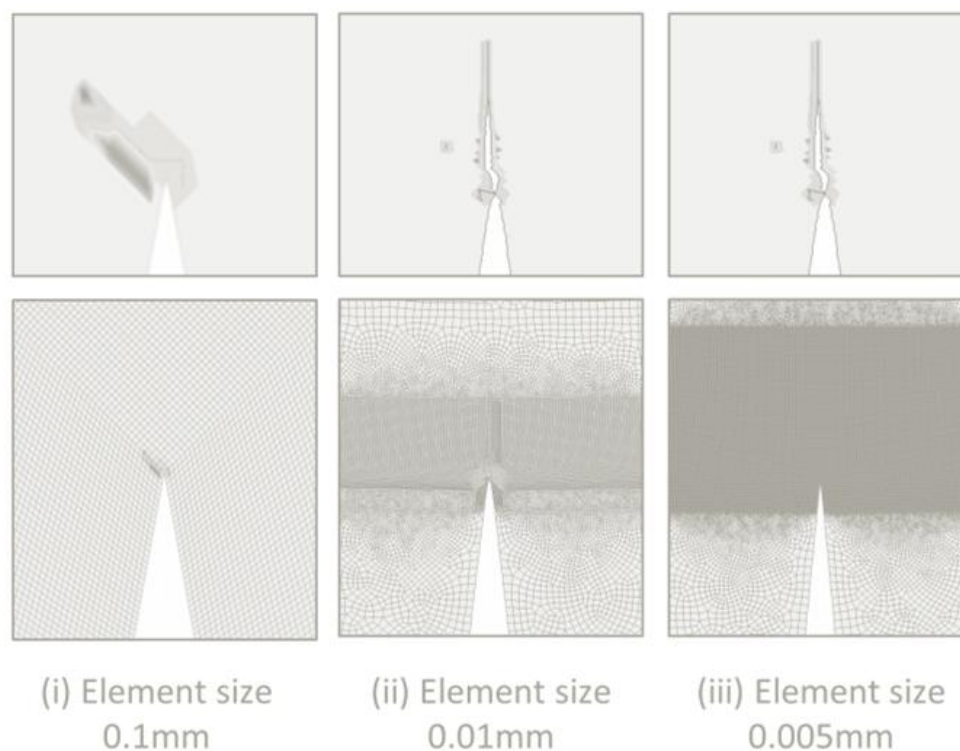
7.7 References

- Abaqus, 2012. Abaqus Users Manual 6.12, Dassault Systemes Simulia Corp., Providence.
- Abdel-Wahab, A. A., Maligno, A. R. and Silberschmidt, V. V., 2012. Micro-scale modelling of bovine cortical bone fracture: Analysis of crack propagation and microstructure using X-FEM. *Computational Materials Science* 52, 128-135.
- An, B., Liu, Y., Arola, D. and Zhang, D., 2011. Fracture toughening mechanism of cortical bone: An experimental and numerical approach. *Journal of the Mechanical Behavior of Biomedical Materials* 4, 983-992.
- Barber, F. A., Herbert, M. A., Beavis, R. C. and Barrera Oro, F., 2008. Suture Anchor Materials, Eyelets, and Designs: Update 2008. *Arthroscopy: The Journal of Arthroscopic & Related Surgery* 24, 859-867.
- Bayraktar, H. H., Morgan, E. F., Niebur, G. L., Morris, G. E., Wong, E. K. and Keaveny, T. M., 2004. Comparison of the elastic and yield properties of human femoral trabecular and cortical bone tissue. *Journal of Biomechanics* 37, 27-35.
- Budyn, É. and Hoc, T., 2010. Analysis of micro fracture in human Haversian cortical bone under transverse tension using extended physical imaging. *International Journal for Numerical Methods in Engineering* 82, 940-965.
- Chatzistergos, P. E., Magnissalis, E. A. and Kourkoulis, S. K., 2010. A parametric study of cylindrical pedicle screw design implications on the pullout performance using an experimentally validated finite-element model. *Medical Engineering & Physics* 32, 145-154.
- Cowin, S. C., 2001. Bone mechanics handbook, CRC press USA.
- Cuny, C., Scarlat, M. M., Irrazi, M., Beau, P., Wenger, V., Ionescu, N. and Berrichi, A., 2008. The Telegraph nail for proximal humeral fractures: A prospective four-year study. *J Shoulder Elbow Surg* 17, 539-545.
- Feng, Z., Rho, J., Han, S. and Ziv, I., 2000. Orientation and loading condition dependence of fracture toughness in cortical bone. *Materials Science and Engineering: C* 11, 41-46.
- Gaines Jr, R. W., 2000. The Use of Pedicle-Screw Internal Fixation for the Operative Treatment of Spinal Disorders. *The Journal of Bone and Joint Surgery (American)* 82, 1458-1458.
- Hashin, Z., 1980. Failure Criteria for Unidirectional Fiber Composites. *Journal of applied mechanics* 47, 329-334.
- He, M., 2000. Asymmetric four-point crack specimen. *Journal of applied mechanics* 67, 207.
- Heřt, J., Fiala, P. and Petrtyl, M., 1994. Osteon orientation of the diaphysis of the long bones in man. *Bone* 15, 269-277.
- Jernkvist, L. O., 2001. Fracture of wood under mixed mode loading: II. Experimental investigation of *Picea abies*. *Engineering Fracture Mechanics* 68, 565-576.
- Kondo, A., Sato, Y., Suemasu, H. and Aoki, Y., 2011. Fracture Resistance of Carbon/Epoxy Composite Laminates under Mixed-Mode II and III Failure and Its Dependence on Fracture Morphology. *Advanced Composite Materials* 20, 405-418.
- Kurtz, S. M. and Devine, J. N., 2007. PEEK biomaterials in trauma, orthopedic, and spinal implants. *Biomaterials* 28, 4845-4869.

- Kwon, B. K., Goertzen, D. J., O'Brien, P. J., Broekhuysse, H. M. and Oxland, T. R., 2002. Biomechanical evaluation of proximal humeral fracture fixation supplemented with calcium phosphate cement. *J Bone Joint Surg Am* 84, 951-61.
- Lapczyk, I. and Hurtado, J. A., 2007. Progressive damage modeling in fiber-reinforced materials. *Composites Part A: Applied Science and Manufacturing* 38, 2333-2341.
- Marsavina, L. and Piski, T., 2010. Bimaterial Four Point Bend Specimen with Sub-Interface Crack. *International Journal of Fracture* 164, 325-332.
- Matzenmiller, A., Lubliner, J. and Taylor, R. L., 1995. A constitutive model for anisotropic damage in fiber-composites. *Mechanics of Materials* 20, 125-152.
- Melenk, J. M. and Babuška, I., 1996. The partition of unity finite element method: Basic theory and applications. *Computer Methods in Applied Mechanics and Engineering* 139, 289-314.
- Mercer, C., He, M. Y., Wang, R. and Evans, A. G., 2006. Mechanisms governing the inelastic deformation of cortical bone and application to trabecular bone. *Acta Biomaterialia* 2, 59-68.
- Norman, T. L., Nivargikar, S. V. and Burr, D. B., 1996. Resistance to crack growth in human cortical bone is greater in shear than in tension. *Journal of Biomechanics* 29, 1023-1031.
- Olvera, D., Zimmermann, E. A. and Ritchie, R. O., 2012. Mixed-mode toughness of human cortical bone containing a longitudinal crack in far-field compression. *Bone* 50, 331-336.
- Reilly, D. T. and Burstein, A. H., 1975. The elastic and ultimate properties of compact bone tissue. *Journal of Biomechanics* 8, 393-396, IN9-IN11, 397-405.
- Rho, J.-Y., Kuhn-Spearing, L. and Zioupos, P., 1998. Mechanical properties and the hierarchical structure of bone. *Medical Engineering & Physics* 20, 92-102.
- Sukumar, N., Huang, Z. Y., Prévost, J. H. and Suo, Z., 2004. Partition of unity enrichment for bimaterial interface cracks. *International Journal for Numerical Methods in Engineering* 59, 1075-1102.
- Wirth, A., Mueller, T., Vereecken, W., Flaig, C., Arbenz, P., Müller, R. and van Lenthe, G., 2010. Mechanical competence of bone-implant systems can accurately be determined by image-based micro-finite element analyses. *Archive of Applied Mechanics* 80, 513-525.
- Zhang, Q. H., Tan, S. H. and Chou, S. M., 2004. Investigation of fixation screw pull-out strength on human spine. *Journal of Biomechanics* 37, 479-485.
- Zimmermann, E. A., Launey, M. E., Barth, H. D. and Ritchie, R. O., 2009. Mixed-mode fracture of human cortical bone. *Biomaterials* 30, 5877-5884.
- Zimmermann, E. A., Launey, M. E. and Ritchie, R. O., 2010. The significance of crack-resistance curves to the mixed-mode fracture toughness of human cortical bone. *Biomaterials* 31, 5297-5305.

7.8 Appendix 7A: Mesh Sensitivity

A mesh sensitivity study was conducted to investigate the mesh independence of crack propagation using the XFEM method. It is clear from the images of Figure 7A.1 that the optimum element length must be identified. A low density mesh with large element lengths may slow the rate of crack turning and the prediction of steady state crack trajectory (Figure 7A.1(i)). A structured mesh should be implemented in the regions in which crack initiation occurs. Generating a structured quad mesh surrounding the crack tip (Figure 7A.1(ii)) leads to a correct prediction of crack orientation. A further increase in mesh density has no effect on the predicted failure mode or failure load (Figure 7A.1(iii)).



Feerick et al. (2013) JMBBM, Article In Press, <http://dx.doi.org/10.1016/j.jmbbm.2012.12.004>

Figure 7A.1 Mesh sensitivity study for (i) unstructured mesh; (ii) optimum structure mesh (iii) higher density structured mesh

7.9 Appendix 7B: XFEM Observations

Some key observations associated with the use of XFEM are summarised in Figure 7B.1. Surfaces at which cracks are expected to reach completion by exiting the mesh should not contain single nodes of any element (Figure 7B.1A(i)). If the crack reaches the point of a single node and the element cannot be split then the

crack will alter its' trajectory, as highlighted in Figure 7B.1A(ii-iii). This results in unrealistic force predictions as additional work is required to grow the crack horizontally. Another example of cracks reaching the end of an enrichment zone but failing to exit the mesh is highlighted in Figure 7B.1B(i). As a result of the crack reaching the end of the enrichment zone and failing to exit the mesh, the crack tip at the neighbouring thread alters trajectory. The crack is forced horizontally until it is free to return to vertical crack growth again (Figure 7B.1B(ii)), resulting in additional work reported in the force predictions. Additionally, it was noted that the use of multiple enrichment zones can lead to issues with cracks bridging between neighbouring enrichment zones (Figure 7B.1C(i)). This can result in elevated force predictions as the resulting fracture surfaces resist further crack growth (Figure 7B.1C(ii)). All of the highlighted issues of Figure 7B.1 were overcome with the implementation of a structured mesh.



Feerick et al. (2013) JMBBM, Article In Press, <http://dx.doi.org/10.1016/j.jmbbm.2012.12.004>

Figure 7B.1 XFEM crack patterns influenced by the mesh and enrichment regions; (A) Single node located on surface of mesh, (B) Altered crack trajectory due to crack failing to exit mesh, (C) Bridging of cracks between neighbouring enrichment regions resulting in elevated failure force predictions

7.10 Appendix 7C: 2D FORTRAN User Subroutine

Content Removed Due to Copyright

Content Removed Due to Copyright

7.11 Appendix 7D: 3D FORTRAN User Subroutine

Content Removed Due to Copyright

Content Removed Due to Copyright

Content Removed Due to Copyright

Chapter 8

Concluding Remarks

The field of orthopaedic fracture fixation covers a vast range of fracture types with a broad range of fixation devices to select from. Optimal devices or fracture fixation techniques have not been identified for particular fractures. Selection of device/fixation technique is made at the discretion of the associated orthopaedic surgeon. For example, deciding between a locking plate and an intramedullary rod for a proximal humeral fracture fixation. Additionally, there may be a range of surgical choices for a given device regarding how many screws to use to anchor the device and the spacing of these screws. (Wilkens et al. (2008); Königshausen et al. (2012)). Surgeons are not provided with device designer guidelines offering biomechanical motivation for selecting a device or anchor location. Rather, surgical selections are generally based upon clinical reports that offer scales of patient satisfaction/functionality, or the devices that were used during surgical training of the orthopaedic surgeon. There is a significant need for greater biomechanical input into surgical decisions, with more direct communication between surgeons and device designers. The primary fracture application considered in this thesis is complex three part fractures of the proximal humerus, with a particular focus on orthopaedic screw pullout. In order to develop future next generation devices capable of surpassing their predecessors, in terms of lifespan and reversion to intact functionality, it is necessary to ascertain the design flaws and failure mechanisms of existing devices. Most importantly, an in-depth understanding of the complex fracture mechanics and failure mechanisms of the cortical bone is integral to the successful design and analysis of orthopaedic devices. Such an enhanced understanding of bone biomechanics is critical not just for device design, but also from a clinical perspective in terms of device selection. Therefore, the work of this thesis aimed to explore the mechanisms of cortical bone fracture through the symbiotic development of experimental studies and computational finite element modelling studies. Experimental studies provided novel visual insight with regard to the relationship between crack patterns, screw pullout force and microstructural alignment of cortical bone. Development of computational models that are capable of capturing these relationships offers significant potential in the development of

future next generation devices. One such example is the evaluation of emerging biomaterials such as CFPEEK as a suitable alternative to currently used metallic materials.

The study of Chapter 4, for the first time, computationally compared four fracture fixation techniques for proximal humerus fractures, with a specific focus on cortical bone stress, fracture fragment displacement, cement reinforcement and device material properties at 90° arm abduction. Previous studies of proximal humeral fracture repair were predominately clinical or experimental, with very few studies using finite element analysis to evaluate proximal humeral fracture fixation. For example, the study reported by Maldonado et al. (2003) conducted finite element simulations on a plate fixation of a two part humeral fracture by representing fracture lines as areas of low stiffness, providing limited insight into relative fracture fragment motion. However, in Chapter 4, finite sliding hard contact was implemented between fracture fragments that facilitated modelling of fracture line opening in addition to relative sliding between fracture fragments. This provided a more accurate representation of the interaction between fracture fragments following repair. Simulations predicted that reinforced fixation led to a reduction in relative sliding between fracture fragments in addition to a reduction in fracture line opening under cyclic loading at the glenohumeral interface. This finding was supported by previous clinical and experimental observations. (Kwon et al. (2002); Mathison et al. (2010); Rose et al. (2010); Neviasser et al. (2011)). Elevated stress concentrations, noted at the screw cortical bone interface, also provided insight with regard to the commonly reported screw pullout/pushout (Owsley and Gorczyca (2008)). The identification of these stresses supported the fact that overly stiff metallic devices, compared to the stiffness of cortical bone (Lill et al. (2003)), leads to block pullout of screws or screw penetration into the glenoid (Owsley and Gorczyca (2008); Clavert et al. (2010); Dheerendra et al. (2011)). The magnitude of these stresses were computed in the range of the ultimate strength of osteoporotic cortical bone (Dickenson et al. (1981)).

The use of lower stiffness materials, closer to the modulus of cortical bone, such as carbon fibre reinforced PEEK (CFPEEK), are proposed in Chapter 4 as an alternative to metallic devices for proximal humeral fracture repair. Composite

materials have previously been proposed for orthopaedic fracture fixation (Yáñez et al. (2010); Bougherara et al. (2011)). Simulations of a CFPEEK locking plate and IM rod highlight the significant reduction in stresses at the screw cortical bone interface that may lower the incidence of screw pullout/pushout. In addition to reducing stress concentrations at the screw cortical bone interface, simulations demonstrate that the relative displacement of fracture fragments is comparable to that of metallic equivalent devices. Therefore the use of the more compliant CFPEEK material to reduce stress concentrations within the humerus was predicted not to compromise device stability in terms of fracture line displacement. Composite materials have promising prospects in the field of orthopaedic fracture fixation due to the fact that FDA approval has been established for these materials in recent years and several grades are available. In Table 8.1 the material properties of three grades of polyetheretherketone (PEEK) are summarised. Table 8.1 highlights the wide range of material properties available and thus the potential to replace metallic devices that are currently overly stiff, significantly altering the stress distribution within whole bones compared to the intact case.

Table 8.1 Unreinforced and reinforced PEEK mechanical properties (Kurtz and Devine (2007))

	Unreinforced PEEK	30% Short CF reinforced PEEK	68% Continuous CF reinforced PEEK
Flexural Modulus (GPa)	4	20	135
Tensile Strength (MPa)	93	170	>2000
Tensile Elongation (%)	30 - 40	1 - 2	1
Poisson's ratio	0.36	0.4	0.38

Due to the computationally observed trend of stress concentrations occurring at the screw cortical bone interface and the clinically reported failures of screw anchored devices, it was clear that the cortical bone failure mechanisms during screw pullout merited further study. The development of a novel experimental test rig (screw pullout damage visualisation (SPDV) test of Chapter 5), facilitating visualisation of failure modes in real time during pullout, offered unprecedented insight into the

relationship between osteon orientation, screw pullout strength and crack patterns. Transverse pullout (osteons perpendicular to screw axis) was observed to require a pullout force a factor of two higher than a longitudinal pullout (osteons parallel to screw axis). Transverse pullout also required significantly higher levels of deformation and crack growth perpendicular to the axis of screw, in order to be removed from the bone. The load data recorded during an SPDV tests was validated by the load displacement data from standard pullout tests. The SPDV test rig is not limited to investigating the failure mechanisms of cortical bone during screw pullout. The rig could be used to investigate a multitude of anchors in a variety of biomaterials such as cancellous bone, bone cement or combined layers of these materials. The experimental testing of Chapter 5 focused on monotonic screw pullout; however the loading application could be altered to investigate the fatigue performance of anchors and materials to investigate loosening. The loading configuration could also be modified from simply tensile to compressive for screw pushout or off axis loading to represent toggling of screws. The SPDV test rig is also a relatively low cost rig compared to other studies that utilised micro CT scanners to image failure mechanisms (Wirth et al. (2010)). Such a micro CT based approach also prohibits the testing of metallic screws/components due to resultant imaging artefacts.

The relationship uncovered between osteon orientation, crack patterns and pullout force during cortical bone screw pullout (by the SPDV test of Chapter 5) provided strong motivation, to develop a predictive computational model with the capability of capturing this relationship. The computational models generally under predict the screw pullout strength compared to experimental test which provides an inbuilt factor of safety. The development of a computational model, capable of predicting both pullout force and crack propagation patterns as a function of osteon-screw alignment, would provide a powerful design tool for development and evaluation of new materials and screw geometries (Goldhahn et al. (2006); Yáñez et al. (2010)). Previous computational studies of screw pullout have modelled bone as an elasto-plastic continuum without any modelling of fracture or damage (Zhang et al. (2004); Wirth et al. (2010)). Chatzistergos et al. (2010) modelled pullout from solid rigid polyurethane foam using a homogeneous material model with cohesive zone surfaces applied along predefined paths. This type of modelling approach would not be

capable of predicting the crack patterns observed during a transverse pullout, which involved significant crack growth perpendicular to the central screw axis. Therefore it was clear that a method of fracture modelling would have to be selected that did not require predefined crack growth. The first computational method implemented for modelling screw pullout was a homogeneous elasto-plastic continuum with damage initiation according to an equivalent plastic strain invariant and the element deletion method was used to model subsequent crack propagation as outlined in Chapter 6. This modelling approach predicted the same crack patterns for longitudinal and transverse pullout simulations. Hence, in order to improve on this model, a phenomenological representation of the microstructure of cortical bone was required, in order to replicate the different experimentally observed failure loads and crack patterns for longitudinal and transverse screw pullout. This model consisted of multiple layers of two distinctly different materials with different stiffness, yield strengths and damage initiation and evolution criteria. This biphasic multi-layered composite model developed for cortical bone, accurately predicted the significantly higher pullout forces during transverse screw pullout. Additionally, this model predicted the significantly different crack growth directions for longitudinal and transverse crack growth. The biphasic multi-layered composite model provides a useful design paradigm for application specific fracture fixation devices, offering a better understanding of potential failure mechanisms. As previously mentioned, commercially available locking plates contain a range of locations for device anchoring (Smith et al. (2007)). Distribution of screws too closely together, particularly for transverse cortical bone orientation, may lead to uniting of cracks and extensive regions of bone damage, adding significant complications to revision surgery. Using the methodologies developed, more precise guidelines regarding screw orientation, screw thread design selection, and spacing of screws can be provided to surgeons.

Computational crack propagation was predicted using the element deletion technique, by the removal of several adjoining elements. The distinct geometric representation of the microstructure of the biphasic multi-layered composite guided the paths of element deletion. Application of the biphasic multi-layered composite model to 3D simulations was not possible due to excessive computational demand. Therefore an alternate computational approach that eliminated the need for explicit

geometric representation of the microstructure was developed in Chapter 7. Anisotropic damage initiation criteria, with associated crack propagation directions, were implemented using the extended finite element method (XFEM) to simulate direction dependent crack propagation. It is demonstrated in Chapter 7 that it is sufficient to model cortical bone as a homogeneous, anisotropic elastic continuum with a known osteon orientation, without the need for a phenomenological representation of cortical bone microstructure. XFEM involves splitting of elements to simulate crack propagation rather than removing elements from the mesh as implemented in the microstructural model of Chapter 6. Although the element deletion method of Chapter 6 was limited to 2D applications, it demonstrated the importance of the composite nature of cortical bone in crack propagation patterns. Hence, this motivated the use of composite based damage criteria for the XFEM damage initiation criteria. Hashin damage type criteria were developed for two of the damage initiation criteria of Chapter 7. These Hashin based criteria provided good replication of crack patterns reported in previous experimental studies of Mode I and II cortical bone fracture (Norman et al. (1996); Zimmermann et al. (2009)). However off axis crack prediction, that was observed during experimental mixed mode loading of cortical bone (Zimmermann et al. (2009)), required the development of a third criterion. This criterion was based upon an effective stress with crack growth defined orthogonal to the maximum principal stress direction. Additionally, asymmetric strengths in tension and compression were assigned, as motivated by previous experimental results for cortical bone (Bayraktar et al. (2004); Mercer et al. (2006)). The combined failure criteria developed for XFEM predicted; (i) the relationship between fracture energy and osteon alignment and (ii) the alternate crack patterns for both varying osteon orientations and loading angle as reported for experimental studies of single and mixed mode fracture of cortical bone (Norman et al. (1996); Zimmermann et al. (2009)). Further application of the calibrated models to 2D and 3D screw pullout illustrated the ability of the developed computational model to predict; (i) distinctive patterns of crack propagation during screw pullout and (ii) osteon alignment dependent screw pullout strength.

The anisotropic damage initiation criteria, developed for XFEM prediction of crack initiation and propagation in cortical bone, offers a powerful design tool. It can be used to evaluate not only the design of the device but also the suitability of the site

chosen to anchor the device. This is further confirmed by the additional applications outlined in Chapter 7 for 3D simulations of screw pullout, three part proximal humeral fracture repair and 2D simulations of CFPEEK screws. As concluded from the findings of Chapter 4, CFPEEK devices lower stress concentrations at the screw cortical bone interface, lowering the risk of screw pullout/pushout. In Chapter 7, the calibrated material and anisotropic damage model for cortical bone with XFEM prediction of crack propagation, was applied to a 3D model of locking plate fixation of a three part fractured humerus. Simulations compared a CFPEEK locking plate with a titanium equivalent. Predicted crack initiation load was 28% lower in the case of a titanium plate compared to a CFPEEK plate. The critical locations of crack initiation and directions of crack propagation were identified. This highlights the potential for future application of the methodologies developed in this thesis to evaluate existing devices, and to guide the development of improved/novel designs. Simulation of pullout of CFPEEK screws from cortical bone predicted cracks in both cortical bone and CFPEEK screws. Therefore, this suggests that existing designs intended for metallic screws will require some geometric modifications to reduce stress concentrations if CFPEEK material is used.

The findings of this thesis provide the motivation for further investigation of CFPEEK for the field of orthopaedic fracture fixation. Furthermore, the experimental and computational techniques developed in this thesis provide the toolset to do so. Ongoing work by the author using the techniques developed in this thesis, in conjunction with a biomaterials company, has been in an area of insertion of self tapping CFPEEK suture anchors. Modelling of the insertion of screws was beyond the scope of this thesis; however it is considered an important aspect of screw design, due to potential damage initiation or plastic deformation during insertion. Future work should also involve the development of computational models to capture the fracture mechanics of cancellous bone and bone cement. Therefore, the failure mechanisms of these materials could also be incorporated into 3D fracture fixation techniques of 3 part humerus fracture simulations. This would provide a complete understanding of the failure mechanisms in each of the materials involved in the repair. Beyond the applications provided in the present thesis, the experimental and computational techniques developed can also be applied to multiple aspects of orthopaedic fracture fixation device design at multiple scales of interest, ranging

from specific individual components of the device to evaluation of the overall performance of the device under physiological loading conditions.

References

- Bayraktar, H. H., Morgan, E. F., Niebur, G. L., Morris, G. E., Wong, E. K. and Keaveny, T. M., 2004. Comparison of the elastic and yield properties of human femoral trabecular and cortical bone tissue. *Journal of Biomechanics* 37, 27-35.
- Bougherara, H., Zdero, R., Dubov, A., Shah, S., Khurshid, S. and Schemitsch, E. H., 2011. A preliminary biomechanical study of a novel carbon–fibre hip implant versus standard metallic hip implants. *Medical Engineering & Physics* 33, 121-128.
- Clavert, P., Adam, P., Bevort, A., Bonnomet, F. and Kempf, J. F., 2010. Pitfalls and complications with locking plate for proximal humerus fracture. *J Shoulder Elbow Surg* 19, 489-494.
- Dheerendra, S. K., Khan, W. S., Barber, J., Goddard, N. J. and Ahrens, P. M., 2011. Outcomes of locking plates in proximal humeral fractures: a systematic review. *Shoulder & Elbow* 3, 74-84.
- Dickenson, R. P., Hutton, W. C. and Stott, J. R., 1981. The mechanical properties of bone in osteoporosis. *Journal of Bone and Joint Surgery-British Volume* 63, 233-38.
- Goldhahn, J., Reinhold, M., Stauber, M., Knop, C., Frei, R., Schneider, E. and Linke, B., 2006. Improved anchorage in osteoporotic vertebrae with new implant designs. *Journal of Orthopaedic Research* 24, 917-925.
- Königshausen, M., Kübler, L., Godry, H., Citak, M., Schildhauer, T. A. and Seybold, D., 2012. Clinical outcome and complications using a polyaxial locking plate in the treatment of displaced proximal humerus fractures. A reliable system? *Injury* 43, 223-231.
- Kurtz, S. M. and Devine, J. N., 2007. PEEK biomaterials in trauma, orthopedic, and spinal implants. *Biomaterials* 28, 4845-4869.
- Kwon, B. K., Goertzen, D. J., O'Brien, P. J., Broekhuysse, H. M. and Oxland, T. R., 2002. Biomechanical evaluation of proximal humeral fracture fixation supplemented with calcium phosphate cement. *J Bone Joint Surg Am* 84, 951-61.
- Lill, H., Hepp, P., Korner, J., Kassi, J. P., Verheyden, A. P., Josten, C. and Duda, G. N., 2003. Proximal humeral fractures: how stiff should an implant be? *Arch Orthop Trauma Surg* 123, 74-81.
- Maldonado, Z. M., Seebeck, J., Heller, M. O. W., Brandt, D., Hepp, P., Lill, H. and Duda, G. N., 2003. Straining of the intact and fractured proximal humerus under physiological-like loading. *J Biomech* 36, 1865-1873.
- Mathison, C., Chaudhary, R., Beaupre, L., Reynolds, M., Adeeb, S. and Bouliane, M., 2010. Biomechanical analysis of proximal humeral fixation using locking plate fixation with an intramedullary fibular allograft. *Clin Biomech* 25, 642-646.
- Mercer, C., He, M. Y., Wang, R. and Evans, A. G., 2006. Mechanisms governing the inelastic deformation of cortical bone and application to trabecular bone. *Acta Biomaterialia* 2, 59-68.
- Neviasser, A. S., Hettrich, C. M., Beamer, B. S., Dines, J. S. and Lorich, D. G., 2011. Endosteal Strut Augment Reduces Complications Associated With Proximal Humeral Locking Plates. *Clin. Orthop. Relat. Res.* 3300-3306.

- Norman, T. L., Nivargikar, S. V. and Burr, D. B., 1996. Resistance to crack growth in human cortical bone is greater in shear than in tension. *Journal of Biomechanics* 29, 1023-1031.
- Owsley, K. C. and Gorczyca, J. T., 2008. Displacement/Screw Cutout After Open Reduction and Locked Plate Fixation of Humeral Fractures. *J Bone Joint Surg Am* 90, 233-240.
- Rose, D. M., Sutter, E. G., Mears, S. C., Gupta, R. R. and Belkoff, S. M., 2010. Proximal Humeral Fractures. *Geriatric Orthopaedic Surgery & Rehabilitation* 1, 73-7.
- Smith, W. R., Ziran, B. H., Anglen, J. O. and Stahel, P. F., 2007. Locking plates: tips and tricks. *The Journal of Bone and Joint Surgery (American)* 89, 2298-2307.
- Wilkins, K. J., Curtiss, S. and Lee, M. A., 2008. Polyaxial locking plate fixation in distal femur fractures: a biomechanical comparison. *Journal of Orthopaedic Trauma* 22, 624.
- Wirth, A., Mueller, T., Vereecken, W., Flaig, C., Arbenz, P., Müller, R. and van Lenthe, G., 2010. Mechanical competence of bone-implant systems can accurately be determined by image-based micro-finite element analyses. *Archive of Applied Mechanics* 80, 513-525.
- Yáñez, A., Carta, J. A. and Garcés, G., 2010. Biomechanical evaluation of a new system to improve screw fixation in osteoporotic bones. *Medical Engineering & Physics* 32, 532-541.
- Zhang, Q. H., Tan, S. H. and Chou, S. M., 2004. Investigation of fixation screw pull-out strength on human spine. *Journal of Biomechanics* 37, 479-485.
- Zimmermann, E. A., Launey, M. E., Barth, H. D. and Ritchie, R. O., 2009. Mixed-mode fracture of human cortical bone. *Biomaterials* 30, 5877-5884.